MAGNETIC MEDIA PATTERNED BY LASER INTERFERENCE LITHOGRAPHY

Voorzitter, secretaris:	Prof. dr. ir. A.J. Mouthaan	Universiteit Twente, EWI
Promotor:	Prof. dr. J.C. Lodder	Universiteit Twente, EWI
Assistent promotor:	Dr. ir. L. Abelmann	Universiteit Twente, EWI
Referent	Dr. J. Martens	ASML, Eindhoven
Leden:	Prof. dr. M.C. Elwenspoek	Universiteit Twente, EWI
	Prof. dr. ir. J. Huskens	Universiteit Twente, EWI
	Prof. dr. A. Driessen	Universiteit Twente, EWI
	Prof. dr B.K. Middleton	University of Manchester, UK

The research described in this thesis was funded by the Dutch Technology Foundation (STW)
The research was carried out at the Systems and Materials for Information storage group (SMI) of the MESA^{+} research institute at the University of Twente.

Cover design:
The cover shows a series of MFM images of CoNi/Pt nanodots after application of different external magnetic fields.
The MFM images were taken by Martin Siekman

© R. Murillo, Enschede, 2006
No part of this work may be reproduced by print, photocopy or any other means without the permission in writing from the publisher.

ISBN 90-365-2344-3

MAGNETIC MEDIA PATTERNED BY LASER INTERFERENCE LITHOGRAPHY

PROEFSCHRIFT

ter verkrijging van
de graad van doctor aan de Universiteit Twente,
op gezag van de rector magnificus,
prof. dr. W. H. M. Zijm,
volgens het besluit van het College voor Promoties
in het openbaar te verdedigen
op woensdag 12 april 2006 om 15.00 uur

door

Rogelio Murillo Vallejo

geboren op 25 April 1972

te Mexico-stad

Dit proefschrift is goedgekeurd door

de promotor:	Prof. dr. J.C. Lodder
de assistent promotor:	Dr. ir. L. Abelmann

Contents

1 Introduction 9
1.1 Development of magnetic recording 9
1.1.1 Early history of magnetic recording 9
1.1.2 Magnetic recording for the computer industry 10
1.1.3 Hard disks for personal computers 10
1.2 Possible pathways for further increase the areal bit density 11
1.2.1 The problem of thermostability 11
1.2.2 Perpendicular recording 12
1.2.3 Patterned media 12
1.3 Methods for preparing patterned media for magnetic recording 13
1.3.1 Ion beam nano-structuring 13
1.3.2 Nano-imprint 14
1.3.3 Pre-patterned substrates 15
1.3.4 Self-assembling structures 15
1.3.5 Interference lithography 16
1.4 Outline of this thesis 16

2 Characteristics for a magnetic patterned medium for information storage 19
2.1 General description 19
2.2 Thermostability of arrays of dots 20
2.2.1 Probability of switching 21
2.2.2 Rate of switching 21
2.2.3 Relaxation time 22
2.3 Raw bit-error rate 22
2.4 Energy barrier 24
2.5 Dot to dot interactions: demagnetizing field 25
2.6 Anisotropy and magnetization saturation 28
2.7 Energy barrier distribution 31
2.8 Probe to dot interactions 32
2.8.1 Switching field distribution 32

2.8.2 Probe dimensions: necessity of a complementary technique in probe recording . . . 34
2.8.3 Probe dimensions: influence of probe size on neighbouring dots . . . 35
2.9 Auxiliary field . . . 38
2.10 Conclusion . . . 39

3 Laser interference lithography for film patterning 41
3.1 LIL for magnetic patterned media . . . 41
3.2 Principle of interference . . . 42
3.3 Types of laser interferometers . . . 43
3.3.1 The dual beam interferometer . . . 43
3.3.2 The Lloyd's Mirror Interferometer . . . 44
3.3.3 Advantages of the Lloyd's Mirror array . . . 45
3.3.4 Interference Lithography arrays by means of diffractive optic elements . . . 46
3.4 Particular details on the used laser interference setup . . . 49
3.5 Summary . . . 51

4 Preparation and characterization of CoNi/Pt and Co/Pt multilayers 53
4.1 Introduction . . . 53
4.2 Magnetic characterization techniques . . . 54
4.2.1 Vibrating sample magnetometry . . . 54
4.2.2 Magnetic force microscopy . . . 54
4.2.3 Magneto-optical Kerr effect . . . 55
4.2.4 Anomalous Hall effect . . . 55
4.3 Substrate preparation . . . 56
4.4 Sputtering deposition of CoNi/Pt and Co/Pt continuous multilayers . . . 57
4.5 Magnetic characterization of CoNi/Pt multilayers . . . 58
4.6 Magnetic characterization of Co/Pt multilayers . . . 61
4.6.1 Influence of number of bilayers . . . 61
4.6.2 Influence of substrate . . . 64
4.7 Conclusions . . . 64

5 LIL patterning of CoNi/Pt and Co/Pt multilayers 67
5.1 Schemes to fabricate arrays of dots . . . 67
5.2 Single layer process (positive photoresist) . . . 69
5.3 Vertical standing waves . . . 70
5.3.1 The use of antireflection coating (Trilevel resist process) . . . 72
5.3.2 Supra exposed single-photoresist process . . . 73
5.4 Ion beam etching . . . 74

5.5 Photoresist removal 77
5.6 The use of reversal image photoresist in combination with the hard mask process 80
5.7 Dots produced with the hard mask process 81
5.8 Conclusions 84

6 Magnetic properties of CoNi/Pt and Co/Pt patterned films 87
6.1 Coercivity in the case of a group nanomagnets 87
6.2 Analysis of CoNi/Pt dots 88
6.2.1 Thermostability of CoNi/Pt dots 90
6.2.2 Remanence and switching field distribution of CoNi/Pt dots 91
6.3 Analysis of Co/Pt dots 93
6.3.1 Thermostability of Co/Pt dots 95
6.3.2 Remanence and switching field distribution of Co/Pt dots 98
6.4 Conclusions 99

7 Conclusions 103
7.1 Minimum requirements for magnetic patterned media 103
7.1.1 Minimum energy-barrier for an idealized pattern media . 103
7.1.2 Maximum areal bit density 104
7.1.3 Minimum switching field distribution in an idealized pattern medium 104
7.1.4 Boundaries for an auxiliary writing field 104
7.2 Fabrication techniques 105
7.2.1 Substrate roughness effect in the continuous films 105
7.2.2 Number of bilayers effect in the continuous films 106
7.2.3 Photoresist stacks and vertical standing waves 106
7.3 Limitations of the fabrication techniques 106
7.3.1 Laser interference technique 106
7.3.2 Photoresist 107
7.3.3 Ion beam etching technique 107
7.4 Coercivity, switching field distribution and writability 107
7.5 Recommendations 108

Bibliography 111

A Anisotropy and energy barrier of Stoner-Wohlfarth particles 121
A.1 Field of anisotropy for a Stoner-Wohlfarth particle 121
A.2 Energy Barrier for a Stoner-Wohlfarth particle 122

Summary 125

Samenvatting 129

Resumen **133**

Acknowledgements **137**

List of publications **139**

Chapter 1

Introduction

In the last century there has been an accelerated development in information technologies, with an enhanced trend in magnetic storage systems. In order to be sustained, this accelerated development requires the creation of new technologies and devices which could allow higher storage densities, portability, lower power consumption and faster access and processing of the retrieved information.

Within this context, a brief overview of the historical development of magnetic recording is presented. Two possible pathways are here considered to keep pace with the trend in the increasing of areal bit density of magnetic recording: Perpendicular anisotropy media and patterned media. Therefore an introduction on up to date different technologies for the preparation of patterned media is given.

This introductory chapter is closed with an outline of the research described in this thesis.

1.1 Development of magnetic recording

The invention and improvement of magnetic recording has been of paramount importance. Its implementation as a tool for storage and subsequent transmission of information has consequences comparable to those of the introduction of printing.

1.1.1 Early history of magnetic recording

In 1878 Oberlin Smith visited the laboratoy of Thomas Edison and became inspired to improve the phonograph using a different principle. He decided to use a magnetizing coil to record sound on a wire instead of Edison's method of using a needle to etch a wavy groove on a wax cylinder . He did not succeed, but

he wrote an accurate description in an article published in 1888 [1]. Valdemar Poulsen in 1898 successfully realized the idea of Oberlin Smith by constructing the telegraphone [2, 3, 4].

Magnetic recording was improved in Germany after World War I. In 1927, Fritz Pfleumer thought that it could be possible to coat paper tapes with iron oxide. The paper tapes could be used as a replacement for the wires used in the telegraphone [5]. A series of improvements on the recording medium followed. By 1943, the Type L tape with a polyvinyl chloride plastic base that increased the sensitivity was introduced by BASF [5].

After World War II the American magnetic recording industry experienced an accelerated development based on the German expertise and designs. The 3M company created its magnetic tape laboratory in 1946. This laboratory discovered that needle-shaped acicular particles of gamma ferric oxide produced better coercivity (28 kA/m) than the cube-shaped particles of magnetite used before (12 kA/m) [6]. At the end of the 40s decade the American tape-recording industry was firmly established and the conditions for the introduction of magnetic recording into the computer industry were already settled down.

1.1.2 Magnetic recording for the computer industry

In 1947 , William Morris with a group of engineers in Engineering Research Associates (ERA) in Minneapolis builded the first magnetic drum for computers. The drum had a diameter of 5 inches and could store 230 bits per inch and had only one reading head. The magnetic drums offered the highest information retrieval rate over all the other storage techniques known at that time. But their storage capacity was limited [7].

In 1949, Macuhly and Eckert developed BINAC - a computer system which stored its programs in a magnetic tape. The magnetic tape had larger data storage capacity than magnetic drums, thus it became the preferred method for data storage during the 50s [8].

Three years later, Critchlow and Johnson at the laboratory of IBM in San Jose, California, were given the task to develop a storage and retrieval method, better than punched cards, drums or tapes. [6] The outcome was a system of 50 magnetic disks, all together with a storage capacity equivalent to 50 thousand punched cards or 4 million characters. The first public demonstration of this device took place in 1955 under the name of Random Access Memory Accounting Control (RAMAC) [9].

1.1.3 Hard disks for personal computers

Seagate introduced the first hard disk drive for microcomputers, known as ST506 in 1980. It had a storage capacity of 5MB and access time of 85 ms. By 1997 Sea-

gate introduced the first 7,200 RPM Ultra ATA [1] hard disk drive for desktop computers and in February 2005 they introduced the first 15,000 RPM hard disk drive, the Cheetah X15 [10]. Milestones for ATA drives follow :

- 1981 PIO 1 at 4 MB/s
- 1994 DMA 2 at 16.6 MB/s
- 1997 Ultra ATA/33 at 33.3 MB/s
- 1999 Ultra ATA/66 at 66.6 MB/s

By 1999 IBM demonstrated an areal bit density of 35.3 Gb/sqi and in 2000 IBM launched its microdrive. This drive holds one gigabyte on a disk which is the size of an American quarter. Only 20 years before, the world's first gigabyte-capacity disk drive was introduced. It was the IBM 3380, was the size of a refrigerator, weighed about 250 kg, and had a price of $40,000 [11]. The capacity of hard drives has grown exponentially over time. With the first hardisk (1980) having 5 MB capacity till nowadays external drives with 1 TB or more.

1.2 Possible pathways for further increase the areal bit density

According to the current trends in the development of information storage devices toward higher capability, portability and miniaturization, further development of hard disks must rely on higher areal densities. In the past, the introduction of the magnetoresistive (MR) sensors and lately the giant magnetoresistive sensors (GMR) had allowed for higher information densities. However, besides the possibilities of additional improvement of read / write heads the introduction of novel magnetic media is critical in increasing the areal density. The main problem to be overcome when designing novel materials for this purpose is the thermostability.

1.2.1 The problem of thermostability

Nowadays media for high density recording consists of a polycrystalline thin-film. The film is deposited on a substrate, which is covered with an underlayer to create the right structure. To achieve a high bit density the grains of a magnetic disk have to be small compared to the bit cell in order to get acceptable

[1]Advanced Technology Attachment. ATA is the most common interface used in consumer PCs. ATA is also known as IDE (Integrated Drive Electronics) in the disk drive industry.

transmission signals. For reversal of it's magnetization, the grain has to overcome an energy barrier. If the energy barrier is small a spontaneous reversal may occur due to thermal energy fluctuations. For an isolated grain the energy barrier is $K_u V$ [12], where K_u is the uniaxial anisotropy constant and V is the volume of the grain. If the grains become very small, the magnetization will be unstable and they will not be anymore suitable for storing information. This phenomenon is called the *superparamagnetic effect*.

1.2.2 Perpendicular recording

In longitudinal recording, due to demagnetizing field effects, adjacent magnetic bits require larger transition distances than perpendicular magnetic bits [13]. Lower transition distances allow for increased bit densities in perpendicular media.

Additionally, the medium can be thicker because the head field penetrates deeper into the medium and because in thicker films the demagnetizing fields decrease. Therefore at the same density the volume of the bits can be increased. Moreover, the head geometry allows for higher fields, so also the anisotropy of the medium can be increased.

Perpendicular recording has been a subject of research since the last three decades. In March 2005, Hitachi Global Storage Technologies demonstrated an areal density of 230 gigabits per square inch on a perpendicular medium device, the highest areal density achieved to date based on perpendicular recording. In August 2005 Toshiba introduced the first hard disk drive based on perpendicular magnetic recording into the market.

Perpendicular recording (PMR) has been predicted for a density of 1 Tb/sqi [14].

1.2.3 Patterned media

In present commercial hard disks technologies the information is stored as a magnetization pattern within a film consisting of weakly coupled grains. In order to get reasonable signal-to-noise ratios every bit covers an area containing hundreds of grains. Further increase in storage density would therefore require a reduction of grain volume V leading to superparamagnetic behaviour [13].

A possible solution is to use patterned magnetic medium consisting of a regular matrix of isolated single domain nanomagnets [15, 16, 17]. In such a discrete recording medium every dot represents one bit. This would allow for a higher bit density. The comparison between the conventional way of magnetic recording and patterned medium is presented in Figure 1.1. From this it becomes clear that the highest density is present in the patterned medium. Moreover, the super-paramagnetic bit density limit of this type of medium is much higher

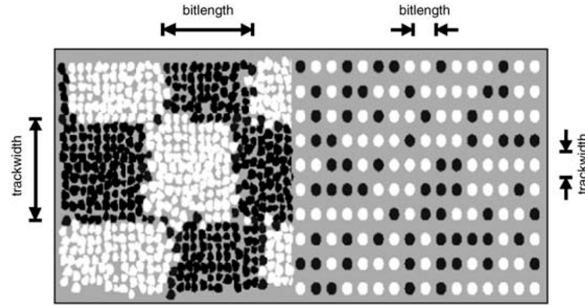

Figure 1.1: *Comparison continuous media (100 crystals per bit) and pattern media (1 dot=1 bit).*

than that of present thin film media. Micromagnetic simulations indicate that a patterned medium with perpendicular magnetic anisotropy would display less noise than a continuous one [18].

In continuous magnetic media bits can be recorded at any area. But in the case of patterned media the write pulse must be synchronized to the patterning [19]. Synchronization requirements impose constraints to the switching field distribution of the media and the writing head gradients. Perpendicular single pole heads in combination with a soft underlayer have been suggested as well [20].

1.3 Methods for preparing patterned media for magnetic recording

The fabrication of a matrix of well defined nanomagnets over a large area demands novel patterning techniques. Extensive discussions on novel patterning technologies have been publishes recently [21, 22, 23, 24]. An outlook of those up-to-date patterning methods is offered in this section.

1.3.1 Ion beam nano-structuring

It is possible to pattern a continuous magnetic film by using an ion beam. When ions are bombarded against a material's surface, the material can undergo certain modifications. For instance, the ions can damage the crystal lattice of the material, the ions can also chemically react with the material itself or being implanted into the crystalline structure. Material can also be removed out of the attacked surface. The resulting effect depends on the type of ions, the energy given to the ions and the exposure doses.

Ion beam nano-structuring with a mask

Combining a broad ion beam with a lithography mask allows to produce patterns on a continuous magnetic material. The mask can be produced by standard photolithography, electron beam lithography or Laser Interference Lithography (LIL) (see Chapter 3). The influence of ion irradiation on Co/Pt multilayers, which present perpendicular anisoptropy [25], has already been studied in detail [17]. When irradiating a Co/Pt multiayered sample with He ions, the sample does not get etched but the perpendicular anisotropy, coercivity and Curie temperature are decreased [26]. Studies on Co/Pt multilayers show that the decrease of coercivity and perpendicular anisotropy K_u as a function of irradiation dose with different ions species is associated with intermixing of the Co/Pt interfaces. In conclusion, by using ion irradiation in combination with a mask it is possible to locally modify the magnetic properties of a Co/Pt multilayered film while preserving the original magnetic properties in the areas protected by the mask.

Ion projection

Another ion irradiation method consists in using a mask which is not in contact with the sample to be patterned. It is possible to focalize the ion beam in such a way that the mask pattern is transferred into the magnetic medium with a demagnification factor of 4. This technique has been used in the fabrication of circular tracks for patterned magnetic discs prototypes [27].

Focused ion beam etching

Patterning can also be performed by Focused Ion Beam Etching (FIBE). In this case a thin ion beam is focused and it is used to remove material by milling. FIBE constitutes a maskless patterning technique. It posses a high precision on the structures that can be etched. Small and well define structures can be fabricated: for instance, dots with 20 nm spacing have been created in this way [28]. One of the disadvantages of this technique is that it cannot cover as large areas as standard photolithography or LIL and it is a time consuming technique. By using FIBE arrays covering areas of 2×2 μm2 have been prepared on CoCrPt [29] and bit densities larger than 140 Gb/sqi have been demonstrated.

1.3.2 Nano-imprint

Imprint technology offers a high resolution and it is in principle less expensive than conventional photolithography. Fabrication of periodic structures over large areas by means of nano-imprint is described by McClelland et al. [30].

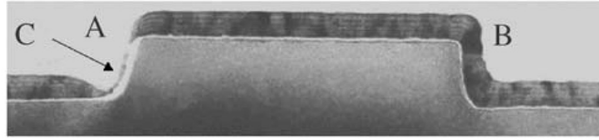

Figure 1.2: *TEM cross-section image of a Si dot with a height of 36 nm and a width of 100 nm covered with a Co/Pt multilayered film [32].*

Metallic dots with diametres of 10 nm and periodicites of 40 nm have been realized by this technique. Dot SiO_2 pillars with periodicites down to 30 nm have been fabricated by using a combination of electron beam lithography, nanoimprint, lift off technique and reactive ion etching [31]. Those SiO_2 pillars could be used as molds for magnetic patterned media with densities of 700 Gb/sqi.

1.3.3 Pre-patterned substrates

Si or SiO_2 substrates can be patterned by standard photolithography, electron beam lithography or LIL in combination with reactive ion etching. Once the substrate surface has been patterned, it is possible to deposit magnetic material by oblique evaporation. In this way it is possible to obtain an array of nanomagnets. Figure 1.2 shows a TEM cross-section image of a Si dot with a Co/Pt multilayer deposited on top of it. In this case the Co was deposited normal to the surface while the Pt was deposited at an oblique incidence from the right. Thus, Pt has been deposited on the side wall B but not on the side wall A. On side wall A a very thin layer of Co oxide has been formed. In the groove opposite to the Pt source a discontinuity in C can be seen due to the shadowing of Pt by the Si dot. It can be concluded that both side walls are non-magnetic, consequently there is no direct exchange between the top and the bottom of the grooves [32].

1.3.4 Self-assembling structures

Periodic polymeric structures formed on top of a continuous magnetic film can serve as etching masks. Block copolymers consists of polymer chains made from two chemically distinct polymeric materials. After phase separation of the blocks the resulting material self assembles into areas with periodic structure. In order to achieve large areas with the same *lattice* orientation it is possible to grow the self assembling polymer along grooves. By this technique 40 nm diameter CoCrPt dots aligned in a spiral pattern have been etched on a 2.5 in glass plate [33].

Recently a new recording approach based on self-assembled FePt nanoparticles has been reported [34]. The nanoparticles are chemically synthesized. When

the particles are spread out on a substrate the carrier solvent can evaporate and the particles self assemble into an ordered lattice with controlled spacing. After an annealing process the FePt nanoparticles get into an $L1_0$ phase. This phase presents a large anisotropy which is necessary to ensure thermal stability of written information. The resulting self-assembled film can be regarded as a recording medium . The particle size can be controlled for 3 to 10 nm. This kind of lattices have a great potential as future storage media.

1.3.5 Interference lithography

It is possible to create an interference pattern by splitting a coherent beam and recombining it afterwards. The periodicity of the resulting interference pattern depends on the angle of incidence of the recombined sub-beams and their wavelength (Refer to Chapter 3). If the interference pattern is projected onto a photoresist one obtain periodic lines (a grating) of exposed resist. If after a first exposure the substrate is rotated by 90 °and a second exposure performed, then it is possible to produce dots arrayed in a squared lattice after developing the photoresist.

Laser Interference Lithography is the chosen technique for the samples fabricated and analysed in this work. It is a fast and mask-less technique. The exposure requires from a few second till 2 minutes depending on the kind of photoresist and desired pattern periodicity. The exposed area depends on the diameters of the interfering beams. Typically, it is possible to expose regular arrays of periodic nano-structures over areas of few square centimeters. This technique will be extensively described in Chapter 3.

1.4 Outline of this thesis

We have already mentioned different possible pathways in order to obtain a magnetic medium which could hold a large information density. The scope of this thesis consist of the exploration of the feasibility of one of these pathways. Fabrication and magnetic characterization of patterned films with perpendicular anisotropy has been carried out. We have realized patterned magnetic nanodots arranged in square and hexagonal lattices with periodicites ranging from 600 nm down to 300 nm, which corresponds to bit densities from 1.8 Gb/sqi up to 7.2 Gb/sqi. The main aim has been focused towards the understanding of the problems involved in the fabrication of large samples (1×1 cm till 3×3 cm) and their write-ability. Gaining insight into this two issues will allow for handling more efficiently additional difficulties which could arise when downsizing the arrays features, in the aim to reach higher bit densities.

In Chapter 2 we discuss about the magnetic properties of an idealized magnetic pattern medium. Issues as the thermal stability, required magnetic anisotropy, bit to bit interaction and its consequences for the material's switching field distribution are considered. Laser Interference Lithography has been the technique chosen to produce the patterned media samples studied in this work. This tool is presented in Chapter 3. Chapter 4 concerns the deposition technique and magnetic properties of continuous CoNi/Pt and Co/Pt films, which were the films which were patterned. In Chapter 5, the patterning process of the continuous magnetic films is presented. In order to produce magnetic patterned media we have chosen to expose the desired arrays by LIL on a photoresist which after development will serve as an etching mask. A discussion about different photoresist stacks which were used in the course of this work is presented. Finally we close this chapter with a discussion on the etching process and the photoresist removal afterwards. Chapter 6 concerns the analysis of the patterned magnetic structures. Three issues are mainly discussed there. The possible damage to the magnetic properties of the material due to the fabrication process, in particular the ion beam etching step and the subsequent removal of the residual photoresist. The switching field distribution displayed by the samples and possible ways to reduce it are part of the second section of that chapter. Finally we examine the thermostability of our samples. The results presented in this work are finally synthesized in Chapter 7, where we discuss on the feasibility of a pattern magnetic medium which could be incorporated in an ultra-high density storage device. Difficulties in writing and retrieving actual information will be commented there. Possible lines for further research are sketched.

Chapter 2

Characteristics for a magnetic patterned medium for information storage

An ideal magnetic patterned medium with potential application in probe recording is presented in this chapter. The medium is considered to be compound of identical elements arranged in a squared periodic lattice.

First we present a discussion giving a general description of the medium. Then follows a discussion on the thermostability, where aspects as switching probability of individual elements in the array are considered. From it, calculated values for the relaxation time are given.

Raw bit error rate is also discussed and an acceptable energy barrier to thermal energy ratio is estimated from it.

Numerical estimations are presented on the subject of required switching fields for individual magnetic elements depending on the magnetization state of neighbouring elements.

A discussion on the required anisotropy and magnetization saturation is also presented.

The dimensions of a reading/writing probe are considered. It is concluded the necessity of an auxiliary field in order to be able to write. Limits to this auxiliary field are given (upper and lower limits).

2.1 General description

To achieve higher information densities it is necessary to decrease the bit size. However the super-paramagnetic effect arises as an obstacle to decrease indefinitely the bit size on present magnetic recording media [35] (e.g. hard disks).

Patterned magnetic materials composed of arrays of single domain elements with uniaxial perpendicular anisotropy have been proposed, besides others, as a possible solution to overcome this problem [23].

The general requirements for an ideal patterned medium can be summarized as follows:

- 1 dot [1] = 1 bit principle
- bits arrayed in a 2D regular matrix
- dots should possess only two (well defined) remanent states
- the magnetization of the dots should remain stable for a long time (i.e. the magnetization of the dots should be thermally stable)
- the dots should be as *identical* to each other as possible
- the dipolar interaction between the magnetic elements (cross-talk) should be minimized.

According to these requirements we will consider a patterned medium in which each dot is identical to each other and behaves as a *Stoner-Wohlfarth* (SW) particle.

Additionally, we will consider that the anisotropy axis of these particles is perpendicular to the medium surface and that they are arranged in a square lattice.

Besides that, because of the patterned medium fabrication characteristics imposed by the LIL and IBE processes, we will consider that the magnetic dots are cylindrical and their diameter is one-third of their pitch or periodicity (distance from one element center to another). For the sake of simplicity, the shape anisotropy contribution to the total anisotropy will be neglected. We will also consider that the reading/writing probe (MFM tip) has the shape of a long cylinder.

2.2 Thermostability of arrays of dots

The switching mechanism of a magnetically anisotropic particle can be described as a process in which, starting from one equilibrium state of magnetization, it is necessary to overcome an energy barrier to bring the particle into another equilibrium state of magnetization. The origin and characteristics of the energy barrier are a property of the material, but its magnitude depends on external variables which can be experimentally controlled such as an applied magnetic field or temperature.

[1] From now on, we will use the term *dot* to name an element of the periodic array in the proposed patterned medium.

2.2.1 Probability of switching

Consider a group of dots which posses only two equilibrium states A and B, we will neglect by the moment any interaction among them. Initially all of them are in the local equilibrium state A. The rate of switching (r) from state A into state B can be described (statistically) by the following expression,

$$\frac{dq_A}{dt} = -rq_A, \qquad (r > 0) \tag{2.1}$$

where $q_A = q_A(t)$ and represents the number of dots in state A at a given time t. From (2.1) it follows that

$$q_A(t) = q_A(0)e^{-rt} \tag{2.2}$$

The ratio $q_A(t)/q_A(0)$ represents the fraction of dots which will still remain in state A at a time t (where the initial time is assumed to be $t = 0$). From the statistical point of view, such a fraction corresponds to the probability of a particle to continue in state A after a time t, i.e.

$$p_A(t) = \frac{q_A(t)}{q_A(0)} = e^{-rt}. \tag{2.3}$$

and of course

$$p_B(t) = 1 - p_A(t) = 1 - e^{-rt}. \tag{2.4}$$

2.2.2 Rate of switching

The rate of switching is not a constant value but rather a function of the energy barrier and the temperature. It can be phenomenologically described by the Arrhenius relation [36],

$$r = f_0 \exp\left(-\frac{\Delta E}{kT}\right), \tag{2.5}$$

where f_0 is the thermal attempt frequency, commonly assumed to be $10^9 s^{-1}$[37] [38] ΔE is the energy barrier, k is the Boltzmann's constant, and T the temperature.

Thus, the rate of switching (as described by the Arrhenius relation) is proportional to the fraction of particles in the system which posses an energy level

higher than the energy barrier ($exp(-\Delta E/kT)$) and the number of attempts per unit of time to 'jump' into another energy level.

By combining (2.4) and (6.2) we obtain the expression of the switching probability,

$$p_B(t) = 1 - \exp\left(- f_0 t \exp\left(- \frac{\Delta E}{kT} \right) \right). \tag{2.6}$$

2.2.3 Relaxation time

The relaxation time τ is defined as the required time for p_A to be $1/e$. Thus, according to (2.4) and (2.6)

$$p_A(\tau) = \exp\left(- f_0 \tau \exp\left(- \frac{\Delta E}{kT} \right) \right) = 1/e$$

$$\Rightarrow \tau = \frac{1}{f_0} \exp\left(\frac{\Delta E}{kT} \right) \tag{2.7}$$

From the equation above it is possible to calculate the variation of the ratio $\Delta E/kT$ as a function of the relaxation time τ, as is shown in table 2.1. Because of the exponential dependence shown in (2.7) it is possible to see in table 2.1 that small variations in the energy-barrier-to-thermal-energy ratio ($\Delta E/kT$) are related to variations of different orders of magnitude in the relaxation time (τ). Thus we have, for instance, that for a relaxation time of 1 second corresponds a value of $\Delta E/kT$ equal to 20.7, while in the case of a relaxation time of 1 year (315,360,000 seconds) corresponds a value of 40.3 (about twice the former value).

In 1997, Charap et al. [39], while studying the thermal stability of recorded information on high-density conventional hard-disks media, considered bits consisting of many grains all of them behaving as perfect SW particles and without magnetic interaction with each other. They determined a *stability criterion* of 95% of magnetization retention on written bits after six months. This criterion corresponds to a $\Delta E/kT$ ratio of 40.27 and its correspondent relaxation time τ is 10 years.

2.3 Raw bit-error rate

The *raw bit error rate* (BER) is the number of defective bits divided by the total number of bits contained on a storage medium. This should not be confused with the *adjusted bit error rate* which is the number of missing or erroneous

τ	$\Delta E/kT$
1 second	20.7
1 minute	24.8
1 hour	28.9
1 day	32.1
1 month	35.5
1 year	38.0
10 years	40.3
100 years	42.6
1000 years	44.9

Table 2.1: *Energy-barrier-to-thermal-energy ratio ($\Delta E/kT$) as a function of relaxation time (τ)*

bits divided by the total of read bits after recovering some of the defective bits through error correction algorithms (most of those algorithms make use of the inclusion of extra check bits in each stored word). Adjusted BER's are much smaller than raw BER's, typically in the range from 10^{-8} (one missing or erroneous bit per 10^8 read bits) to 10^{-12} . In magnetic recording, typical raw BER's range from 10^{-4} to 10^{-5} and in the case of optical media the typical values go from 10^{-5} to 10^{-6}.

In our ideal storage medium, we assume (as mention before) that all dots are identical to each other, so in principle, there are no defective physical dots. But even so, there will be defective bits. Those will be the bits that *spontaneously* switch their magnetization as a result of overcoming the energy barrier. They will account for a raw BER which will be time dependent.

Let's us consider that we are aiming for a raw BER ϵ in between 10^{-4} and 10^{-6} 5 years after writing some information.

So, the relaxation time will be given by

$$\tau = \frac{1}{r} = \frac{t}{\ln\left(\frac{1}{1-\epsilon}\right)}, \tag{2.8}$$

The ratio $\Delta E/kT$ can be obtained from (2.4)

$$\frac{\Delta E}{kT} = \ln(f_0 \tau) \tag{2.9}$$

Table 2.2 shows the values of the calculated parametres τ and $\Delta E/kT$ for three different values of ϵ. We conclude that a patterned magnetic material which could be useful for storing information during at least five years and with a minimum acceptable raw BER according to nowadays standards should fulfill

BER	τ (years)	$\Delta E/kT$
10^{-4}	5×10^{4}	48.8
10^{-5}	5×10^{5}	51.1
10^{-6}	5×10^{6}	53.4

Table 2.2: *Relaxation time (τ) and energy-barrier-to-thermal-energy ratio ($\Delta E/kT$) as function of the raw bit error rate (BER)*

the condition that

$$\frac{\Delta E}{kT} \geq 48.8 \tag{2.10}$$

2.4 Energy barrier

In the previous section we derived a minimum value of 48.8 for the *energy-barrier to thermal-energy ratio*. The value of kT in the denominator of (2.10) is already fixed, since we will require that our storage device should operate at room temperature or slightly above. So, any further effort in order to design a suitable magnetic storage medium relies on the value of its energy barrier.

From (2.10) it follows that

$$\Delta E \geq 2.02 \times 10^{-19}\ \mathrm{J} \tag{2.11}$$

The energy barrier of a Stoner-Wohlfarth particle is described by the following expression[37][2]:

$$\Delta E = U\left(1 - \frac{H}{H_0}\right)^2, \tag{2.12}$$

where U represents the energy barrier at zero field and zero temperature (also known as the *internal energy*), H_0 is the *anisotropy field* and H represents all the fields external to the particle, in particular

$$H = H_d + H_{tip}, \tag{2.13}$$

where H_d represents the field applied over the particle due to all the other magnetic particles present in the array and H_{tip} is the field due to the presence

[2]Please refer to appendix for the details on deduction of equation (2.12)

of the magnetic probe(s) which will be used to read and write over each dot. For the moment only the field H_d will be considered. The field H_{tip} will only be considered during the write- or read operations .

2.5 Dot to dot interactions: demagnetizing field

First we will consider the field H_d due to the presence of one single dot. Analogue to electrostatic calculations, the field can be calculated from the magnetostatic potential ϕ as [40]

$$\overrightarrow{H}_d = -\nabla\phi, \qquad \text{with} \qquad \phi = \frac{1}{4\pi}\iiint \frac{\nabla\cdot\overrightarrow{M}}{R} dV + \frac{1}{4\pi}\iint \frac{\hat{n}\cdot\overrightarrow{M}}{R} dA. \tag{2.14}$$

In the case of a cylinder with radius r_0, height $2z_0$ and uniform magnetization density $\overrightarrow{M} = (0,0,M)$, whose center is at the origin of the coordinate system, the field at the point $(x_0,0,0)$ is given by,

$$\overrightarrow{H}_d = -\frac{\hat{n}\cdot\overrightarrow{M}}{2\pi}\int_0^{2\pi}\int_0^{r_0} \frac{r z_0}{(x_0^2 + z_0^2 + r^2 - 2rx_0\cos\varphi)^{\frac{3}{2}}} dr d\varphi \hat{\mathbf{z}} \tag{2.15}$$

We can rewrite equation (2.15) in a dimensionless scalar form as

$$\frac{H_d}{M} = \frac{1}{2\pi}\int_0^{2\pi}\int_0^{r_0} \frac{r z_0}{(x_0^2 + z_0^2 + r^2 - 2rx_0\cos\varphi)^{\frac{3}{2}}} dr d\varphi. \tag{2.16}$$

In accordance to the proportionality between the different system dimensions, it is possible to perform the following substitutions; $r_0 = g\Lambda$ (in this case g=1/6, since we set the dot diameter as one third the periodicity distance), $z_0 = r_0 b$ (where b is the height-to-diameter ratio of the dot) and $x = a\Lambda$, where a is a scaling factor, so we can express all the dimensions in terms of the periodicity Λ. By applying a change of variable in the form

$$r = \Lambda r' \quad \text{and} \quad dr = \Lambda dr' \tag{2.17}$$

and substituting the values for z_0 and r_0 we get

$$\frac{H_d}{M} = \frac{gb}{2\pi}\int_0^{2\pi}\int_0^{g} \frac{r'}{(a^2 + (gb)^2 + r'^2 - ar'\cos\varphi)^{\frac{3}{2}}} dr' d\varphi. \tag{2.18}$$

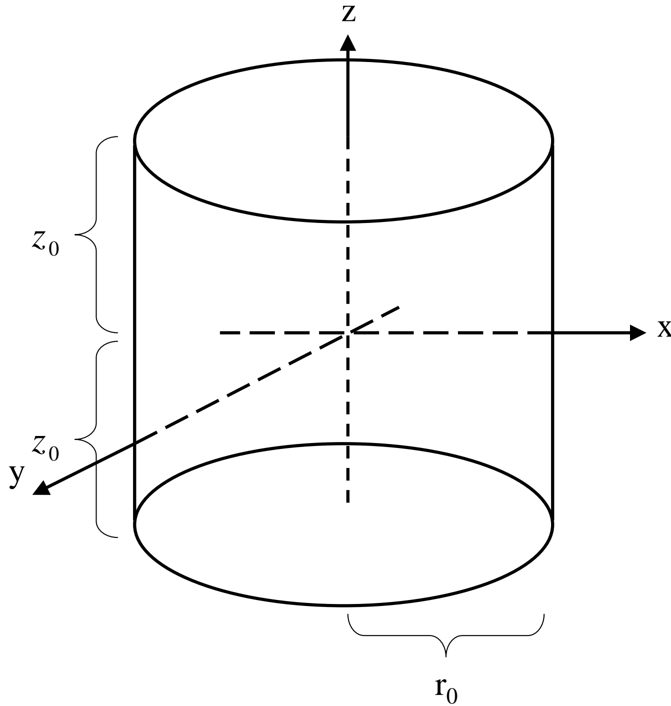

Figure 2.1: *Diagram showing the feature sizes considered in the modelled cylindric dot*

It should be noted that g and b are both fractions. As mentioned before we will consider that $g = 1/6$, while the variable b will be allowed to vary in the rage $0 \leq b \leq 1$. Thus $(gb)^2 \leq 1/36$. On the other hand, the scaling factor a will be relevant for us only when $a \geq 1$, since we are interested in the interaction field of the neighbouring dots and the first four neighbours are already at a distance of $1 \times \Lambda$. So, we have that $a \geq 1/36 \geq (bg)^2$ so we can assume $a \gg (bg)^2$ and approximate (2.18) to

$$\frac{H_d}{M} \approx \frac{gb}{2\pi} \int_0^{2\pi} \int_0^g \frac{r'}{(a^2 + r'^2 - 2ar' \cos\varphi)^{\frac{3}{2}}} dr' d\varphi \tag{2.19}$$

We will consider now the influence of the surrounding dots over the demagnetizing field experienced by one single dot. The maximum exerted demagnetizing field occurs when all the surrounding dots are magnetized in the same direction as the analysed dot . The influence of a dot decays rapidly ($\sim 1/r^3$) with the distance. So, in sake of simplicity, only the surrounding dots up to the

Dots in a square grid				
Neighboring order	Number of neighbors	Distance in terms of Λ	Individual contribution (H_d/Mb)	Contribution per neighboring order (H_d/Mb)
1	4	1	0.002389	0.009557
2	4	$\sqrt{2}$	0.000831	0.003326
3	4	2	0.000292	0.001167
4	8	$\sqrt{5}$	0.000208	0.001667
5	4	$2\sqrt{2}$	0.000103	0.000411
Total contribution				0.016127

Table 2.3: *Contribution of the surrounding dots to the demagnetizing field in terms of the ratio H_d/Mb with g fixed to $1/6$*

fifth neighbouring order will be considered in the analysis. In table 2.3 the contributions to the demagnetizing field in terms of H_d/M and b are displayed for a fixed value of $g = 1/6$. The table was constructed by using expression (2.19). The first column of table 2.3 shows the neighbouring order. The second column indicates the number of dots belonging to certain neighbouring order. The third column corresponds to the distance between the addressed dot and its neighbours, this distance is given as a multiple of the parameter Λ (periodicity of the array). The fourth column shows the contribution to the demagnetizing field of a single dot over the addressed dot in terms of the dimensionless ratio H_d/Mb, where H_d is the demagnetizing field itself and the product $M \times b$ corresponds to the total magnetization density per unit of surface of the dots. The fifth column gives the contributions per neighbouring order, which corresponds to the value displayed in the fourth column times the value displayed in the second column. At the bottom of the fifth column there is a cell labelled *total contribution* which is the addition of all the individual dot contributions up to the fifth neighbouring order. It can be noted from table 2.3 that the contribution of all the second nearest neighbours represents around 34% of the contribution of the first order (nearest) neighbours. The contribution of the third, fourth and fifth order neighbours represents about 12%, 13% and 4% (respectively) of contribution of the first order neighbours. The value of the total *field-to-magnetization ratio* contribution will be used below when defining the constant $\tilde{n}$ in (2.20). This information will be used in the rest of the analysis.

From table 2.3 we take the field-to-magnetization ratio contribution of the neighbouring dots as

$$\tilde{n} = \frac{H_d}{Mb} = 1.6127 \times 10^{-2} \Rightarrow H_d = \tilde{n}bM, \tag{2.20}$$

Note that $\tilde{n}$ is a function of the ratio between dot diameter and dot spacing g.

2.6 Anisotropy and magnetization saturation

At this point we would like to find an expression for the energy barrier (ΔE) in terms of the anisotropy (K) and magnetization saturation (M) of the material used to fabricate the patterned medium. In order to achieve this expression we will use results already found in section 2.4 and section 2.5.

Substituting the last result, (2.20), into (2.11) and using (2.12) we obtain

$$\Delta E = U\left(1 - \frac{\tilde{n}bM}{H_0}\right)^2 \geq 2.02 \times 10^{-19}\ \mathrm{J} \tag{2.21}$$

But we know that[3] $H_0 = \frac{2K_u}{\mu_0 M_s}$ and $U = KV$, then

$$\Delta E = KV\left(1 - \frac{\tilde{n}b\mu_0 M^2}{2K}\right)^2 \geq 2.02 \times 10^{-19}\ \mathrm{J}\ . \tag{2.22}$$

Since V is the volume of the dot, we obtain

$$V = \pi r_0^2 \cdot 2z_0 = \pi \cdot g^2\Lambda^2 \cdot 2bg\Lambda = 2\pi b g^3 \Lambda^3 \tag{2.23}$$

So, it is possible to rewrite (2.22) as

$$\Delta E = 2\pi b g^3 \Lambda^3 K\left(1 - \frac{\tilde{n}b\mu_0 M^2}{2K}\right)^2 \geq 2.02 \times 10^{-19}\ \mathrm{J}\ . \tag{2.24}$$

We now have an expression for the energy barrier in terms of the magnetization (M_s) of the material, its anisotropy constant (K) and the periodicity (Λ) of the dots which is directly related with the information density in the system. From (2.24) it is possible to observe that as the anisotropy constant increases, the energy barrier also will increase. However, given a specific value for K, there is a maximum value for M_s in order to keep the expression (2.24) valid.

Material	K (kJ/m^3)	M (kA/m)
Ni [a]	75	480
TbFeCo [b]	100	100
$BaFe_{12}O_{19}$ [c]	330	380
Co (hcp)	450	1420
$Co_{50}Ni_{50}$/Pt [d]	480	500
Co (fcc) [a]	640	1420
FePd $L1_0$ [e]	660	1050
Fe [a]	920	1700
Co/Pt [f]	950	1750
FePd $L1_0$ [g]	2100	1050
FePt $L1_0$ [e]	6600	1070
FePt $L1_0$ [g]	7000	1070

[a]Values given for shape anisotropy of quasi-infinitely elongated pillars (aspect ratio$\gg$1). [41]
[b]Value from [42].
[c]Single-crystal [43]
[d]Value from [41]
[e]Experimental value, from [44].
[f]Value from [45]
[g]Theoretical value, from [44]

Table 2.4: *Values for the anisotropy constant and the saturation magnetization of different materials*

Figure 2.2 displays a series of plots for the maximum allowed M_s as a function of the anisotropy K for different bit density values considering a dot aspect-ratio of $b = 1/2$. The dots in the graph correspond to the magnetic materials that are mentioned in table 2.4. Those dots below a given curve represent (according to this model) the materials which are useful for storing information with a raw bit error rate lower than 10^{-4} per five years. It can be observed that the $Co_{50}Ni_{50}$/Pt multilayer which is used in this thesis, is not a suitable material for media with a bit density of 1 Tb/sqi according to the criteria we have defined earlier. But the Co/Pt multilayer, which is also used in this thesis, is on the edge of fulfilling the requirements. The most promising candidate FePt ($L1_0$ phase) could yield a maximum bit density of approximately 4.1 Tb/sqi.

Figure 2.3 displays curves for the maximum allowed M_s as a function of the anisotropy K for different bit density values considering an aspect ratio of $b = 1$.

It can be seen in the figure that at an aspect ratio of 1, CoNi/Pt multilayers might be capable of supporting 1 TBit/in^2, whereas Co/Pt multilayers safely fullfill the requirements. With FePt layers and a dot ascpect-ratio $b = 1$ it could

[3]Refer to appendix for details concerning derivation of expressions $H_0 = \frac{2K_u}{\mu_0 M_s}$ and $U = KV$

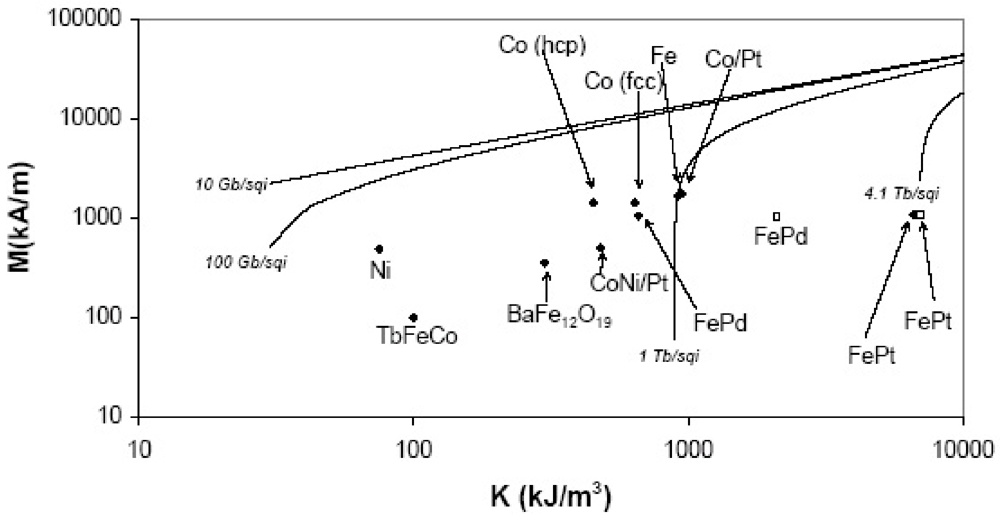

Figure 2.2: *Maximum value of M at an aspect ratio of $b = 1/2$ as a function of the anisotropy constant K for different bit densities. Holed squares stand for calculated values while solid diamonds indicate experimental data.*

be possible to achieve a bit density of 6.5 Tbit/sqi.

Figure 2.4 shows curves defining the maximum allowed values of M_s for a bit density of 1Tb/sqi as a function of the anisotropy K. Each curve corresponds to a different dot aspect-ratio (b). In the case of $b = 1/8$ the only material which could yield a density of 1Tb/sqi is the FePt, while at an aspect ratio of $b \geq 1$ CoNi/Pt and Co/Pt qualify for this density. In the case of an aspect ratio of $b \geq 2$ even dots made of pure Co(hcp) could be used for a media with the 1Tb/sqi density.

For higher aspect ratios, the model depicted in this work is not adequate any more due to the approximation made in (2.19).

In figure 2.5 two materials are considered: the Co/Pt multilayer and FePt ($L1_0$ phase). The energy barrier as a function of the bit density for two different aspect ratios ($b = 1$ and $b = 1/10$) is displayed. It can be seen that an aspect ratio of $b = 1/10$ the bit-density limit for Co/Pt is 0.4Tb/sqi and for FePt the bit-density limit is 1.3 Tb/sqi. In the other hand, at an aspect ratio of $b = 1$ the density limit for Co/Pt is 1.6 Tb/sqi and for FePt 7 Tbit/sqi. Producing dots at high aspect ratios could improve the thermal stability since the volume of magnetic material per dot is higher and it contributes to increase the energy

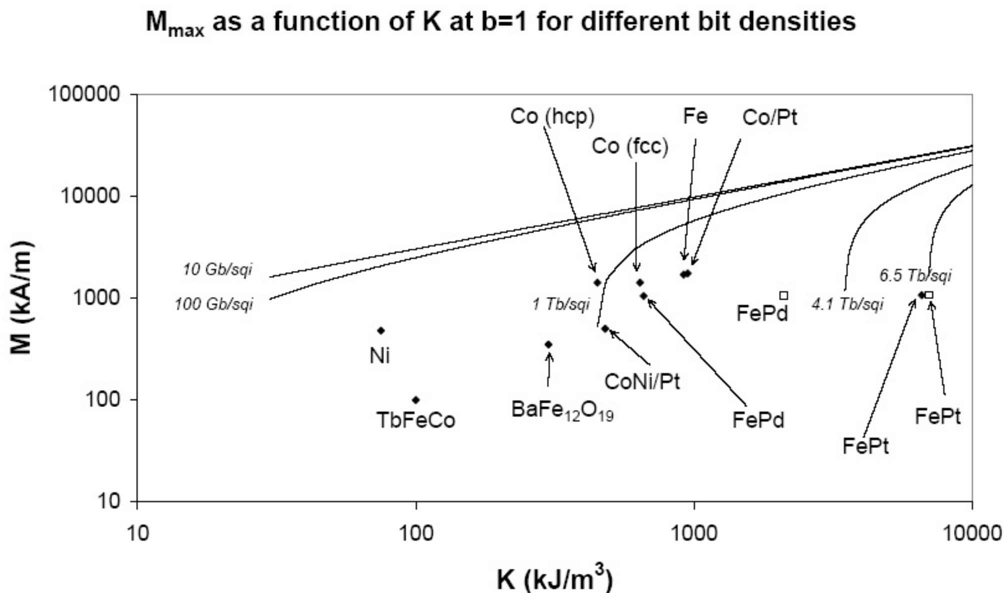

__Figure 2.3:__ Maximum value of M at an aspect ratio of $b = 1$ as a function of the anisotropy constant K for different bit densities. Holed squares stand for calculated values while solid diamonds indicate experimental data.

barrier. Using soft magnetic underlayers will produce a similar effect.

2.7 Energy barrier distribution

The former calculations were performed by considering a dot energy barrier equal or higher than $2.02 \times 10^{-19} J$, as given in expression (2.24). This expression was obtained by assuming that the dot under consideration was in the least stable situation, which happens when all the surrounding dots are magnetized in the same direction. The value of the energy barrier calculated in this way will be renamed as ΔE_{min}. On the other hand, if we aim to write on a dot (i.e. we want to change its state of magnetization), then the most pessimistic scenario will be when the dot is in its most favourable thermal-stable situation, which happens when all the surrounding dots are magnetized in the opposite direction. The value of the energy barrier for this most stable situation will be named as ΔE_{max}. There are many other energy barrier levels for a single dot depending on the magnetization states of its neighbours. In other words in this idealized medium, the energy barrier is not always the same from dot to dot. But there is an energy barrier distribution whose extremes are given by ΔE_{min} and ΔE_{max}. In absence of external interactions the extreme values are given

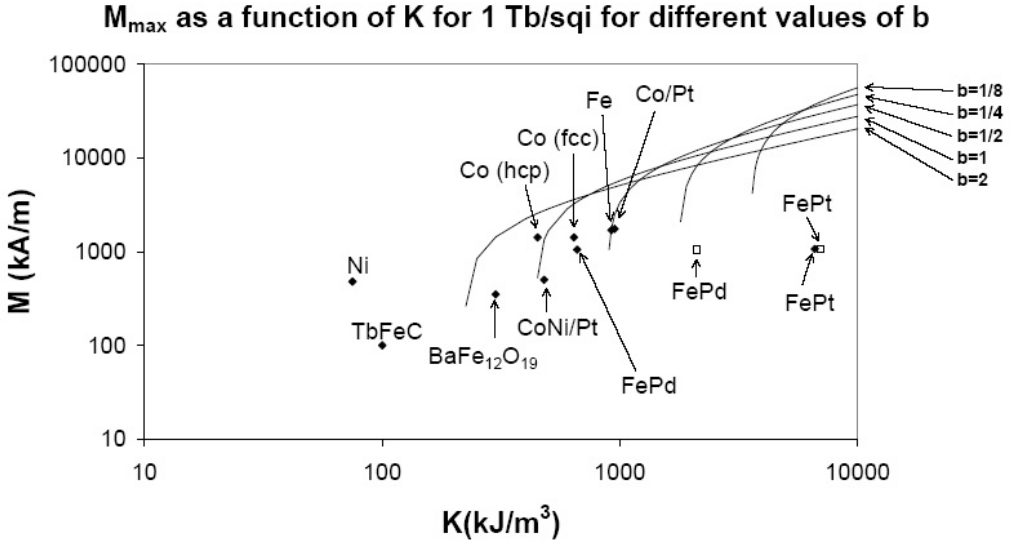

Figure 2.4: Maximum value of M at a density of $1Tb/sqi$ as a function of the anisotropy constant K for different dot aspect ratios values b. Holed squares stand for calculated values while solid diamonds indicate experimental data.

as follows

$$\Delta E_{min} = U\left(1 - \frac{H_d}{H_0}\right)^2 \quad \text{and} \quad \Delta E_{max} = U\left(1 + \frac{H_d}{H_0}\right)^2 \tag{2.25}$$

2.8 Probe to dot interactions

In previous sections we have discussed on the energy barrier of a single dot and how this is affected by interaction with the surrounding dots. In this section we will discuss another interaction. We will consider the interaction of a magnetic probe with the addressed dot and with the neighbouring dots as well.

2.8.1 Switching field distribution

The magnitude of the energy barrier of a dot will be affected in the presence of a magnetic probe, which could be used for writing information on the dots (i.e. changing their magnetization state). By considering the *probe-to-dot* interaction

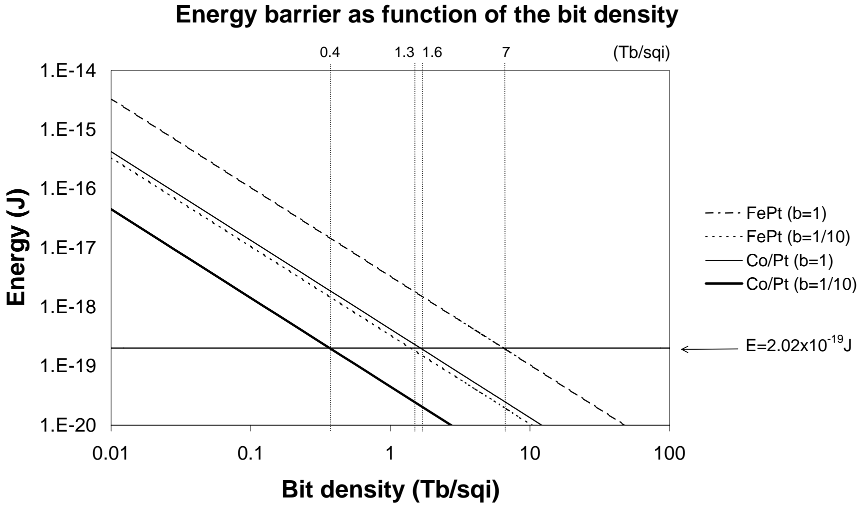

Figure 2.5: *Energy barrier as a function of the bit density at the aspect ratios of $b = 1/10$ and 1 for CoNi/Pt multilayer (experimental) and $L1_0$ FePt(theoretical).*

it is possible to write more general expressions out of equations (2.25) as

$$\Delta E_{min} = U\left(1 - \frac{H_d + H_{tip}}{H_0}\right)^2 \quad \text{and} \quad \Delta E_{max} = U\left(1 + \frac{H_d - H_{tip}}{H_0}\right)^2 \tag{2.26}$$

In this context, a writing-operation will be executed on a dot when its energy barrier is lowered so that the chance of switching in the time the tip is present is almost one.

Equalizing the expressions in (2.26) to zero, we get that

$$H_{min} = H_0 - H_d \qquad \text{and} \qquad H_{max} = H_0 + H_d, \tag{2.27}$$

We conclude that, analogue to the energy barrier, there is a switching field distribution whose extremes are given by H_{min} and H_{max}. By using (2.20) we

obtain the distribution width

$$H_{max} - H_{min} = 2H_d = 2\tilde{n}bM \tag{2.28}$$

We can notice that even when in this ideal medium the dots are identical to each other in their intrinsic properties, still they will show differences in their switching field. We can see from (2.28) that the switching field distribution width is proportional to the magnetization saturation of the magnetic dots.

2.8.2 Probe dimensions: necessity of a complementary technique in probe recording

Let us assume that the probe we use has the shape of a very long rod (semi-infinite cylinder). We will also assume that the writing process will be performed by tapping, so we will consider that the tip at a certain moment makes contact with the dot. We can calculate the minimum probe diameter from the maximum required field H_{max} (which corresponds to the most stable scenario). This can be done by considering an analogous relation to (2.15). The diameter calculated in this way should fulfill the following expression:

$$\frac{M_{tip}}{4\pi}\int_0^{2\pi}\int_0^{R_{tip}}\frac{Rz_0}{(x_0^2+z_0^2+R^2-2x_0R\cos\varphi)^{\frac{3}{2}}}dRd\varphi \geq H_0+H_d = H_{max} \tag{2.29}$$

From the equation above, it can be noted that the problem of writing on a dot is being address in a simplified way. The field that actuates on the dot is considered to be the field exerted at its center. In other words, the dot is considered as a punctual particle. Thus, when it is said that the probe makes contact with the dot, still there is a distance under consideration. That is the distance from the center of the *real dot* till its upper surface (z_0).

In the case we are considering the addressed dot is located at the origin of the coordinate system and the tip is right on the top of it, then $x_0 = 0$, and substituting from the above equation we have that

$$\begin{aligned}\frac{M_{tip}}{4\pi}\int_0^{2\pi}\int_0^{R_{tip}}\frac{Rz_0}{(z_0^2+R^2)^{\frac{3}{2}}}dRd\varphi \\ = \frac{M_{tip}}{2}\left(1-\frac{z_0}{\sqrt{z_0^2+R_{tip}^2}}\right) \\ \geq H_0+H_d = H_{max}\end{aligned} \tag{2.30}$$

	b=1/8	b=1/4	b=1/2	b=1	b=2
Co/Pt	868	871	878	892	920
FePt (theoretical)	10414	10416	10420	10429	10477

Table 2.5: *H_{max} in kA/m for two different media (Co/Pt and FePt) as a function of their dot aspect ratio (b)*

and by substitution of $z_0 = r_0 b = gb\Lambda$, $H_0 = \frac{2K}{\mu_0 M_s}$ and $H_d = \tilde{n} b M_s$ we find

$$\frac{M_{tip}}{2}\left(1 - \frac{1}{\sqrt{1+\left(\frac{R_{min}}{gb\Lambda}\right)^2}}\right) \geq \frac{2K}{\mu_0 M_s} + \tilde{n} b M_s = H_{max} \tag{2.31}$$

From the above relation it can be observed that in order to make a probe suitable for writing into a dot, the properties of both materials (dots and probe) should fulfill the following relation

$$\frac{M_{tip}}{2} \geq \frac{2K}{\mu_0 M_s} + \tilde{n} b M_s = H_{max} \tag{2.32}$$

otherwise, it will never be possible to build a probe (not matter how big) that can switch a dot which is already in a situation of maximum stability due to the interactions with its neighbors. The latest finding can be explained because of the fact that, when the surface of the probe becomes too big, the lines of magnetic field out of it become quasi-parallel. In other words, the magnetic flux through the dot remains constant irrespective of the surface-size of the probe.

Table 2.5 shows the values of H_{max} in kA/m for two different media (Co/Pt and FePt) as a function of their dot aspect ratio (b). The value $\frac{M_{tip}}{2}$ for pure Cobalt (hcp) is 710 kA/m and in the case of FePt it is 535 kA/m. As we can see, none of those materials has enough magnetization in order to be used as a writing probe. In principle there are two different approaches to overcome the insufficient magnetization of the probe. The first one consist in locally heating the addressed dot, which will have as an effect the reduction of H_{max} along with its energy barrier. This technique is known as *heat assisted magnetic recording* (HAMR)[23][46]. The other one consists in applying an *auxiliar field* over the whole medium.

2.8.3 Probe dimensions: influence of probe size on neighbouring dots

We have seen that the interaction between dots has effect on the energy barrier and its direct consequence is the modification of the dot's switching field. In the

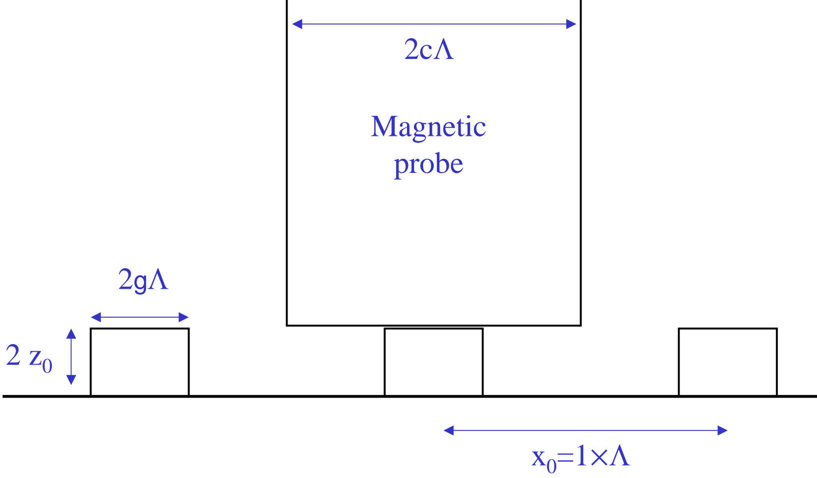

Figure 2.6: *Diagram showing the feature sizes considered in the modelled patterned medium*

same way, besides the addressed dot, the presence of the tip has effect on the energy levels and switching fields of the neighbouring dots. In this section we will quantify the interaction between the first-neighbour dots and the tip when this is in contact with the dot that is being addressed.

By using the left side of expression (2.29) we obtain the value of the z component of the probe's field on the first-neighbour dots. In this case we use a value of $x_0 = a \times \Lambda$ with $a = 1$, and (as before) $z_0 = gb\Lambda$. Figure 2.6 displays a diagram showing the feature sizes that have been mentioned.

$$H_z = \frac{M}{4\pi} gb\Lambda \int_0^{2\pi} \int_0^{R_{tip}} \frac{R}{(\Lambda^2 + (bg\Lambda)^2 + R^2 - 2\Lambda R \cos\varphi)^{\frac{3}{2}}} dR d\varphi \tag{2.33}$$

By applying a change of variable in the form

$$R = \Lambda R' \quad \text{and} \quad dR = \Lambda dR' \tag{2.34}$$

$c = 1/6$	$b = 1/8$	$b = 1/4$	$b = 1/2$	$b = 1$	$b = 2$
$\lvert\frac{H_{(a=0)}}{M_{tip}}\rvert$	0.43798	0.37873	0.27639	0.14645	0.05279
α	91.4	92.9	95.7	101.3	117.2
$\lvert\frac{H_{(a=1)}}{H_{(a=0)}}\rvert$	0.01364	0.01579	0.02172	0.04160	0.12188
$c = 1/2$	$b = 1/8$	$b = 1/4$	$b = 1/2$	$b = 1$	$b = 2$
$\lvert\frac{H_{(a=0)}}{M_{tip}}\rvert$	0.47919	0.45848	0.41780	0.34189	0.22265
α	92.4	94.8	99.5	108.4	123.7
$\lvert\frac{H_{(a=1)}}{H_{(a=0)}}\rvert$	0.09004	0.09435	0.10461	0.13292	0.23270

Table 2.6: *Table showing the value of the ratio between the probe's field at the addressed dot and the probe's magnetization $H_{(a=0)}/M_{tip}$, the angle α (given in degrees) of the probe's field exerted on the first neighbouring dot $H_{(a=1)}$ and the ratio between magnitudes of the probe's field on the addressed dot and on the first-neighbour dot $\frac{H_{(a=1)}}{H_{(a=0)}}$. The values are presented as a function of the dots aspect ratio b (diameter to height) for two values of c, where c is the constant of proportionality between the period Λ and the probe's diameter R_{tip}.*

and by approximating in a similar way than (2.18) into (2.19) we get that

$$H_z \approx \frac{M}{4\pi} gb \int_0^{2\pi} \int_0^c \frac{R'}{(1 + R'^2 - 2R' \cos\varphi)^{\frac{3}{2}}} dR' d\varphi \tag{2.35}$$

where c is the constant of proportionality between the radius of the tip R_{tip} and the period of the dots Λ.

In an analogue way we can obtain the expression for H_x,

$$H_x \approx \frac{M}{4\pi} \int_0^{2\pi} \int_0^c \frac{R'(\cos\varphi - 1)}{(1 + R'^2 - 2R' \cos\varphi)^{\frac{3}{2}}} dR' d\varphi \tag{2.36}$$

In order to prevent side-writing, we would like to compare the probe's field on the first neighbour dot and on the addressed dot. A low value for the ratio of the two fields is desirable. Table 2.6 was constructed with the calculated values from expressions (2.31), (2.35) and (2.36). It shows the value of the ratio between the probe's field at the addressed dot and the probe's magnetization $H_{(a=0)}/M_{tip}$, the angle α (given in degrees) of the probe's field exerted on the first neighbouring dot $H_{(a=1)}$ and the ratio between magnitudes of the probe's field on the addressed dot and on the first-neighbour dot $\frac{H_{(a=1)}}{H_{(a=0)}}$. The values are presented as a function of the dots aspect ratio b (diameter to height) for two values of c, where c is the constant of proportionality between the period Λ and the

probe's diameter R_{tip}. The two values chosen for c are $1/6$, which corresponds to a probe diameter equal to the diameter of the dot, and $1/2$, which corresponds to a probe diameter equal to the period Λ of the patterned array. These two values are considered as extremes in the possible dimensions of the tip. Probes with radius smaller than that of the dot will produce field fluxes through the dot which will be noticeable non-uniform, exerting weaker perpendicular fields at the edges of the dot than at the center. In the other hand, probes with too large diameters will have strong interactions with the neighbouring dots, thus increasing the risk of "side writing". It should be noted from table 2.6 that for a probe with a diameter equal to that of the periodicity Λ the ratio between the field exerted at the addressed dot and its first neighbour is already around 10% and even larger than 20% for higher dot aspect ratios as $b = 2$.

In table 2.6 the angle α is referenced from the original dot magnetization direction, i.e. $\alpha = 0$ correspond to an applied field parallel to the original dot magnetization and $\alpha = 180$ to the antiparallel direction, which is the field angle that will be used for performing a writing operation. It can be seen from the table 2.6 that the angle of the field exerted by the tip at the first-neighbour dot is very close to 90 degrees. Additionally, in the case of $c = 1/6$ the field at the first-neighbour dot is very weak when compared to the field exerted on the addressed dot. In section 2.9 will consider a probe diameter equal to that of the dot, this will allow for neglecting the exerted field at the neighbouring dots, while preserving a reasonable close-to-uniform field flux through the addressed dot. We will also consider in section 2.9 a dot aspect ratio of $b = 1/4$.

2.9 Auxiliary field

We will now consider the case of writing on a dot while using a magnetic probe made of pure cobalt. As mentioned in previous sections, irrespective of the tip size, it will be necessary to assist the writing process since the probe by itself has not enough magnetization to switch the dot. In this section we will consider the application of an auxiliary field as the technique for assisting in the writing process. As mentioned in the latest section, for this estimation we will consider a probe diameter equal to that of the dot and a dot aspect ratio of $1/4$.

While attempting to write on the addressed dot we will consider the most difficult scenario. That is the case in which the addressed dot is in its most stable energy state corresponding to the switching field H_{max} previously discussed and one of the first-neighbouring dots is in its most unstable energy state corresponding to H_{min}. We aim to change the state of magnetization of the addressed dot while not changing the magnetization state of its neighbour. This situation

can be outlined by this expression,

$$H_{tip} + H_b \geq H_{max} > H_{min} > H_b \tag{2.37}$$

where H_b represents the magnitude of the *auxiliary field*. From table 2.4 we take the value of M_s for pure Cobalt as $M_s = 1750$ kA/m and from table 2.6 we have that H_{tip} is (in the case of an aspect ratio $b = 1/4$) $H_{tip} = 0.37873 \times M_s = 537$ kA/m. Also from table 2.5, we obtain for a Co/Pt multilayer $H_{max} = 871$ kA/m. Combining this with the left side of (2.37) we obtain for the minimum value of the auxiliary field

$$537 \text{ kA/m} + H_b \geq 871 \text{ kA/m} \Rightarrow H_b \geq 333 \text{ kA/m} \tag{2.38}$$

From the equation for H_{min} in (2.27) we get that, for Co/Pt, $H_{min} = 857$ kA/m. It can be seen that the condition expressed in the right side of (2.37) is fulfilled. So, we conclude that in the case of Co/Pt the applied auxiliary field should be in agreement with the following constraints,

$$333 \text{ kA/m} < H_b \leq 857 \text{ kA/m} \tag{2.39}$$

2.10 Conclusion

Estimations on different desirable properties of an idealized patterned medium for information storage were presented in this chapter. The medium was proposed to consist of identical SW particles and interaction between neighbouring dots has taken into account.

It has been found that in the context of *one bit in one dot principle*, it is necessary an energy-barrier to thermal-energy ratio ($\Delta E/KT$) of 48.8 in order to achieve a raw BER of 10^{-4} after 5 years. This corresponds to a relaxation time (τ) of 5×10^4 years.

These values are more demanding than those derived from the *stability criterion* stated by Charap [39] for a *one bit per many grains* schema, corresponding to an energy-barrier to thermal-energy ratio of 40.27 and a relaxation time of 10 years. In our stability criterion the minimum acceptable energy barrier value is 2.02×10^{-19} J (1.26 eV).

The magnetic interaction between the dots affects the value of the energy barrier. According to this model, for a given dot-aspect-ratio the highest achievable bit-density is restricted by the magnetization saturation of the dots.

From this model has been estimated that in the case of Co/Pt multilayered dots with an aspect ratio of $b = 1$ the maximum achievable bit density (according

to our stability criterion) lies around 1.6 Tbit/sqi. In the case of FePt $L1_0$ dots with the same aspect ratio the maximum bit density lies around 7 Tbit/sqi.

For lower bit aspect ratios the maximum bit density is lower. In the case of an aspect ratio of $b = 1/10$ (which is close to the features of some of the samples studied in this work) the maximum bit density for Co/Pt dots lies around 0.4 Tbit/sqi and in the case of FePt $L1_0$ it is 1.3 Tbit/sqi.

It is observed that higher aspect ratios are most convenient in realizing high-bit-density magnetic patterned-media.

The medium here discussed exhibits an *energy barrier distribution*. Each dot will possed an energy barrier value depending on the magnetization state of its neighbours due to the dot to dot interactions considered in the model. Since for a given energy barrier value corresponds a switching field value, it follows that there exist a *switching field distribution*. It has been estimated that in the case of dots made of Co/Pt multilayers with an aspect ratio of ($b = 1/4$) the switching fields range from 857 to 871 kA/m.

It can be expected that larger switching field distributions will be observed in actual magnetic pattern-media. Eventual inhomogeneities or defects within the dots are not considered in our model and they would strongly disperse the switching field values.

In order to change the magnetization state of a dot it was proposed to place a magnetic probe in contact with the addressed dot. It was found that from all the materials displayed in table 2.4 none has enough magnetization to switch a dot. In order to assist the insufficient magnetization, it has been proposed the use of an auxiliary field. In the case of a probe made of pure Cobalt with a diameter equal to that of the dots it has been estimated that an auxiliary field in between 333 and 857 kA/m is required.

It is predictable that in actual patterned media, the auxiliary field values will be more restricted due to the larger switching field distributions that are expected.

Chapter 3

Laser interference lithography for film patterning

Laser Interference Lithography is an alternative mask-less lithographic technique. In this technique a photosensitive resist is exposed to an interference pattern produced by two coherent laser beams. This lithographic technique has the capability of generating patterned structures over large areas [47, 48, 49, 50] and in short time. [1] The method has been used as a tool for fabricating submicron gratings for application in integrated optics for many years [51, 52]. In recent years Interference Lithography has attracted great attention for a wide variety of applications [23], amongst others: field emission displays [53], antireflection-structures and polarization elements [54], photonic crystals [55], microfiltration [56], mask masking for nanoimprint [57] and X-ray lithography [58] and patterned magnetic media [59, 60, 61, 62]. Its capability for patterning large areas is clearly demonstrated by the fabrication of 50×50 cm^2 areas of submicron dots [63].

3.1 LIL for magnetic patterned media

In Chapter 2 a patterned magnetic medium was suggested, composed of arrays of single domain elements with uniaxial perpendicular anisotropy and arranged in a square lattice. It is obvious that in order to fabricate such a structured medium a patterning technique is required with which a large and regularly patterned area can be obtained. Laser Interference Lithography is suitable for this application.

In order to study the feasibility of magnetic data storage in discrete nanoparticles, as well as to design the optimal nanomagnet for application in storage,

[1] Typical exposure times are less than 1 minute.

different groups have found interference lithography to be the lithography of choice [59, 61, 62].

Interference lithography offers advantages over scanning electron-beam lithography due to its ability to define grid patterns over large areas in a single, fast, maskless exposure. In addition, since interference lithography defines periodic patterns with well-controlled periodicity, it provides an absolute reference that may facilitate read/write head position tracking [49].

At the moment, at the MESA+ Institute two other research projects explore the possibilites of LIL. One of them in the field of photonic crystals [64, 65, 66] and the other one in the field of microsieves and nanochanels fabrication [67, 68].

3.2 Principle of interference

Let us assume two planar waves, denoted by $\vec{k}_1$ and $\vec{k}_2$ which are incident to a surface and under an angle Θ with respect to the $\hat{z}$ direction (perpendicular to the plane).

$$\vec{k}_1 = k(\hat{x}\sin\Theta, \hat{z}\cos\Theta) \quad \text{and} \quad \vec{k}_2 = k(-\hat{x}\sin\Theta, \hat{z}\cos\Theta) \tag{3.1}$$

From (3.1) we have that $|\vec{k}_1| = |\vec{k}_2| = k$, where k is the wave number which is related to the wavelength of the radiation source according to $k = 2\pi/\lambda$. In order to find the intensity of the interference pattern, the two plane waves are added at the position $\vec{r} = x\hat{x} + z\hat{z}$. Thus, the amplitude of the resulting wave can be expressed as follows:

$$I(\vec{r}) \propto \left| \exp(i\vec{k}_1 \cdot \vec{r}) + \exp(i\vec{k}_2 \cdot \vec{r}) \right|^2 = 4\cos^2\left(\frac{1}{2}(\vec{k}_1 - \vec{k}_2)\cdot\vec{r}\right) \tag{3.2}$$

After calculating the inner product we obtain the following expression for the intensity pattern along the substrate in the $\hat{x}$ direction:

$$I(\hat{x}) \propto \cos^2(kx\sin\Theta) \tag{3.3}$$

The minimal resolvable feature size Δx, which corresponds to the distance between intensity maximum and an adjacent minimum, can be found with help of the following relation:

$$k\Delta x \sin\Theta = \frac{\pi}{2} \tag{3.4}$$

From the former equation, the minimal resolvable feature can be expressed as

$$\Delta x = \frac{\pi}{2k\sin\Theta} = \frac{\pi}{2\left(\frac{2\pi}{\lambda}\sin\Theta\right)} = \frac{\lambda}{4\sin\Theta} \tag{3.5}$$

Finally, the period Λ of the created pattern (distance between two adjacent maxima) is two times Δx:

$$\Lambda = \frac{\lambda}{2\sin\Theta} \tag{3.6}$$

As seen from the last expression, the minimum achievable periodicity is ideally that corresponding to half the wavelength of the radiation source,

$$\Lambda_{min} = \frac{\lambda}{2} \tag{3.7}$$

From the last two expressions it is concluded that the smaller the wavelength used, the smaller the produced patterns will be.

3.3 Types of laser interferometers

Different kinds of experimental arrays have been proposed in order to produce structures by means of Interference Lithography. In this section we give a brief overview on them.

There are two main kinds of Interference Lithography arrays in use. One of them makes use of reflective optics elements while the other one uses diffractive optics elements.

3.3.1 The dual beam interferometer

The dual beam interferometer makes use of reflective optics as a means to produce interference patterns. A beam of light is directed onto a beam splitter. There the beam is divided into two branches of almost the same intensity. Each branch is directed to a mirror. The mirrors are located in such a position and angle that they reflect the beams in a way that they intersect each other at the surface of the sample to be patterned. Before each beam of light reaches the substrate they go through a spatial filter and beam expansion assembly consisting of a lens (or lenses) and a pinhole. The spatial filters are used to eliminate noise from the beam which would otherwise be printed as distortion in the grating. A

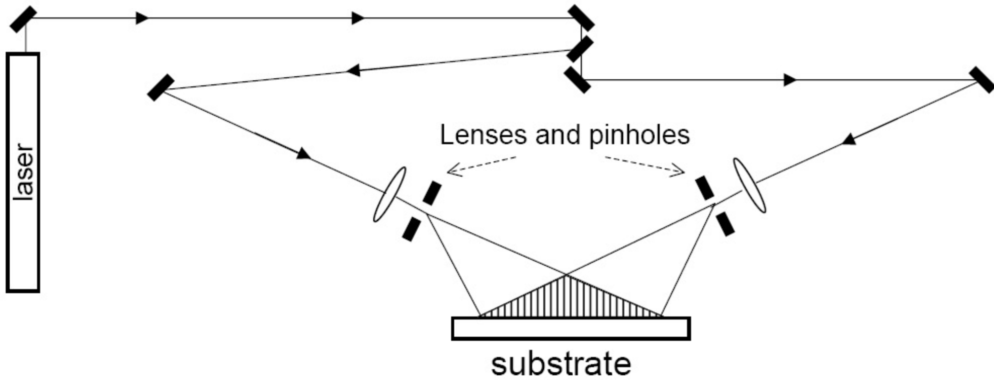

Figure 3.1: *Diagram showing the basic configuration of a dual beam interferometer. A laser beam is directed onto a beam splitter. The resulting beam branches will be redirected by mirrors onto a system compound of lens(es) and pinhole(s), which serve as spatial filters. The filtered pair of beams intersect each other at the sample surface where the interference occurs.*

schematic diagram of the dual beam interferometer setup array is displayed in Figure 3.1.

The dual beam interferometer consists of a number of moving parts: Each one of the mirrors should be adjusted at an specific angle in order to produce an interference pattern with the desired periodicity. The beam splitter should be also carefully aligned, so the two resulting beams of light could reach properly each one of the mirrors. Finally, the sample holder must be displaced every time the angle of the mirrors is readjusted in order to place the sample surface at the point of incidence of the two interfering beams.

All those moving parts are susceptible to vibration during the time of exposure. Relative displacements of the optical elements of the setup will ruin the exposure. It should be noted that displacements produced by vibrations should be small compared to the wavelength of the light-source employed. A relative motion of only half the periodicity of the produced interference is enough to totally erase any pattern on the photoresist.

3.3.2 The Lloyd's Mirror Interferometer

The Lloyd's Mirror setup is another interferometer based on reflective optic elements. It consists of a mirror placed perpendicular to the sample holder. An expanded beam illuminates both the mirror and the sample. Part of the light is reflected on the mirror and interferes with the portion of the beam that is directly

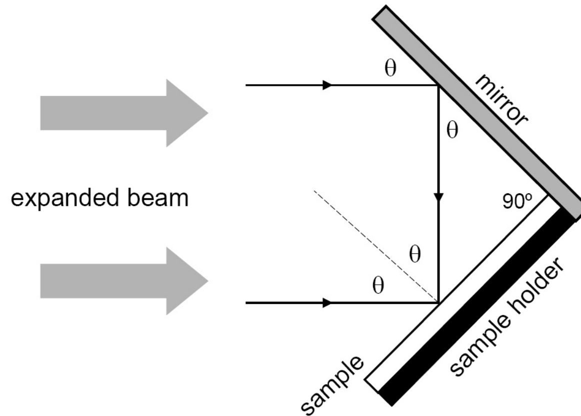

Figure 3.2: *Diagram of a Lloyd's mirror. It consists of a mirror placed perpendicular to the sample holder. An expanded beam illuminates both the mirror and the sample. Part of the light is reflected on the mirror and interferes with the portion of the beam that is directly illuminating the sample.*

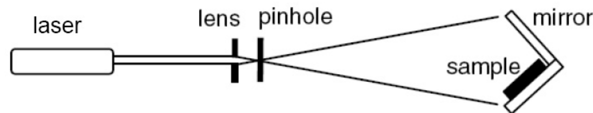

Figure 3.3: *Simplified diagram of the Lloyd's mirror interferometer setup. A laser beam is expanded and spatially filtered by an array of a lens and a pinhole. The broad beam is then directed onto a mirror-sample array.*

illuminating the sample. Figure 3.2 shows a diagram of the Lloyd's mirror.

The periodicity of the produced pattern can be changed by rotating the whole array (mirror and sample holder). In the case of the Loyd's mirror interferometer there is only one laser beam which is expanded and spatially filtered by an array of lens(es) and a pinhole. The broad beam is then directed onto the mirror-sample array. Figure 3.3 shows simplified a diagram of the Lloyd's interferometer setup.

3.3.3 Advantages of the Lloyd's Mirror array

Because the number of moving parts the dual beam interferometer setup is sensitive to vibrations which can disturb the interference pattern. On the other hand, the Lloyd's mirror setup has less moving parts and therefore less risk of vibrating during the exposure time.

The Lloyd's mirror interferometer only requires a simple rotation of the sample-holder-and-mirror-array in order to change the periodicity of the produced interference pattern. In the case of the dual beam interferometer it is necessary to move and align more elements.

The spatial filters of the dual beam interferometer are located after the mirrors. In the case of the Lloyd's setup the spatial filter is located before the mirror. Thus any dust particle or imperfection on the mirror surface will produce scattering or variation on the optical path of the incoming light which may be noticed as irregularities in the produced interference pattern. In that sense, the dual beam interferometer allows for higher quality patterns.

Additionally, since the reflectivity of the mirror is not 100%, the intensity of the the two beams interacting in the Lloyd's interferometer is never equal. This will deteriorate the contrast of the resulting patterns.

In both of the setups dots can simply be fabricated by a second exposure after rotating the substrate over 90°. Different kind of patterns can be obtain by using different rotation angles between the two exposures. A few examples are displayed in figure 3.4: The first column shows different patterns done by LIL exposure on positive tone photoresist. In case of using negative (instead of positive) photo-resist it is possible to fabricate arrays of holes (second column of figure 3.4. The third column shows the calculated dose distribution over the photoresist after a double LIL exposure. The equation used to produce the graphs in the third column of the figure is displayed below:

$$D = \sin^2\left(\pi * \frac{x}{\Lambda}\right) + \sin^2\left(\pi * \frac{x\cos\alpha + y\sin\alpha}{\Lambda}\right). \tag{3.8}$$

In the former equation (3.8), α is the angle of rotation of the sample in between the two exposures and Λ is the periodicity of the resulting pattern. The value of Λ is obtained from expression (3.6)

The patterned area is determined by the diameter of the two laser beams in the case of the dual beam interferometer. In the case of the Lloyd's mirror interferometer, the size of the mirror is also an important factor. In both setups laser instabilities or beam intensity variations will cause problems while using two different exposures in order to obtain a dot pattern. Those problems will be noticed as elliptic photoresist dots (instead of rounded dots in the case of a 90°rotation) and distortions over the pattern.

3.3.4 Interference Lithography arrays by means of diffractive optic elements

Next to the dual-beam and Lloyd's mirror setups, one could only just use a single diffraction grating. Depending on the grating design setups of this kind can

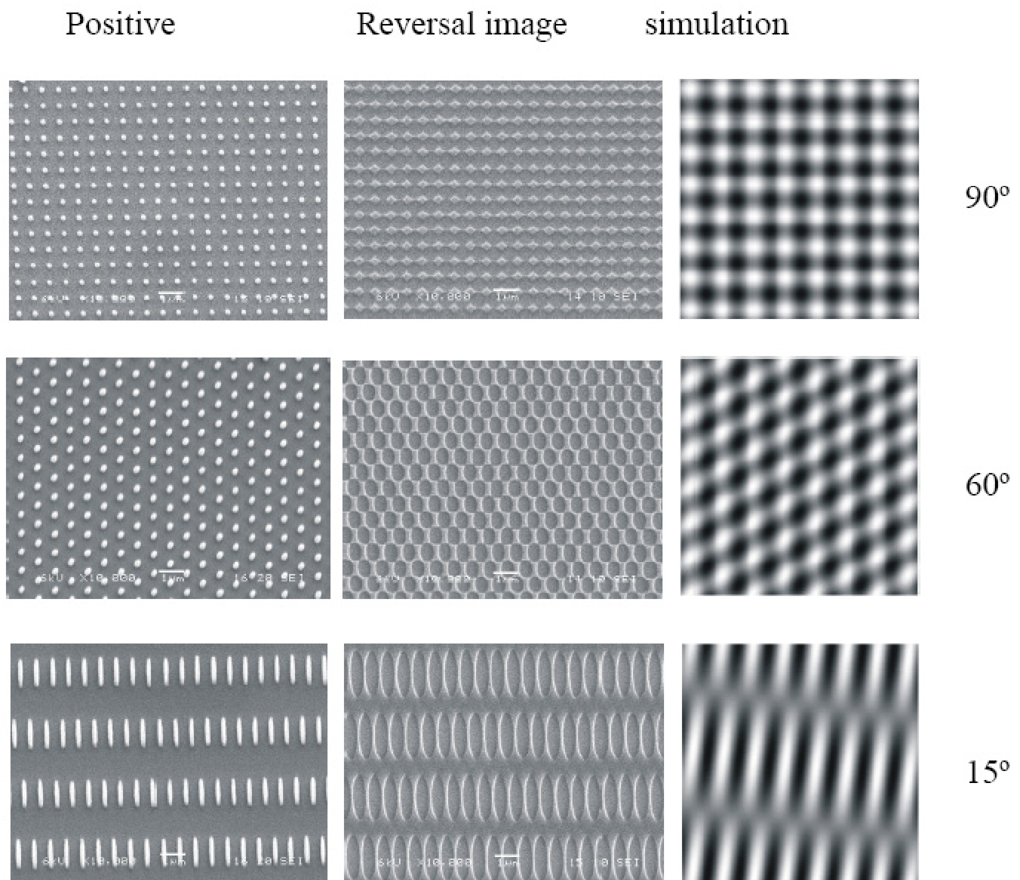

Figure 3.4: *SEM images of different patterns obtained by changing the rotation angle of the substrate between two LIL exposures. The patterns here displayed were obtained by using positive PR (diluted Olin 907/12) for producing dots (first column) and reversal image PR (TI 09xr) for producing holes (second column). The third column displays the calculated intensity patterns according to the different rotation angles. All the patterns were produced with the Lloyd's mirror interference setup available at the MESA+ institute. In every case the sample holder was fixed at an angle of* 12.81 *degrees with respect to the incident beam, which in the case of a beam wavelength of 266 nm corresponds to a periodicity of 600 nm.*

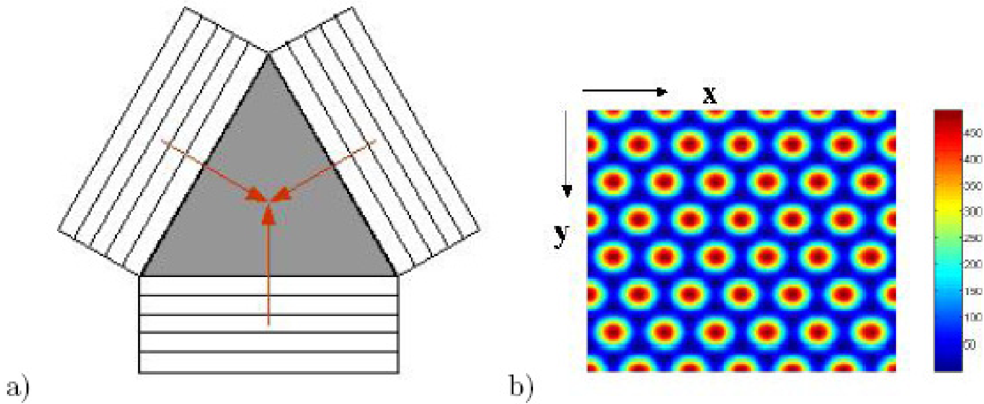

Figure 3.5: Schematic view of a diffraction grating a) that will generate from a single light beam 3 beams that will interfere to generate the intensity distribution calculated in b) at the wafer location.

generate from a single beam of light two or more diffracted beams which will interfere to generate a specific pattern [55, 69]. An example of a 3 beam diffraction grating and its corresponding calculated intensity pattern are displayed in figure 3.5 [70].

Setups of this kind require no mirrors but only a single diffraction grating. This leads to almost circular dots or holes and a higher contrast pattern in photoresist, as shown by the calculation in figure 3.5. Therefore problems with ellipticity of holes and inhomogeneity of pattern, caused by double exposure in dual-beam or Lloyd's mirror approaches, can be overcome. Further advantages are a single exposure step and less critical exposure dose. However some flexibility will be lost since the pattern period is determined by the grating and cannot be adjusted by the angle of incidence as is the case using the *dual beam* or the *Lloyd's mirror* approaches. Additionally, the gratings have to be carefully aligned, which makes this method difficult to use.

Achromatic interference lithography

One possible option is to use *achromatic interference lithography*. In this array a phase grating is used to obtain two first order diffraction beams from an incident short wavelength lightsource, which does *not* have to be coherent. The diverging beams are reflected back by an additional set of gratings and form a standing wave with half the periodicity of the gratings used. The phase gratings can be made by conventional LIL, which doubles the achievable periodicity. Figure 3.6 shows a diagram of the achromatic interference lithography setup. Achromatic

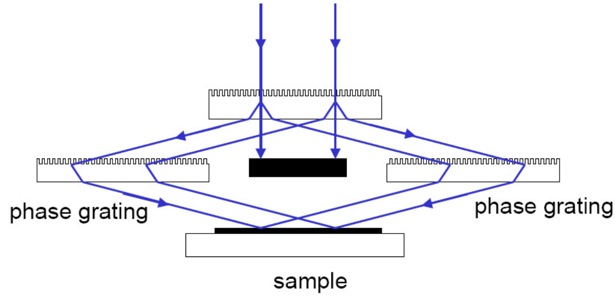

Figure 3.6: *Diagram of the achormatic inteference lithography setup. One of the advantages of this array is that the light source does not have to be coherent. The periodicity of the resulting pattern is half the periodicity of the phase gratings.*

Laser Type	Wavelength (nm)
Argon fluoride (DUV)	193
Krypton fluoride (DUV)	248
Nitrogen (UV)	337
Argon (UV)	351
Argon (blue)	488
Argon (green)	514
Helium neon (green)	543
Helium neon (red)	633
Rhodamine 6G dye (tunable)	570-650
Ruby ($CrAlO_3$) (red)	694
Nd:YAG (NIR)	1064
Carbon dioxide (FIR)	10600

Table 3.1: *Typical commercially available lasers and their emission wavelengths. The LIL setup at the MESA+ institute is equipped with a Nd:YAG laser with a basic wavelength of 1064 nm. This wavelength is frequency doubled to 532 nm in an intracavity and by using an external frequency doubler this wavelength is again halved to $\lambda = 266$ nm.*

interference lithography using ArF excimer lasers at 193nm has the capability of patterning resist structures with periods of 100 nm [71] [72].

3.4 Particular details on the used laser interference setup

In order to produce the smallest possible interference patterns, a compromise between wavelength and stability of the laser source has to be made. A list dis-

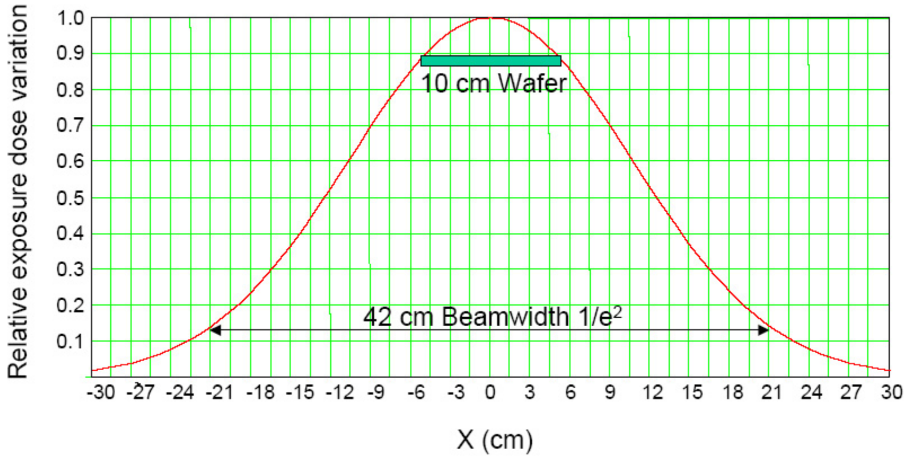

Figure 3.7: *Calculated exposure dose variation for a gaussian beam with a width of 42 cm. This beamwidth warranties that a wafer of 10 cm in diameter will be exposed with a maximum expose dose variation of 10%.*

playing different kinds of commercially available laser is displayed in table 3.1 The shortest wavelength is obtained with an ArF eximer laser. This is however a pulsed laser, which suffers from poor coherency length. For our LIL setup we chose a highly stable continuous wave (CW) Nd:YAG laser with a basic wavelength of 1064 nm. This wavelength is frequency-doubled to 532 nm in an intracavity. By using an external frequency doubler this wavelength is again halved to λ=266 nm with a small bandwidth (1 Mhz) and a maximal power of 200 mW. This UV laser beam is optically filtered with a lens with a focal distance of 11 mm and a pinhole of 5 μm in diameter to achieve a clean near-Gaussian beam.

Even when the beam is perfectly filtered, it should be wide enough to get an illumination with sufficient spacial homogeneity. For that reason, the diverging beam travels 3 m over an optical table to a Lloyd's Mirror Interferometer mounted on a rotation table. By doing this it is possible to achieve a beamwidth of 42 cm (1/e) at the sampleholder position. This warranties that a 10 cm wafer could be exposed with a maximum exposure dose variation of 10%. In figure 3.7 the calculated variation in exposure dose of a gaussian beam with a width of 42 cm is shown. Additionally, the beam divergence along the 3 m path allows to get a quasi-planar wavefront which is needed in order to generate regular interference patterns.

As has been mentioned, this produced interference will give a line pattern with a periodicity given by $\Lambda = \frac{\lambda}{2\sin\Theta}$. By changing the angle Θ, the periodicity Λ can be easily adjusted from almost 1 μm down to 150 nm as shown in figure 3.8.

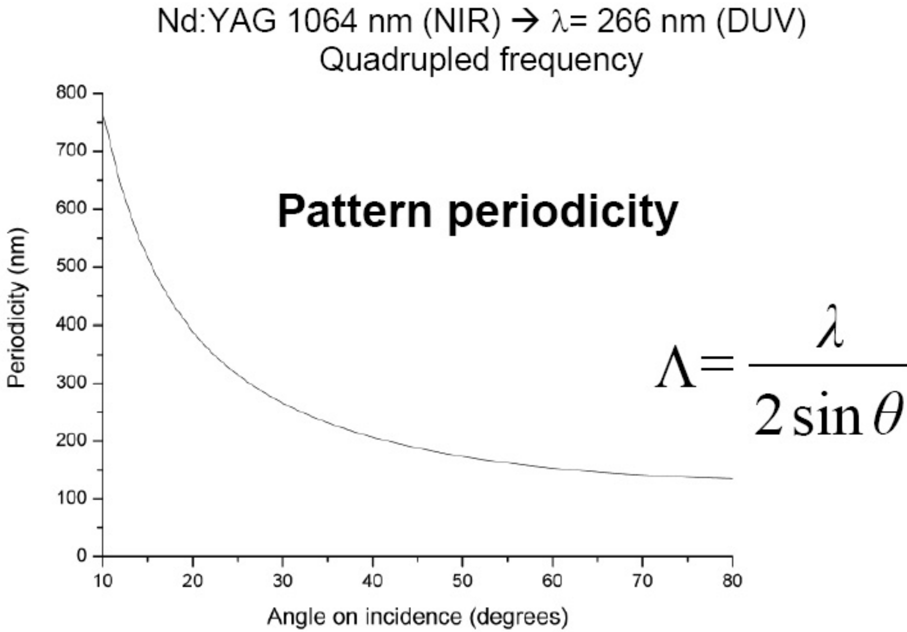

Figure 3.8: *Line pattern periodicity (nm) as a function of the angle of incidence (given in degrees) for a fixed wavelength $\lambda = 266$ nm. For all practical purposes periodicities ranging from almost 1 μm down to 150 nm can be achieved in the laser interference setup at the MESA+ Institute.*

To prevent vibrations, which could disturb the interference pattern, the complete setup is built on an actively damped optical table of 3 $\times$ 3.6 m. The Lloyd's Mirror Interferometer is placed in a closed cabinet to avoid air streams which could affect the stability of the interference pattern. Additionally, the part of the floor in the MESA+ cleanroom where the setup is situated, is mechanically isolated from the foundations of the rest of the building in order to reduce the influence of vibrations form the surroundings (e.g. other cleanroom equipments).

With this setup highly regular patterns can be produced over areas of about 2 cm $\times$ 2 cm. .

3.5 Summary

The laser interference lithography method which serves to expose patterns on photoresist was presented. Different kinds of experimental arrays were described and some of their advantages and limitations were mentioned. The laser interference setup at the MESA+ Institute facilities was described and compared with the dual-beam setup array.

At present, the minimum period of the interference pattern at the MESA+ LIL setup is 133 nm, which corresponds to half the wavelength of the laser source that is used. For further decrease of the periodicity it should be necessary to use a laser source with a shorter wavelength. However, lasers with shorter wavelengths often lack of coherence and/or stability. Both characteristics (coherence and stability) are indispensable in a laser source which would be used in a Lloyd's mirror setup. Nevertheless, achromatic interference lithography can use laser sources that not necesarily should be coherent.

Chapter 4

Preparation and characterization of CoNi/Pt and Co/Pt multilayers

In this chapter, the deposition process of continuous magnetic multilayered CoNi / Pt and Co / Pt films is presented. The substrate preparation is explained and how it influences the magnetic properties of the deposited films. The effect of the number of deposited bilayers on the magnetic properties is also discussed. The films have been characterized by Magnetic Force Microscopy, Vibrating Sample Magnetometry, Anomalous Hall Effect and Magneto-Optical Kerr effect. With these techniques it was found that smoother substrates favour sharper transitions in the switching of magnetization.

4.1 Introduction

Before we can prepare an array of magnetic dots, it is necessary to prepare a substrate which will support the magnetic material. In our case we used two kinds of substrates, silicon wafers without any thermal treatment and silicon wafers with a layer of silicon oxide grown by thermal oxidation. It has been found that the way of preparing the substrate has an influence on its roughness (section 4.3) and on the magnetic properties of the magnetic film deposited on it (section 4.4).

By magnetron sputtering two kinds of multilayered films were deposited on the substrates, $Co_{50}Ni_{50}$/Pt and Co/Pt. Those films show perpendicular magnetic anisotropy due to the contribution of the interfaces [73]. Continuous CoNi/Pt and Co/Pt multilayers have been formerly studied in the Systems and Materials for Information storage group [45] [62] [41]. In order to take advantage of the already earned expertise, it was decided to use those materials as basis for our research on patterned magnetic films.

The samples were magnetically characterized by Vibrating Sample Magnetometry (VSM), Magnetic Force Microscopy (MFM), Magneto-Optical Kerr effect (MOKE) measurements and Anomalous Hall Effect (AHE). A brief description of those techniques is offered in section 4.2. A discussion on the influence of the substrate and number of deposited bilayers on the resulting magnetic properties is given in section 4.4.

4.2 Magnetic characterization techniques

Different techniques for magnetic characterization were used to analyse the sputtered films. This section gives some descriptions and remarks on these methods.

4.2.1 Vibrating sample magnetometry

Vibrating Sample Magnetometry (VSM) is one of the most important methods of magnetic characterization. In this technique the sample is positioned in between the poles of an electromagnet, which is used to apply different external fields. Around the sample there is a group of small coils which will serve as sensors. The sample is mounted on a servomechanism which will make the sample to vibrate. The vibration of the magnetic sample will produce changes in the magnetic flux through the sensing coils. This will induce a voltage proportional to magnetic moment of the analysed sample. Details of this technique can be found in [74].

4.2.2 Magnetic force microscopy

Magnetic force microscopy (MFM) is a scanning probe technique. In this technique a thin magnetized tip is mounted on a flexible plate named cantilever. Then the array of cantilever and tip is brought to a very close distance from the sample surface. The interactions between the sample's magnetic field and the magnetic tip will become noticed as attractive or repulsive forces on the tip. The exerted forces will produce deflections on the cantilever which is what is actually measured. MFM is a useful technique to determine domain structure. The resolution of MFM reaches below 50 nm and allows investigation of nanomagnets [75]. However, MFM has the drawback that the information gathered by this technique is qualitative. Quantitative interpretations of the read signals are not reliable because the magnetization state of the MFM tip depends on too many parameters including shape irregularities and previous magnetic interactions (history of the tip).

4.2.3 Magneto-optical Kerr effect

The change in polarization of light transmitted through magnetic magnetic materials was first reported by Michael Faraday in 1845 and is known as *Faraday effect*. The analogous effect on reflected light was discovered by Rev. John Kerr in 1876 and became known as *Kerr effect*.

When plane polarized light reaches the surface of a magnetic material, the reflected light will undergo a rotation on its plane of polarization with respect to the incident beam of light, named as *Kerr rotation*. This happens because the refraction index for right-handed circularly polarized light and the refraction index for left-handed circularly polarized light are not equal if the material is magnetized. It should be noted that a beam of plane polarized light can be expressed as the combination of two opposed circularly polarized beams. When the magnetization of the sample is changed, e.g. by means of an applied external field, the the Kerr rotation will also change. Since the Kerr rotation is proportional to the magnetization of the sample, it is possible to construct hysteresis loops by measuring the Kerr rotation as a function of an applied external magnetic field.

4.2.4 Anomalous Hall effect

If there is an electric current flowing through a thin film and a magnetic field is applied , then it will possible to measure a potential difference due to the presence of the magnetic field. The ratio of the potential difference to the current flowing is defined as the *Hall resistance* and is a characteristic of the material. This phenomenon was discovered in 1879 by Edwin Hall and is named *Hall effect*, also know as *normal Hall effect*. In general the measured Hall voltage (V_H) consists of the contributions of three effects: the normal (V_{NHE}, the anomalous (V_{AHE}) and the planar (V_{PHE}). Thus, in a general form, the Hall voltage can be expressed as

$$V_H = V_{NHE} + V_{AHE} + V_{PHE} \tag{4.1}$$

When the magnetic field is applied perpendicular to the current the planar Hall effect becomes zero. If the film plane is assumed as the xy plane and the current is assumed to be applied along x-axis (I_x), the Hall voltage of the film (V_y) can be written as

$$V_y(H) = \Big(R_{NHE}H_z + R_{AHE}\frac{M_z}{\mu_0}\Big)\frac{I_x}{t}, \tag{4.2}$$

where R_{NHE} and R_{AHE} are the Hall resistances related to the NHE and the AHE, H_z and M_z are the perpendicular components of the external field and the

magnetization, respectively, μ_0 is the permeability and t is film thickness. If the Hall voltage is plotted as a function of the applied field, the contribution of the NHE can be easily subtracted from the AHE curve as a linear function of the applied field. Therefore, relevant parameters such as coercivity(H_c) and squareness ratio ($S = M_r/M_s$) can be obtained [76]. This technique has been used in the characterization of polycrystalline Co-Cr [77]. AHE has also been used for the magnetic characterization of a single isolated $L1_0$FePt dot with a diameter of 60nm [78]. As part of this thesis we have used the AHE technique as a characterization method for Co/Pt multilayers as well as for arrays of nanodots prepared from those multilayers by laser interference lithography (LIL). Further details regarding the AHE characterization technique can be found in [77].

4.3 Substrate preparation

The very first step in the fabrication process of a sample is the cleaning of the wafer. It includes the removal of possible organic and inorganic contamination.

The cleaning of the wafers consisted in immersing them in fuming nitric acid (concentration of 100%) to remove organic material and an immersion in boiling nitric acid (concentration of 70%) to remove inorganic contaminants such as metallic particles. After this cleaning process the wafers will still posses a thin layer of native silicon oxide which was removed with a bath of hydrofluoric acid (HF) with a concentration of 1% by one minute.

For most of the samples a silicon oxide layer was grown by thermal oxidation. Two oxidizing methods were used: dry thermal oxidation and wet thermal oxidation. The first one consists of placing the wafer into an oven with a flux of oxygen and bringing the substrate to an elevated temperature. In the second method, a mixture of air and water vapour is injected into the oven where the oxidation takes place.

Different kinds of substrates were thus used: silicon wafers with its native oxide removed [1], and thermal oxidized silicon wafers by using the dry and the wet methods. The substrates roughnesses were measured by AFM, resulting in a value of 0.4 to 0.5 nm for the thermally oxidized wafers while the silicon substrates had a roughness of 0.2 nm [2]. The former results are in agreement with measurements reported elsewhere [79, 80]. In our measurements, roughness

[1]Native oxide was removed from the silicon wafers by using a bath of HF with a concetration of 1% during one minute. After the removal of the native oxide layer the wafers were loaded into a vacuum chamber where the sputtering of the magnetic films took place. The time span since the HF bath till the samples were loaded did not exceed 5 minutes. Although during the meanwhile a new oxide layer will grow the time is not enough for achieving a self limited process (SMI internal communications).

[2]Roughness on silicon wafers were measured about 1 hour after the HF cleaning

substrate	oxidation method	temperature (°C)	process time	silicon oxide thickness (nm)	roughness (nm)
Si	—	—	—	—	0.205
SiO_x	wet	900	30 min	400	0.375
SiO_x	wet	1150	30 min	590	0.440
SiO_x	dry	950	$1\frac{1}{2}$ hr	40	0.464
SiO_x	dry	1100	$4\frac{1}{2}$ hr	300	0.517

Table 4.1: *Roughness of different substrates measured as the mean square root of the height variations over an area of 1μm^2. The first row corresponds to those substrates which did not receive any thermal treatment, however a very thin native oxide layer exists on top of them. The method of oxidation (dry oxidation or wet oxidation) is indicated along with the process temperature and process time for the rest of the rows in the table.*

was defined as the mean square root of the height variations over an area of 1 μm^2.

In table 4.1 a summary of the roughness measurements on the different kinds of substrates is displayed, along with the silicon oxide thickness grown and the corresponding oxidation method. It should be noted that the first row of table 4.1 corresponds to those substrates which did not receive any thermal treatment. However, even when those substrates got their original native oxide coat strippe dby using a bath of HF, the oxide spontaneously regrew as soon as those wafers were again in contact with the air.

4.4 Sputtering deposition of CoNi/Pt and Co/Pt continuous multilayers

After the substrate preparation, the next step in the sample fabrication is the deposition of a magnetic film by magnetron sputtering.

The sputtering machine used for growing the films has two vacuum chambers: The main chamber, where film deposition takes place, with a base pressure smaller than 5×10^{-8} mbar; and a loadlock chamber, which serves as an intermediate pressure step just before bringing the substrate into the main chamber.

Inside the main chamber there are two circular planar magnetrons, each one with a diameter of 2 inches. Due to the system specific configuration, the plasma is confined within approximately 1 inch of distance from the targets [81]. The target-to-substrate distance is 100 mm.

The sputtering gas is argon and the deposition pressure can be varied from 1 to 36 μbar. A more extensive description of the system can be found elsewhere

[82].

Previous work within the SMI group has been done in order to optimize the magnetic properties of multilayered $Co_{50}Ni_{50}/Pt$ films [41] and we decided to use those same parameters in this work. Thus, our $Co_{50}Ni_{50}$/Pt films, consisted of 26 bilayers deposited on a seed layer of Platinum (Pt(6Å) / [$Co_{50}Ni_{50}$(6Å) / Pt(6Å)] x 26). All of them sputtered at an argon plasma pressure of 12 μbar. Previous experiments carried out in the same deposition system have shown that this sputtering argon pressure favours the formation of smooth $Co_{50}Ni_{50}$/Pt interfaces, thus providing a good perpendicular magnetic anisotropy [45]. The $Co_{50}Ni_{50}$/Pt films were deposited using a DC power of 30 W, with a voltage of 400 V for the Platinum, which corresponds (at the argon pressure of 12 μbar) to a deposition rate of 1.6 Å/s. In the case of the $Co_{50}Ni_{50}$ alloy, an AC power of 40 W (13.52 MHz) was used, resulting in a deposition rate of 0.5 Å/s.

In the case of the Co/Pt films, the samples consisted of two different sets of samples. A first set with 1, 3, 5 and 10 bilayers with a 10 Å Pt seed layer, deposited on a silicon oxide substrate. And a second set of 5 bilayers with a 10 Å seed layer deposited on three different kinds of substrates. All the samples were deposited at the minimum stable argon pressure of the system, corresponding to 1μbar, in order to achieve the smoothest layer's interfaces. At this pressure, a DC power of 30 W resulted in a Platinum deposition rate of 1.3 Å/s. The Cobalt deposition rate was 0.5 Å/s with an AC power of 30 W (AC frequency was the same os that for the sputtering of the CoNi alloy).

4.5 Magnetic characterization of CoNi/Pt multilayers

In figure 4.1 hysteresis loops of five $Pt(6\AA)/[Co_{50}Ni_{50}(6\AA)/Pt(6\AA)] \times 26$ films deposited under similar sputtering conditions but on different substrates measured by VSM in the direction perpendicular to the film surface are displayed. It is observed from the graphs that from saturation the magnetic moment of the films suddenly drops at an applied field of around 16 kA/m, and then slowly increases to saturation in the opposite direction. As discussed elsewhere this reversal behaviour can be explained by two processes[62]: First at the nucleation point stripe-domains are formed and the sample turns into a demagnetized state. This means that the energy barriers for domain wall displacements are very small. Second, when further increasing the applied field, the stripe domains are narrowed and completely vanish at saturation. Moreover, the origin of the initial nucleation is the presence of small, vestigial domains which become unstable at some certain applied field. Also Barnes et al. (1994) [83] explain this reversal behaviour for a similar multilayerd system (Co/Pd).

From the curves (figure 4.1) it is also observed that the nucleation point is less well defined for those films deposited on rougher substrates. In the same figure

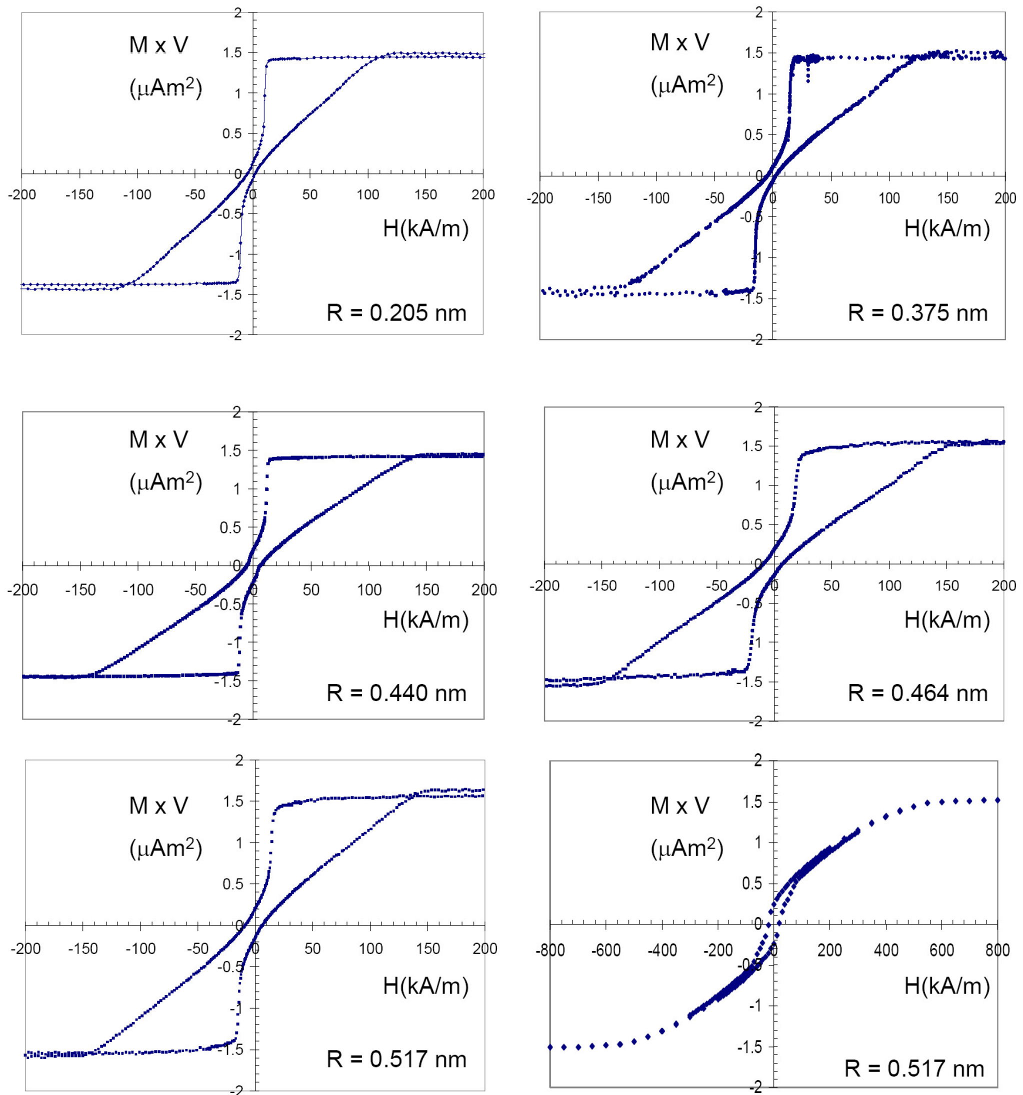

Figure 4.1: *Perpendicular hysteresis loops of five CoNi/Pt films deposited under the same argon pressure conditions but on different substrates. The roughness (R) of each substrate is displayed on the bottom right corner of each graph. All the samples correspond to the following array Pt(6Å)/[$Co_{50}Ni_{50}$(6Å)/Pt(6Å)]x26. At the bottom right corner it is also displayed the in-plane VSM loop the film deposited on the substrate with a roughness of 0.517 nm. The in-plane VSM graph presented here is typical of these kind of films.*

substrate	oxidation method	Temperature °C	roughness (nm)	H_c (kA/m) VSM
Si	—		0.205	3.64
SiO_x	wet	900	0.375	4.55
SiO_x	wet	1150	0.440	6.55
SiO_x	dry	950	0.464	8.94
SiO_x	dry	1100	0.517	8.89

Table 4.2: *Selected set of $Co_{50}Ni_{50}$/Pt multilayers samples. All the samples here listed consisted of a seed layer of Platinum (6Å) and 26 bilayers ($Co_{50}Ni_{50}$(6Å/Pt(6Å)). The columns display from left to right: type of substrate, oxidation method (if that is the case), temperature at which the oxidation process was performed, substrate roughness and coercivity as measured by Vibrating Sample Magnetometer (VSM) . The first row in the table corresponds to those substrates which did not receive any thermal treatment.*

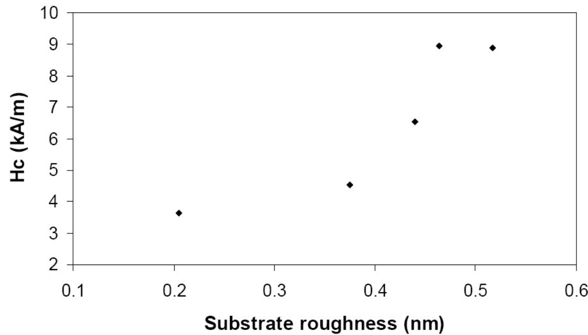

Figure 4.2: *Coercivity (H_c) as measured by VSM as function of the substrate roughness. The samples analysed correspond to those on table 4.2*

(4.1) it is also displayed the in-plane VSM loop of one of the films (bottom right corner). From comparing the perpendicular and in-plane loops it is possible to conclude the presence of perpendicular anisotropy. This is the case for all the other films discussed in this section. Table 4.2 displays the values for the coercivity of those samples along with the kind of substrate and its roughness. It can be noted that the substrate roughness seems to have influence on the coercivity of the films. The smoother the substrate, the lower the coercivity. Such behaviour is depicted in figure 4.2. The reason could be that rougher substrates favour the formation of more defects in the deposited layers and interlayer-interfaces, thus domain propagation becomes more difficult and requires of higher coercive

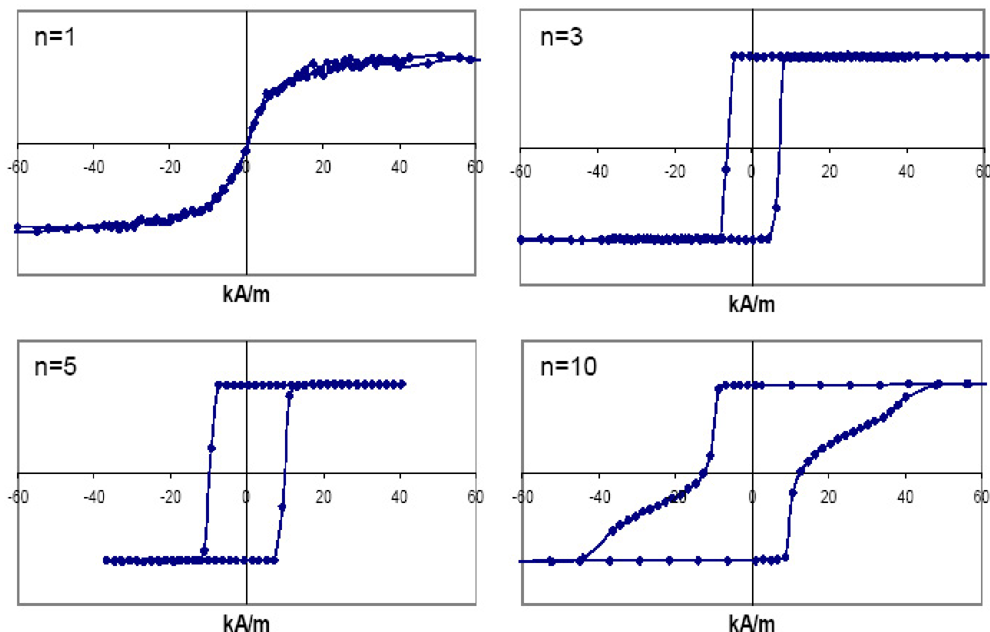

Figure 4.3: *Hysteresis loops of multilayered Co/Pt films taken by means of Anomalous Hall Effect measurement. In the figure loops corresponding to four different samples are displayed, all of them deposited under the same sputtering conditions but consisting of a different number of bilayers (n=1, 3, 5, 10). Units of the external applied field are displayed in kA/m. In the case of the vertical axis, (which corresponds to the measured anomalous Hall voltage) the units have been normalized.*

fields to occur. This is confirmed by the fact that the nucleation point becomes less defined for those films deposited on rougher substrates.

4.6 Magnetic characterization of Co/Pt multilayers

4.6.1 Influence of number of bilayers

Figure 4.3 displays the perpendicular hysteresis loops as measured by Anomalous Hall Effect of the first set of samples. Those samples correspond to multilayered films with the following configuration: Pt(10Å) / [Co(4Å)/Pt(10Å)] ×n, with (n=1, 3, 5, 10). All those films were deposited on a SiOx substrate. The SiOx substrate was grown by wet oxidation process at a temperature of 1150 °C.

In table 4.3 the values of nucleation field, coercivity and saturation field of those samples are listed. Figure 4.4 shows the dependence of the coercive and

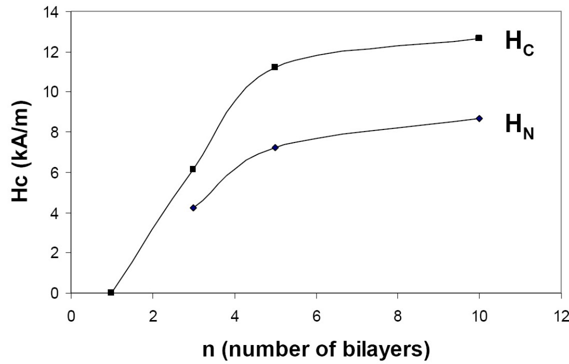

Figure 4.4: *Dependence of the coercive field (H_C) and nucleation field (H_N) of multilayered Co/Pt according with the number of deposited multilayers (n). The values of H_C and H_N were obtained by means of Anomalous Hall Effect measurement.*

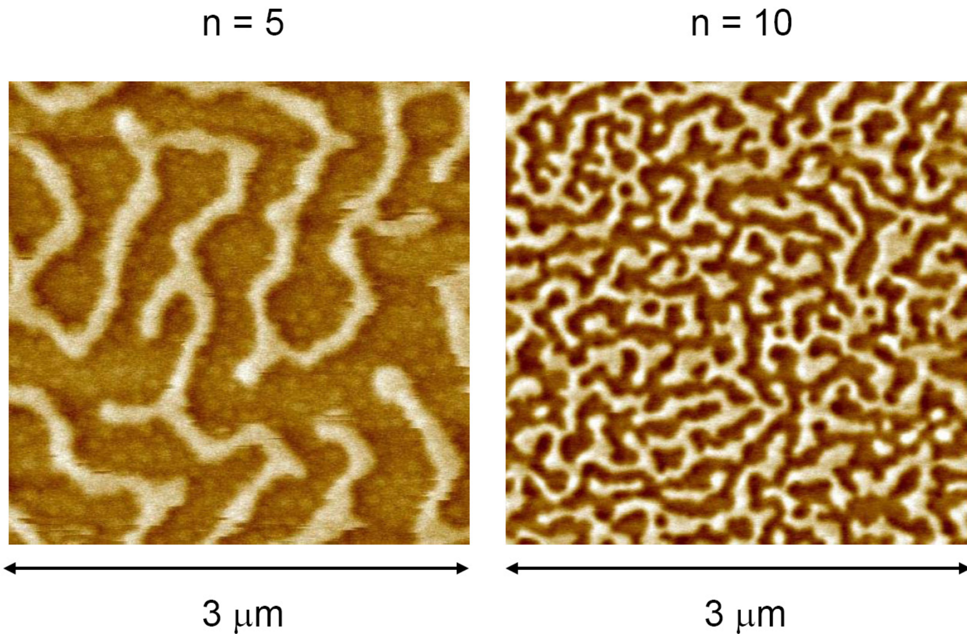

Figure 4.5: *MFM images showing the magnetic domains of $(Co/Pt) \times n$ samples for n = 5 and 10.*

n	H_N	H_c	H_s
1	-	~ 0	-
3	4.22	6.13	8.04
5	7.24	11.22	13.13
10	8.67	12.65	48.78

Table 4.3: *Values of nucleation field, coercive field and saturation field of multilayered Co/Pt films taken by means of Anomalous Hall Effect measurement. Data from four different samples are displayed, all of them deposited under the same sputtering conditions but consisting of different number of bilayers (n=1, 3, 5, 10).* H_N*,* H_c *and* H_s *are expressed in units of kA/m.*

nucleation fields on the number of bilayers in the samples.

From figure 4.3 and figure 4.4 it is observed that the coercivity and nucleation point increase as the number of deposited bilayers increases. In the case of 1 bilayer sample, the saturation field (H_s) is estimated as 25.96 kA/m. This is remarkable higher if compared with the 3 and 5 bilayer samples. One reason for this is that this film possesses a very weak perpendicular anisotropy since it has only one Co/Pt interface, thus most of its anisotropy is in the in-plane direction. This is confirmed by the fact that its remanence in the perpendicular direction is very small (zero for all practical reasons).

It is also observed from figure 4.3 that samples of 3 and 5 bilayers present squared loops. In the case of the sample of 10 bilayers it is observed that from saturation the magnetic moment of the films suddenly drops to zero. After that, the magnetization grows slowly in the negative direction until reaching its saturation. In the case of the sample with only one bilayer, no coercivity was found. It could be the case that the anisotropy of this film consisting of only two interfaces (Pt/Co/Pt) is too low to posses a measurable coercivity. Figure 4.5 displays two MFM images, one corresponding to the 5 bilayers sample and the other corresponding to the 10 bilayers sample, both of them in their demagnetized state. It is noticed that the domain size for the 5 bilayers sample is lower that for the other sample. In the case of the samples with 1 and 3 bilayers it was not possible to image their magnetic domains. It is thought that the samples were too soft to be imaged with the magnetic probe. MFM images of similar series of samples [76] have shown that the domain size in the demagnetized state decreases rapidly with increasing the number of bilayers.

From the four samples here discussed, the sample with the five bilayers configuration was selected for further investigation. This sample presents a higher coercivity than the 3 bilayers sample and still posses a squared hysteresis loop, which is not the case of the 10 bilayers configuration.

4.6.2 Influence of substrate

The second set of samples consisted to three films with the following configuration: Pt(40Å) / [Co(4Å)/Pt(10Å)] ×5. The seed layer of these samples is four times thicker than the samples discussed in the previous section in order to enhance the coercivity [45]. Each sample was deposited on a different substrate: pure Silicon (with its native oxide removed), SiOx grown by dry oxidation at 950 °C and SiOx grown by wet oxidation at 1150 °C.

Figure 4.6 shows the hysteresis loops of the three samples as measured by VSM. It is observed that the coercivity of the sample deposited on the SiOx substrates (grown by wet oxidation) is about 30 kA/m which is three times higher than the coercivity of the five bilayer sample deposited on the same kind of substrate but with a thinner seed layer (discussed in the previous section, figure 4.3). It is also observed that the hysteresis loop of the sample deposited on bare Silicon (4.6 top) is remarkable steeper if compared with the other two samples (4.6 middle and bottom), and its coercivity is one third of the other two samples.

4.7 Conclusions

The sample deposition process was decribed. Two kinds of magnetic multilayer films have been used, $Co_{50}Ni_{50}$/Pt and Co/Pt, both presenting perpendicular magnetic anisotropy.

It has been found that Silicon wafers with its layer of native oxide removed present a low surface roughness of 0.2 nm, which favours the growth of smooth sputtered layers.

The coercivity of the $Co_{50}Ni_{50}$/Pt samples decreases as the substrates become smoother. This could be explained by the fact that rougher substrates favour the formation of more defects in the films, which hampers domain propagation.

It was found that the magnetic reversal in the CoNi/Pt samples occurs in two steps. First the magnetic moments of the films drop drastically, and after that slowly increases to saturation in the opposite direction. This behaviour can be explained by the presence of vestigial domains which at the nucleation field expand into stripe-domains and demagnetize the sample. This rapid expansion might is to the fact that energy barriers for domain wall displacements are very small.

In the case of the Co/Pt multilayers, samples consisting of 1, 3, 5, and 10. It was observed that the nucleation field and coercivity increase as the number of bilayers increases. This might be due to the larger amount of defects present in the thicker samples. The samples with 3 and 5 bilayers presented square hysteresis loops. As the number of bilayers was increased the squareness was lost. The sample with 10, bilayers displayed a reversal behaviour occurring in two

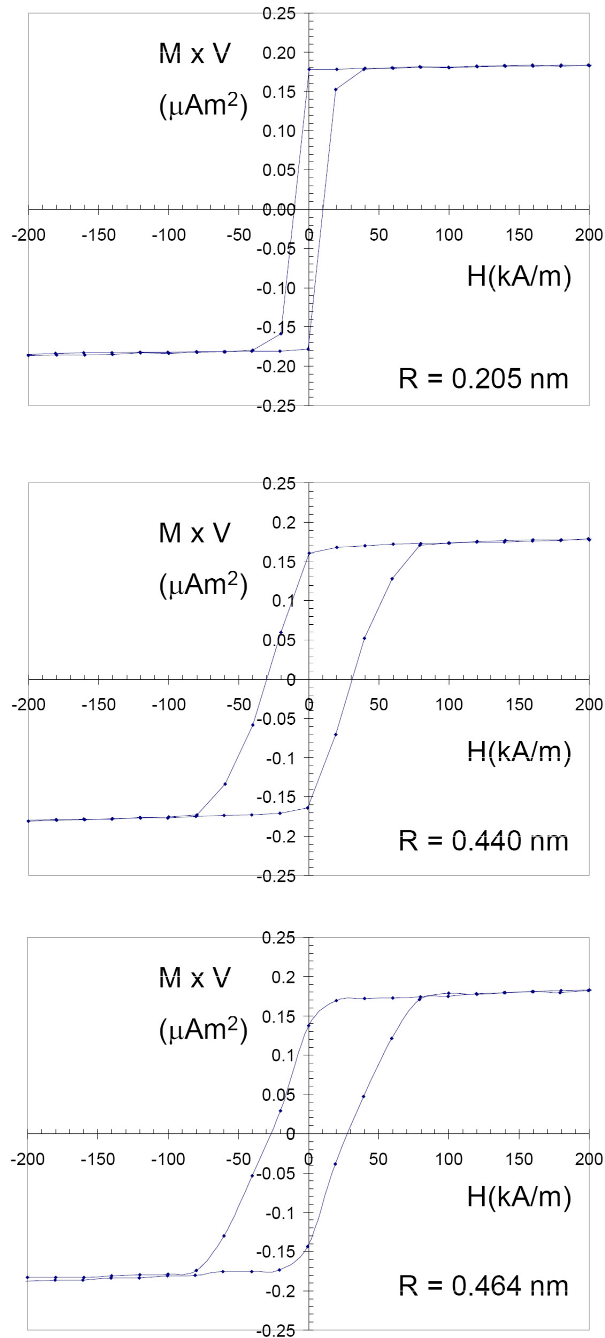

Figure 4.6: *Hysteresis loops of multilayered Pt(40Å)/[Co(4Å)/Pt(10Å)]×5 films deposited under the same argon pressure conditions but on different substrates as measured by VSM. The roughnes (R) of each substrate is displayed at the bottom corner of each graph. The three substrates consisted of pure Silicon (graph at the top), 590 nm thick SiOx grown by wet oxidation (graph at the middle) and 40 nm thick SiOx grown by dry oxidation.*

steps, equal to the behaviour already described for the CoNi/Pt samples, which suggest a similar reversal process than the CoNi/Pt samples already discussed.

The influence of the substrate roughness was explored in the case of the CoNi/Pt (consisting of 25 bilayers) and the Co/Pt samples (consisting of 5 bilayers). It was found that smother substrates favour steeper (more squared) hysteresis loops, sharper points of nucleation and lower coercivity.

Chapter 5

LIL patterning of CoNi/Pt and Co/Pt multilayers

The first step in the LIL processing consists in coating the sample (in this case the continuous magnetic films) with a *photoresist system*. Then the photoresist is exposed to the interference pattern produced by the LIL setup. Afterwards the resist is developed. Then an etching process follows in order to transfer the resist pattern into the sample. Finally, the photoresist system should be removed from top of the patterned sample. In this chapter we compare three different *photoresists systems* that were tested as part of this research. The first one is a single positive photoresist layer. The second consists of a three-layer system comprising an antireflection coating (ARC) at the bottom, an interlayer acting as a hardmask during the subsequent etching process, and a positive resist on the top. The third one is an image reversal resist acting as a shadow mask for the evaporation of a hard etching mask.

5.1 Schemes to fabricate arrays of dots

The three different approaches used here in fabricating arrays of magnetic dots are shown in figure 5.1. In the **first column** (*left*), the process consisting of photoresist islands acting as an etching mask on top of a magnetic film is represented. The uncovered magnetic material is removed by IBE while the covered material remains. In a final step the remaining photoresist should be removed from the top of the resulting dots. In the **second column** (*center*) the three-layer process is depicted. The photoresists islands are placed on top of a thin interlayer (SiO_2 in this case). Below the inter-layer an antireflection coating (ARC) is placed. Below the three layer stack are the magnetic film and the substrate. The photresist pattern is transferred to the interlayer by reactive ion etching (RIE) with CHF_3 (second diagram). After this the pattern is transferred again into

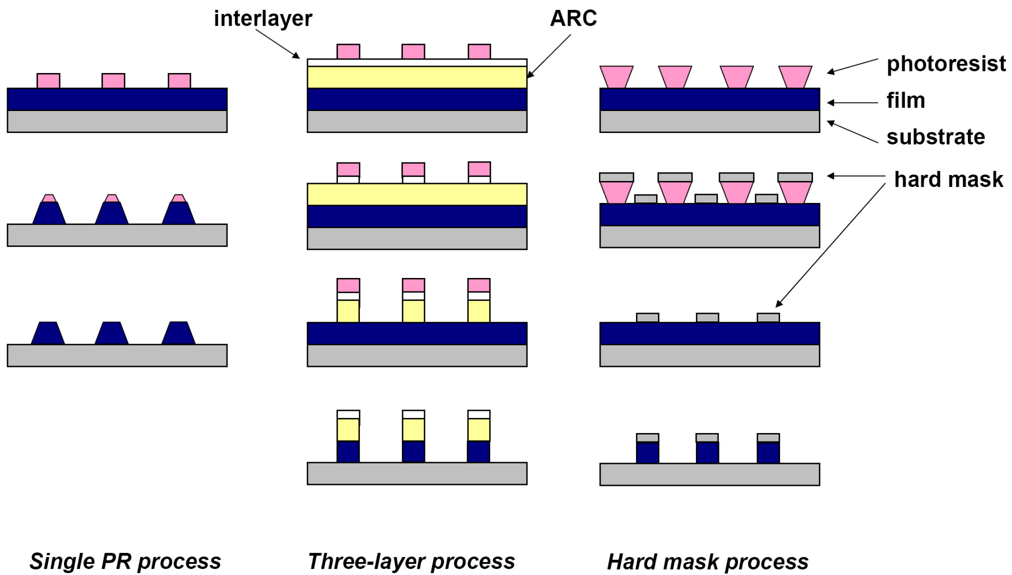

Figure 5.1: Different schemes in fabricating arrays of magnetic dots. *In the first column (*left*), the single PR process consisting of photoresist islands acting as an etching mask on top of a magnetic film. The uncovered magnetic material is removed by IBE. In the second column (*center*) the three-level process is represented. The photoresist is placed on top of a thin inter-layer which will serve as a hard IBE etching mask in a further step. Below the inter-layer an antireflection coating (ARC) is placed. In the third column (*right*) a hard mask process is depicted. Holes are produced through a photoresist on top of the magnetic film. Then a hard mask is deposited by evaporation. Then the resist is removed in a lift-off step and the magnetic material is etched.*

the ARC by a second RIE process with oxygen plasma (third diagram). The uncovered magnetic material is finally removed by IBE. In a further step, the remaining ARC and interlayer might be removed. Isues regarding the removal of these two layers will be discussed in one of the sections of this chapter. In the **third column** (*right*) a hard mask process is depicted. Holes (instead of islands) are produced through a photoresist coating on top of a magnetic film. Then a hard mask is deposited by evaporation, then the resist is removed in a lift-off step and finally the magnetic material is etched by IBE.

Ion milling was used to transfer the photoresist pattern onto the magnetic films. But it was found difficult to remove the etching mask after the ion milling process, which is also discussed in this chapter.

5.2 Single layer process (positive photoresist)

The photoresist used almost universally for optical micro-lithography is the DNQ system: a novolac resin with diazonaphthoquinone (DNQ) sensitizer. DNQ inhibits the dissolution of the novolac resin [84], however, upon exposure to light, the dissolution rate increases even beyond that of pure novolac [85]. The interaction between novolac and DNQ is still an area of active research [86, 87, 88].

Positive photoresist, OiR 907/12 (produced by ARCH Microelectronic Materials, Inc.), was used as a basis for our process. According to the manufacturers specifications (and our own ellipsometer measurements), when this resist is spin coated by 20 s at 4000 rpm and baked at 95 °C for 15 min, the resulting film thickness is about 1.2 μm. This is too thick for our purposes since the aspectratio of the PR mask becomes too high for fabricating submicron structures. Therefore, it has been decided to dilute the PR with two solvents, Ethyl 3-ethoxypropionate (EEP) and Methyl 3-methoxypropionate (MMP). The effect of different volumetric dilution ratios (PR:EEP:MMP = 5:3x:2x; for x = 0, 1, 1.5, 2 and 3) and spin-coating speeds was investigated, while keeping the bake-out conditions and spinning time constant. Figure 5.2 shows a series of plots which correspond to the final PR thickness as measured by ellipsometry. Each plot is the result of the average of at leats five measurements. Based on the experimental results, the following exponential expression was fitted to describe the variation in thickness as a function of the volumetric fraction of solvents present in the PR and the spin-coating revolutions per minute:

$$z = 2587 \times e^{-\left(\frac{x}{0.2798}+\frac{y}{9.1159}\right)}, \tag{5.1}$$

where x is the number of revolutions per minute (rpm) expressed in thousands of rpm, y is the volume fraction of solvents added to the original PR ($0 \leq y < 1$) and z is the PR final thickness expressed in nm. The diagonal lines in Figure 5.2 corresponds to the values of z as obtained by the expression (5.1). As expected, the film thickness decreases with increasing rotation speed and dilution.

Based on the former measurements, we decided for the preparation of the magnetic patterned samples to use a dilution of PR:EEP:MMP = 5:4.5:3, spin-coated by 20 s at 4000 rpm. This results in a film thickness of approximately 200 nm after being baked at 95 °C by 5 minutes. All the prepared mixtures of PR, EEP and MMP were filtered twice by using sieves with 200 nm diameter pores. OiR Photoresist Developer 4262 (OPD 4262) was used in the developing process with a development time of 30 seconds.

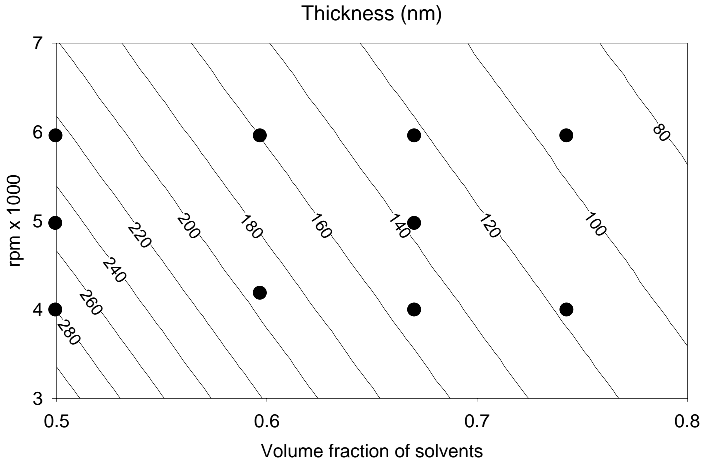

Figure 5.2: *Final thickness of the photoresist OiR 907/12 as a function of spin-coating revolutions per minute (rmp) and amount of added solvents. The dots correspond to experimental values, each plot is the result of the average of at least 5 measurements. The experimental values were fitted into an exponential function. The diagonal lines correspond to the expected thickness according to the fitted function.*

5.3 Vertical standing waves

During the LIL exposure (in addition to a horizontal pattern) a vertical pattern is produced into the photoresist. This is due to the presence of vertical standing waves caused by interference of the incoming light with light reflecting from the film surface. In Figure 5.3 there is a diagram representing a typical sample. At the top there is a photoresist coating, underneath there is the magnetic film and below it is found an underlayer (typically SiO_x, grown by thermal oxidation at a Silicon wafer) and at the bottom the substrate (a Silicon wafer in this case). Sometimes in between the photoresist and the magnetic film could be additional layers depending on the mask-stack chosen (e.g. hard masks for later etching steps). Two incoming laser beams reach the sample at the same angle and interfere with each other. However, the sample posses multiple optical interfaces, each one of them reflecting back a fraction of the incoming beam. The reflected light will then interfere with the incoming beams. In this way vertical standing waves are produced into the photoresist layer.

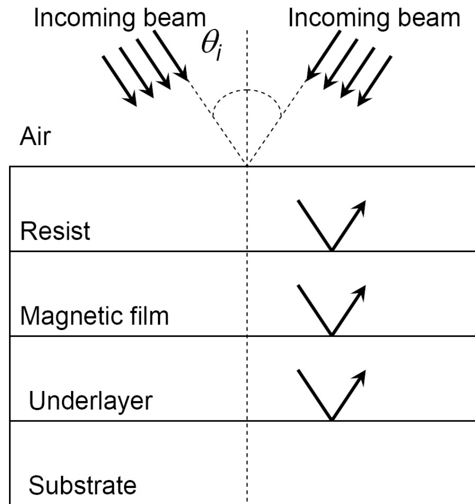

Figure 5.3: *Diagram showing different optical interfaces found within a LIL sample. Each of these interfaces will reflect a fraction of the incoming beams. The light reflected back will interfere with the incoming beams generating vertical standing waves within the sample. Thus a vertical pattern might be noticeable at the photoresist after development.*

The period of the vertical standing wave, $\Lambda_{vertical}$, is determined by the projection of the k-vector in the resist in the transverse direction. In Figure 5.4 k_m is assumed to be in the $+z$ direction, just like the projection of the k-vector in the x-direction that form the wanted lateral pattern.

The diagram depicted in Figure 5.4 also shows that the period of lateral (horizontal) standing wave is determined by the projection of the k-vector in that direction ($k_{m||}$) and is not determined by the refractive index of the incident medium but by the angle of incidence. Simply interchanging the incident medium with higher index material will not result in a lower periodicity per se.

$$\Lambda_{vertical} = \frac{\pi}{k_m cos\Theta_m} \tag{5.2}$$

Snell's law relates the angle of the incident medium to obtain,

$$\Lambda_{vertical} = \frac{\lambda}{2n_m cos\Big(arcsin(\frac{n_i}{n_m} sin\Theta_i)\Big)} \tag{5.3}$$

The resulting vertical interference pattern will produce PR structures with a number of periodic narrowed waists along them. The standard solution to this

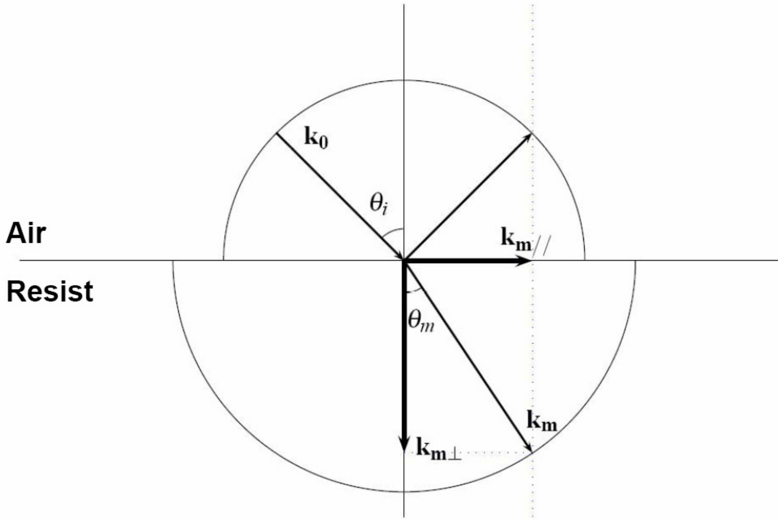

Figure 5.4: *k-vector construction showing the projection of the k-vector when refracted from air into a medium on the z-axis in the medium, which is in our case photoresist and denoted by $k_{m\perp}$. k_0 represents the wavevector in air.*

problem is to use anti-reflection coatings (ARC), which will be discussed first. It was found that for our particular process, ARCs cannot be used, so we propose a method based on high exposure doses, which will be discussed in the second part.

5.3.1 The use of antireflection coating (Trilevel resist process)

A standard procedure is to apply an ARC underneath the PR. High quality PR dots have been prepared with this method [53]. In the work reported here, XHRi-16 (produced by Brewer Science, Inc.) was used as an ARC. In order to be able to transfer the PR pattern through the ARC layer, a Trilevel Resist Process can be applied [89]. In this process a hard etch mask is deposited between the ARC and the PR (Figure 5.1 - Three-layer process). This hard etch mask should be resistant to the reactive ion beam etching of the ARC in subsequent processes. At the same time the index of refraction of the hard mask should be as close as possible to that of the ARC (1.730) and the resist (1.800). The best choice is SiO_2, with an index of refraction of 1.590. Because of these differences in the refractive indices, vertical standing waves cannot be completely suppressed, but can be minimized by carefully selecting the SiO_2 thickness [47]. The optimal thickness

Material	Complex refractive index	Reference
Resist	n = 1.800, k = 0.028	[91]
SiO_2	n = 1.590, k = 0.000	[92]
ARC	n = 1.730, k = 0.130	[93]
$Co_{50}Ni_{50}$/Pt multilayer	n = 1.300, k = 2.000	[94]

Table 5.1: *Refractive indices at a wavelength of 266 nm of materials used in the fabrication process*

has been found to be 62 nm for a wavelength of 266 nm. Figure 5.5 shows the calculated interference patterns in the vertical direction for a single PR stack, and for this optimized trilevel system. Table 5.1 lists the data used for this calculation. The calculations for the patterns shown in Figure 5.5 have been carried out with a Maple V® worksheet. [1]

To realize the trilevel system more process steps are needed than for a single PR layer process. Additionally, it is difficult to remove the ARC after ion beam etching. ARC-XHRi is a modified novolak resin, which is a thermal-set polymer that hardens during pre- and post-bake. It will not dissolve in acetone; therefore it is for instance very suitable for a lift-off process [90]. Standard removal procedures include ozone plasma strip, oxygen plasma, RCA Clean and Piranha. None of these methods can be applied because they will oxidize the cobalt layers. For large structures some oxidation can be accepted, because the oxidation process is self-limiting, but our dots are so small that the magnetic properties would seriously deteriorate. Because of these reasons it was found that the use of ARC was not suitable for our fabrication process.

5.3.2 Supra exposed single-photoresist process

The vertical standing waves (VSW) cause periodic areas of maximum intensity, which are responsible for the narrowed waists along the PR pillars. This periodicity depends on the angle of incidence, and increases with increasing Θ as depicted in (5.2) and (5.3). Above a certain angle the periodicity of the VSW is larger than that of the inference pattern on the film surface. If we choose the PR coating thickness below the periodicity of the VSW, its effect can be minimized. Additionally, by increasing the radiation dose the effect of the VSW can be further reduced. Figure 5.6 shows different scanning electron microscope (SEM) images of PR dots exposed at increasing exposure doses. For low doses the vertical standing waves produce wide plateaus or terraces around the dots, which are so wide that they even interconnect. When increasing the dose the terraces

[1]The code of the Maple worksheet used to calculate the reflectance of an absorbing 3-layer stack on an absorbing substrate was originally written in the SMI group by Marc Haast and modified by Sebastiaan Konings

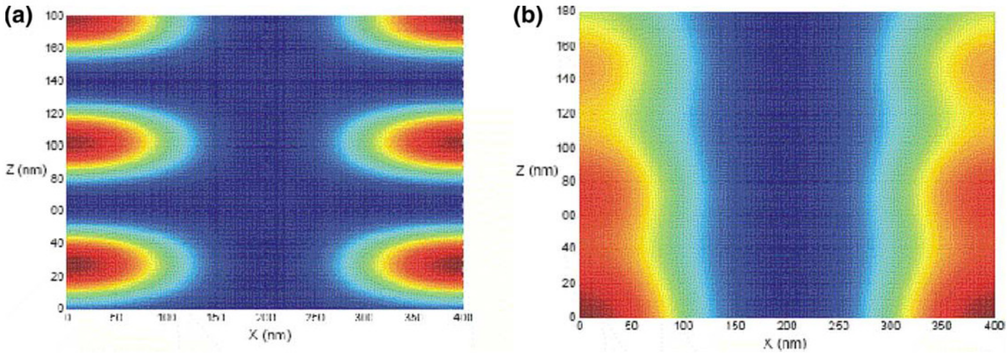

Figure 5.5: Calculated interference pattern occurring in the PR layer (z is the direction normal to the substrate) for (a) the case with a single PR and (b) the case with a trilevel system with SiO_2 (62 nm) as interlayer.

decrease in size and start to disconnect. For even higher radiation doses the terraces become negligible. In figure 5.7, the profile of the PR dots produced by this supra-exposure technique is shown, and it can be observed that the VSW are strongly suppressed. This supra-exposure technique only works if the two interfering laser beams are equal in intensity. When they are not equal, there will not be complete destructive interference and the resist will be overexposed everywhere. Therefore, we use a dielectric mirror with a reflectivity of more than 99%.

5.4 Ion beam etching

By means of ion beam etching (IBE) the PR pattern is transferred to the magnetic film. Different problems have been encountered during the IBE step like faceting [62] and sidewall deposition. Part of the deposited material is originating from the acceleration grid [95] however this effect can be reduced by decreasing the acceleration voltage. The other part is redeposited magnetic material, which can be removed by varying the etching angle [62]. Different tests have been done using two different acceleration voltages, 350 and 100 V and various angles. The etch time was kept constant at 8 min with argon pressure of 3×10^{-4} mbar. Figure 5.8(a) shows the resulting structures after etching with a voltage of 350 V and an angle of 20°. The structures present irregular edges and sidewall deposition. Remains of PR were difficult to remove. Figure 5.8(b) shows the results of etching under the same acceleration voltage but at an angle of 0°. The structures are irregular and heavily damaged. Figure 5.8(c) shows structures etched at an acceleration voltage of 100 V and under an angle of 0°. The shapes look more regular, but sidewall deposition is observed at the base of the structures. Figure

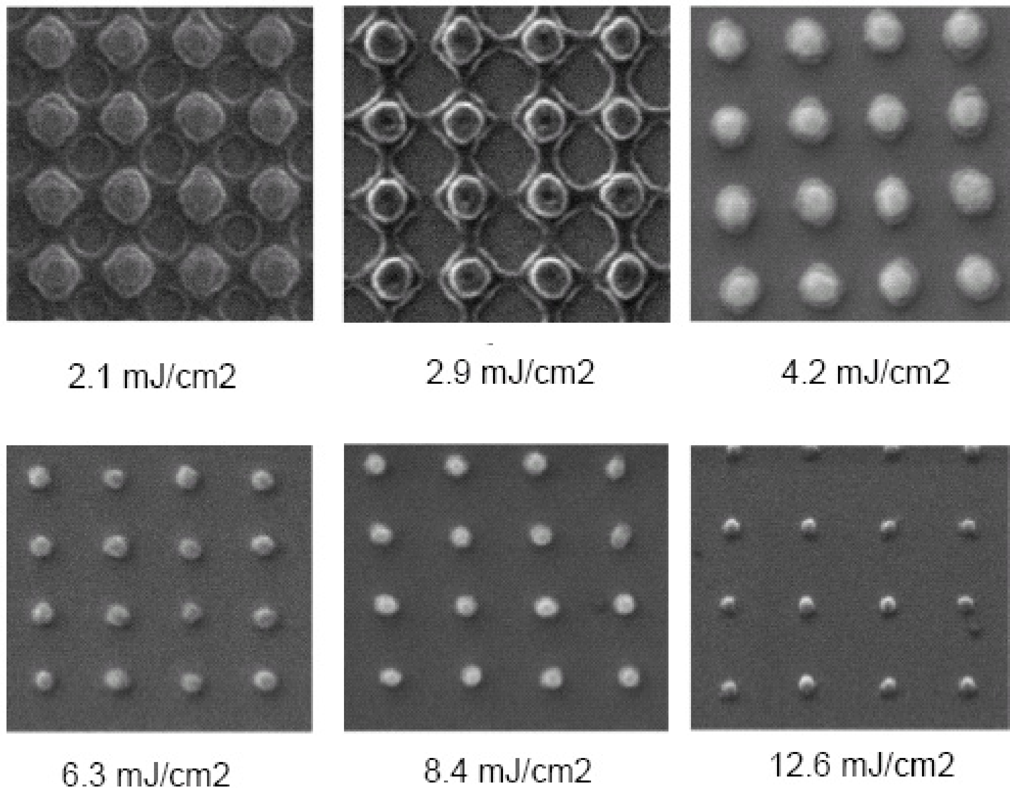

Figure 5.6: *SEM images of structures produced on photoresist by double LIL exposure. For low exposure doses (2.1 and 2.9 mJ/cm^2) it is possible to see plateaus of photoresist surrounding the photoresist dots. The plateaus are so big that they are even interconnected with each other. Increasing the exposure dose reduce the size of the plateaus produced by the vertical standing waves (4.2 mJ/cm^2). Further increasing the exposure dose has the effect of vanishing the photoresist plateaus and reducing the diameter of the photoresist dots (6.3, 8.4 and 12.6 mJ/cm^2)*

5.8(d) shows the result of etching at 100 V at an angle of 0°by 7 min and a final etching at 60°by 1 min. Almost no sidewall deposition was observed and PR was easier to remove, so we conclude the sidewall deposition has been removed while etching at 60°. However, the structures are more rounded because of the high-angle etching step. We expect this will deteriorate the magnetic properties of the dots. Good quality magnetic nanodots are a compromise between reasonable regular shapes with straight sidewalls and sidewall deposition.

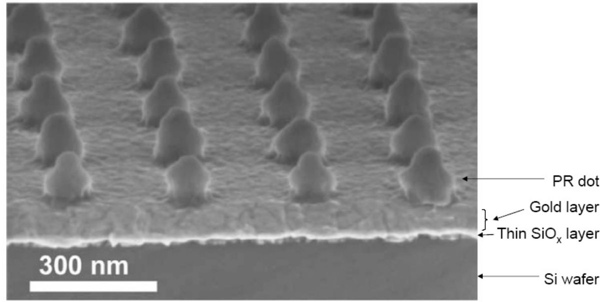

Figure 5.7: *SEM image showing the profile of PR dots with 300 nm of periodicity arranged in a squared grid. The radiated dose was 6.3* mJ/cm^2.

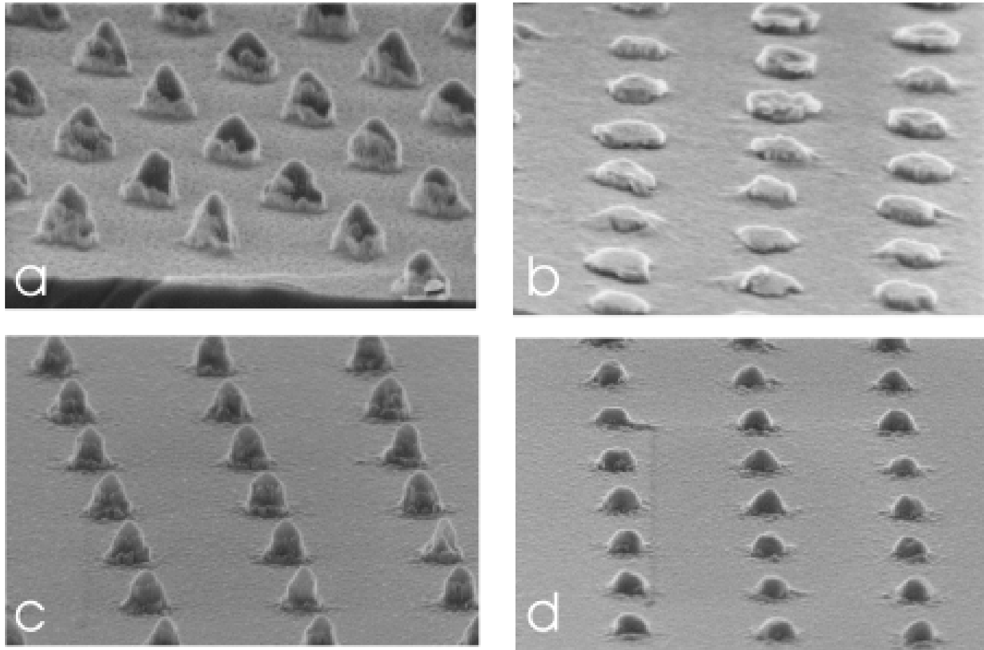

Figure 5.8: *SEM images showing the profile of nanomagnets fabricated under different IBE conditions: (a) acceleration voltage: 350 V, etching angle 20 by 8 min, periodicity = 350 nm; (b) acceleration voltage 350 V, etching angle 0 by 8 min, periodicity = 300 nm; (c) acceleration voltage: 100 V, etching angle 0 by 8 min, periodicity = 400 nm; (d) acceleration voltage 100 V, etching angle 0 by 7 min and 60 by 1 min, periodicity = 400 nm.*

Solvent name	Composition
Acetone	C_3H_6O
PRS-2000	Diethylene glycol monoethyl ether N-methylpyrrolidone Tetraethylene glycol
Microposit	1- methyl-2-pyrrolidine Pyrrolidone compound

Table 5.2: *Composition of three solvents (Acetone, PRS-2000 and Microposit) typically used for photoresist removal*

5.5 Photoresist removal

After developing the photoresist (diluted OiR 907/12), when the exposed areas are dissolved, the wafer is subjected to IBE in order to locally etch away the magnetic multilayer structure. Preliminary experiences suggested that IBE could affect the developed PR pattern. After IBE treatment, the remaining PR seemed to be insoluble in the commonly used acetone-based stripper, quite large amounts of PR remained stuck on the metallic dots. AFM measurements had shown the thickness of the PR residue to be about 80 nm. It has been found that after an IBE process, the removal of the PR mask on top of the etched structures turns to be difficult. Since the signal-to-noise ratio in MFM measurements strongly depends on the tip-medium distance, any PR residue should be, preferably, removed. [2]

It was thought that, under action of IBE, the PR suffered structural changes: carbonization or cross-link formation. A diffusion-based metal-PR interface mixing could also be an explanation, when metal particles and large polymer molecules formed a very tough composite material.

Preliminary studies also indicated that during IBE redeposition occurs around the bases of the dots. This sidewall formation had been thought to be in connection with encountered PR removal difficulties.

Three different solvents (Acetone, PRS-2000 and Microposit) were used in order to find a standard mask removal procedure. Table 5.2 displays the composition of the solvents here used. All samples used were deposited by sputtering of Platinum and an alloy of Cobalt and Nickel, consisting of one Pt seed layer and 26 bilayers of $Co_{50}Ni_{50}$ / Pt. The thickness of each individual layer was 0.6 nm. The samples were patterned into a periodicity of 300 nm and their dots

[2]For the purposes of this work MFM measurements are specially important, not only because MFM is one of our characterization tools, but because we used MFM probes in order to do bit-write/red experiments (this will be explained in the next chapter).

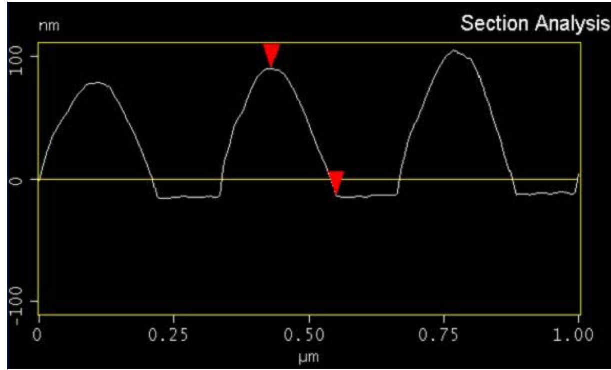

Figure 5.9: *AFM section image of 300 nm periodicity $Co_{50}Ni_{50}$/Pt multi-layered dots after ultrasonic cleaning with* Microposit *by 3 hours at 45 ^oC. The section image displays a vertical distance between top and basement of a dot of 103 nm.*

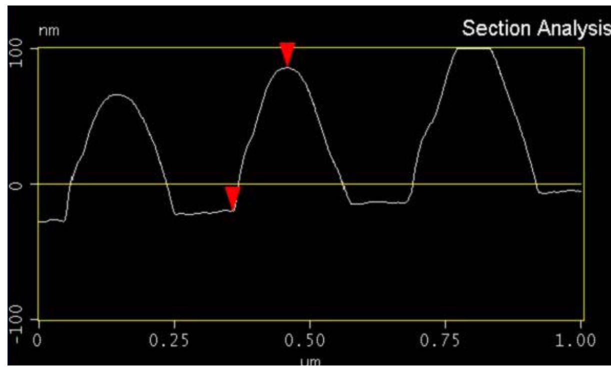

Figure 5.10: *AFM section image of 300 nm periodicity $Co_{50}Ni_{50}$/Pt multi-layered dots after ultrasonic cleaning with* PRS2000 *during 3 hours at 45 ^oC. The section image displays a vertical distance between top and basement of a dot of 106 nm.*

diameter was about 70 nm after the etching step. The IBE was performed at an acceleration voltage of 350 V with and etching angle 20°by 8 min. After the IBE step the samples were immersed in one of the solvents at 45 ^oC by 3 hours in an ultrasonic cleaning unit with a frequency of 40 kHz and a power of 320 W. In all cases we observed from SEM and AFM images taken before and after an ultrasonic cleaning process that the photoresist was not removed.

Figure 5.9 shows an AFM section image of $Co_{50}Ni_{50}$/Pt dots with a periodicity of 300 nm after being ultrasonic cleaned in Microposit according to the specifications already mentioned. In the section image the vertical distance be-

tween the top and the basement of the central dot is 103 nm. Figure 5.10 shows an AFM section image of a similar sample which was ultrasonic cleaned in PRS 2000. In this case the vertical distance between the top and the basement of the central dot is 106 nm. In the case of the sample cleaned with acetone, similar results were obtained.

Assuming a multilayer thickness of 30 nm, these results indicate a photoresist thickness after the ultrasonic cleaning of about 80 nm. In order to have a good resolution while imaging the dots by MFM we need to be able to approach the magnetic tip at a distance of about 10 nm to the magnetic layer.

Other standard photoresist removal procedures include ozone plasma strip, oxygen plasma, RCA Clean and Piranha. All these methods will oxidize the cobalt layers of the dots and therefore damage the magnetic properties of the samples. However those methods are quite efficient. Figure 5.11 shows a SEM image of a sample consisting of 300 nm periodicity gold dots after IBE and ultrasonic cleaning in acetone by 3 hours at 45 ^{o}C. As can be seen, large amounts of photoresist remain on top of the gold dots. This is the reason for the *sombrero* shape of the dots. Figure 5.12 shows a SEM image of the same sample which was taken after the 3 hour ultrasonic cleaning with acetone into an oxygen plasma cleaning by only five minutes. It can be observed that after the oxygen plasma cleaning the photoresist was removed. The small square at the right top of figure 5.12 corresponds to the previous figure (figure 5.11) and displays the state of the gold dots just before the oxygen plasma cleaning process. Apparently oxygen plasma cleaning is a very efficient method to remove residual photoresist after an IBE process, unfortunately it is not compatible with our magnetic multilayer stacks.

One last method was tried in order to remove the residual photoresist on top of the magnetic dots. It consisted in using an AFM tip while scanning at contact mode. By doing this all the dots in an area of 50×50 μm were scratched and the resist on top of them wiped away. Figure 5.13 shows an AFM section of a sample after scratching. The section image displays a vertical distance between top and basement of a dot of about 35 nm. The scanned area was also inspected with an optical microscope. In figure 5.14 it is possible to observe a different colour hue on the wiped square surface compared to the outside area. Rests of the wiped photoresist and redeposited material can be observed at the edges of the cleaned square.

Since scratching is the only way to remove resist without damaging the magnetic multilayer, all samples fabricated from positive tone photoresist and analysed in this work by MFM measurement (see Chapter 6) have been treated in this way.

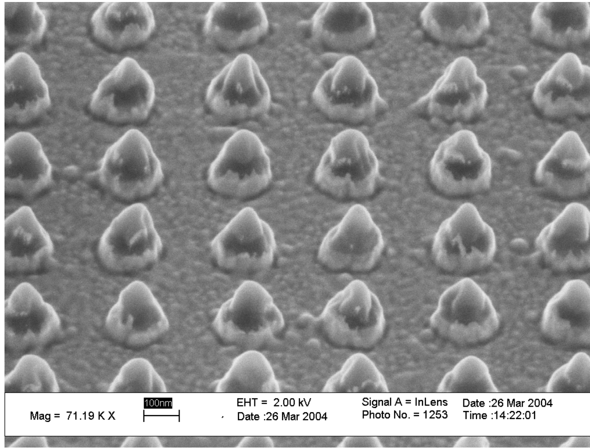

Figure 5.11: *SEM image of 300 nm periodicity gold dots after IBE and ultrasonic cleaning with acetone by 3 hours at 45 °C. Photoresist could not be removed.*

5.6 The use of reversal image photoresist in combination with the hard mask process

An alternative process is desired in which the magnetic dots are free of any photoresist. This would allow better MFM characterization and performance in read-write experiments using magnetic scanning probes. In this section a fabrication process consisting in making holes in a photoresist coating (instead of islands) is explored.

While trying the hardmask scheme approach TI04XR photoresist was selected. This is a diluted experimental version of the commercial TI09XR mixed by the manufacturer. The TI04XR resist can work in image reversal mode. Alternatively, it can be processed as a conventional positive resist if the reversal bake step is avoided [96]. Photoresist processing was based on previous work done in the SMI group [97, 98].

Figure 5.15 shows a scheme of the image reversal procedure. After exposure, the resist acts as a positive resist. Then an image reversal bake takes place and cross-links are formed at exposed area while the unexposed area remains photoactive. The resist is *flood-exposed* with a UV lamp that makes the resist not exposed in the first step soluble in the developer. Finally, the areas exposed in the first step remain after developing [50]. This resist has the special characteristic that when used in its image reversal mode, the holes produced present inverted walls. This allows for using the holed patterns as shadow masks.

The material used as a hard mask was Titanium. The deposition of Titanium

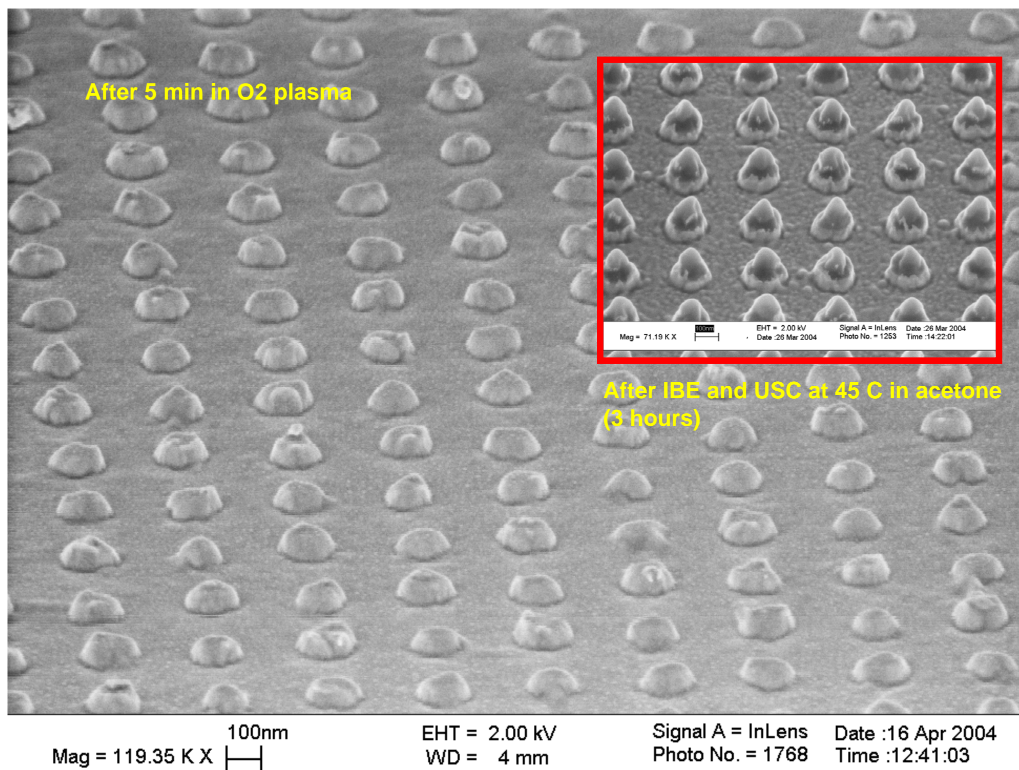

Figure 5.12: *SEM image of the 300 nm periodicity gold dots displayed in figure 5.11 after IBE, ultrasonic cleaning with acetone by 3 hours at 45°C, and 5 minutes in oxygen plasma. After the oxygen plasma cleaning the photoresist was removed. The small square at the right top of the image corresponds to figure 5.11 and displays the state of the gold dots just before the oxygen plasma cleaning process.*

was performed in an electron-gun evaporation system (Balzers BAK 600). The evaporated layers must be thick enough to act as an etch mask. On the other hand, thin layers are desired to prevent sidewall deposition of magnetic material.

Considering the magnetic multilayer used in these experiments to be 24 nm, and assuming the Titanium etch rate to be half of the multilayer etch rate, it was decided to deposit a 12 nm Titanium mask.

5.7 Dots produced with the hard mask process

The hardmask scheme has yielded satisfactory results when producing dots with diameters of 300 nm and periodicity of 600 nm (Figure 5.16). The resist

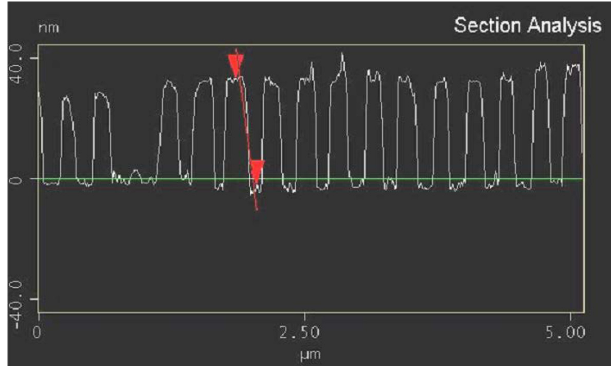

Figure 5.13: AFM section image of 300 nm periodicity $Co_{50}Ni_{50}$/Pt multilayered dots after scratching with an AFM tip while scanning in contact mode. The section image displays a vertical distance between top and basement of a dot of 35 nm.

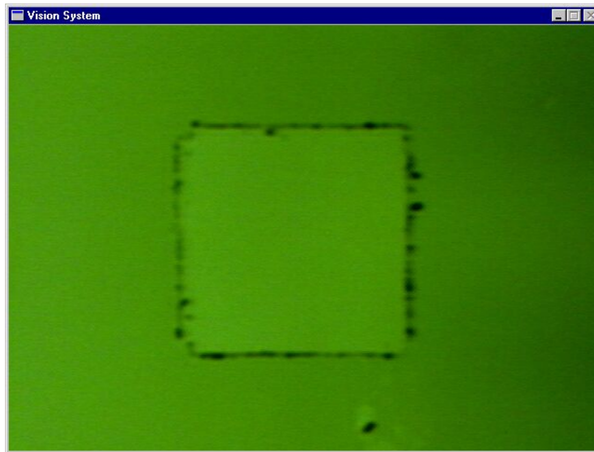

Figure 5.14: Optical microscope image showing an area of 50 x 50 μm that was scratched with an AFM tip while scanning in contact mode. It is possible to observe a different tone on area outside the square. Remains of the removed photoresist and redeposited material are seen at the square edges.

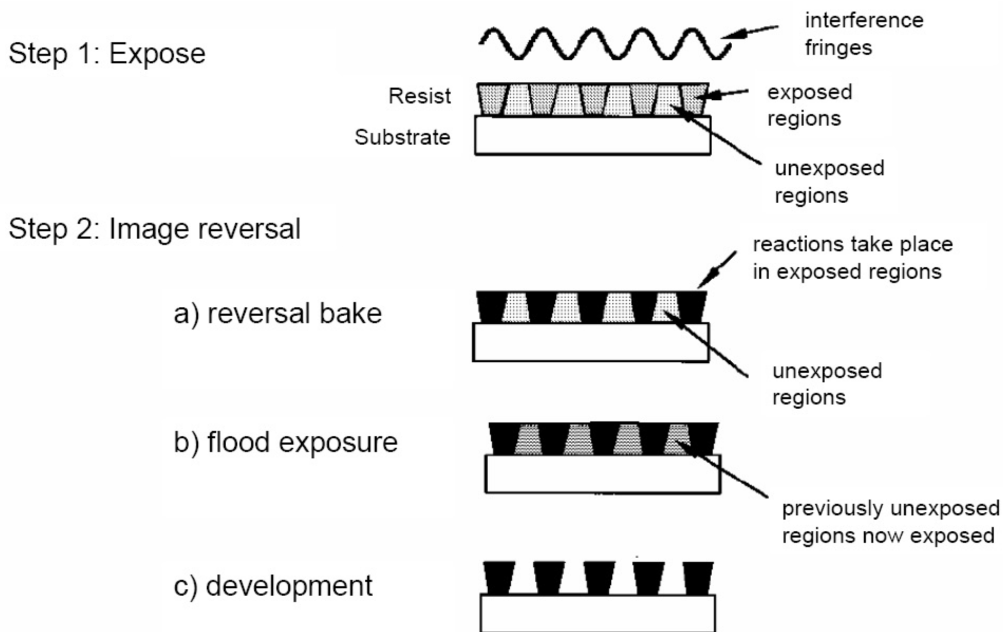

Figure 5.15: *Process steps to generate holes with image reversal (figure from [50]).*

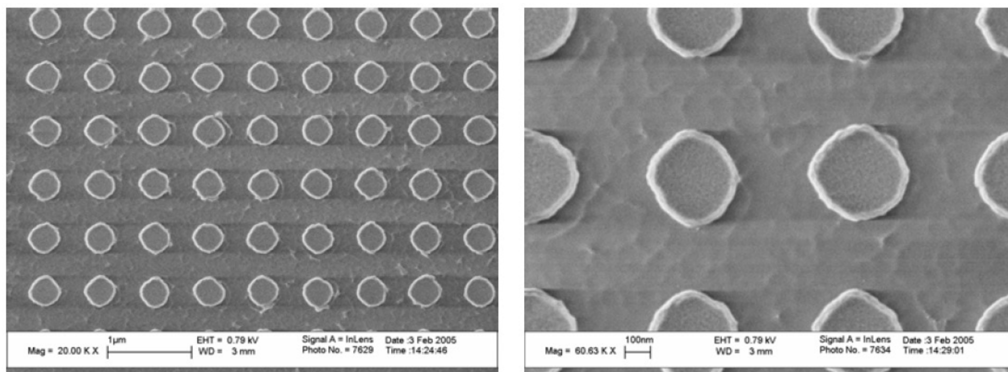

Figure 5.16: *SEM image of magnetic dots with a periodicity of 600 nm etched by using a Titanium hardmask (images from [98])*

was easily removed after the Titanium evaporation, since it was not yet been exposed to IBE. However the attempts to fabricate quality magnetic dots with 300 nm period failed, because deposition of Titanium turned critical when working with small resist holes. The resist walls are easily covered during the evaporation since the inverted wall profile of the image reversal photoresist is not very well defined in these small structures. This makes it extremely difficult to remove the resist.

Even when the use of image reversal photoresist appears promising as a fabrication method for magnetic nanodots, further work is still required to produce good quality hardmasks when reducing the features size.

5.8 Conclusions

The LIL patterning process was described. As part of the fabrication experiments two kinds of photoresist were explored, one positive resist and one image reversal resist. Three different etch masking systems were studied, a simple etching mask compound only by the patterned photoresist coating, a trilevel stack using a bottom antireflection coating, and a hardmask approach in combination with the image reversal photoresist. Problems concerning the IBE process and the photoresist mask removal afterwards were also discussed.

In order to diminish or suppress vertical standing waves in the photoresist after LIL exposure, a bottom antireflection coating within a tri-layer scheme was tested first. Different inconveniences were found by using this method. First of all the thickness of the SiO interlayer acting as a hard mask had to be careful chosen because of differences in the diffraction indices of the photoresists, the antireflection coating and the SiO interlayer itself. Because of those differences in diffraction indices the vertical standing waves could be attenuated but never totaly suppressed. Besides that, problems in removal of the antireflection coating after ion beam etching process were found. Presumably, this is due to polymer crosslinking during the baking of the antireflection coating [90].

Next, a single-layer approach was attempted. It consisted of a thin coating of diluted positive photoresist. The problem of vertical standing waves was addressed by using a high exposure dose (supra-exposure scheme). By increasing the exposure dose and using a highly reflective mirror to achieve good contrast, it is possible to control the size of the photoresist dots and to diminish the prescence of terraces or plateaus due to the presence on vertical standing waves. This method is preferable because the resist stack is simple and the etching process only includes one etching step (IBE). This in contrast with the tri-level approach in which three reactive ion etching steps plus one ion beam etching step are required (One RIE step to go through the photoresist on top of the stack, one RIE step to go through the SiO in the middle and one RIE step to go through the

antireflection coating at the bottom. Plus an IBE step to go through the magnetic film).

Removal of the photoresist acting as an etching mask is problematic in samples prepared by using the single-layer stack approach. Different organic solvents were used in combination with ultrasonic cleaning to remove the remains of photoresist, but all of them failed. Conventional methods like oxygen plasma or acids have proven to be quite effective, but they can oxidize the magnetic material within the dots. Thus no oxidizing cleaning methods are suitable for our processes. Therefore, mechanical removal of the remaining photoresist has been found to be the safest method. This has been done by *wiping* small areas of the samples by using an AFM probe in contact mode, more or less acting as a *broom*.

The problem of photresist removal after IBE was circumvented by using a hard mask approach using reversal image photoresist and lift-off. With this method holes are patterned into a photoresist, spin-coated on top of the magetic film. Then a hard mask (in this case Titanium) was deposited by evaporation. Afterwards the complete photoresist mask is removed, leaving the hard mask dots behind which can be than be used for etching the magnetic layer. The hardmask scheme yielded satisfactory results when producing dots with diameters of 300 nm and periodicities of 600 nm. However, difficulties were found when attempting to produce smaller structures. Depositing Titanium by evaporation through holes with small diameters turned out to be critical since the hole walls became covered with Titanium, which frustrates the lift-off process. Further work is necessary to deposit high quality hardmasks through patterned photoresist masks.

From the three fabrication methods, the single-resist approach (using supra-exposure) is the easiest to implement and yields the best results. However further research is necessary into the removal of remaining photoresist after IBE. Nevertheless, the hardmask approach should still be investigated since it seems to be a promising candidate. It is necessary to be able to achieve a good control on shape and size of the holes. Deposition methods for the hardmask, other than evaporation, should be explored.

Chapter 6

Magnetic properties of CoNi/Pt and Co/Pt patterned films

Thermostability and switching field distribution are two important parameters for any recording medium. A thermal stable material will warranty that the stored information will remain unchanged for a long time. On the other hand, a lower switching field distribution means that in such a medium each bit of information can be written by exerting the same (or at least a similar) magnetic field, which helps to avoid side writing.

In the analysis of the dots the coercivity plays an important role. Because of this reason, in the first section of this chapter we will consider an ensemble of nanomagnets and we will derive an expression which relates the coercivity of the ensemble with its internal energy. By using that expression (in combination with experimental data) a study on the thermal stability and distribution of the switching field of arrays of CoNi/Pt and Co/Pt dots is presented. Those structures have diameters around 90 nm and a periodicity of 300 nm. The thermal dependence of the averaged switching field has been investigated by means of VSM. Additionally the switching field distribution at room temperature has been studied by performing VSM remanent measurements and MFM measurements.

6.1 Coercivity in the case of a group nanomagnets

In general, the energy barrier of a group of particles with uniaxial anisotropy is described by the following expression [37]:

$$\Delta E = U\Big(1 - \frac{H}{H_0}\Big)^n, \tag{6.1}$$

where U is the energy barrier at zero applied field, H is the applied field and H_o is the field needed at zero temperature to overcome the energy barrier. The value n depends on the switching mechanism within the system, $n = 1$ for weak domain-wall pinning [99, 100], $n = 3/2$ in the case of an ensemble of particles with a Lorentzian switching-field distribution and coherent magnetization rotation [101], and $n = 2$ in the case of a group of identical Stoner-Wohlfarth particles. [102].

As previously explained in Chapter 2, the switching probability rate as a function of the energy barrier and temperature can be phenomenologically described by the Arrhenius relation [36],

$$r = f_0 \exp\left(-\frac{\Delta E}{kT}\right). \tag{6.2}$$

In the case of a set of uniaxial particles it is possible to define the coercivity as the applied field at which the probability of being already switched after a time t is $1/2$ [38] (i.e. $rt = 1/2$).

Combining equations (6.1) and (6.2) and using the definition above it is possible to express the coercivity as

$$H_c(t,T) = H_0\left(1 - \left(\frac{kT}{U} ln(2f_0 t)\right)^{1/n}\right). \tag{6.3}$$

The latest expression will be used in coming sections in order to determine the internal energy (U) and coercivity at zero field and zero temperature (H_0) of the arrays of dots. This can be done by performing coercivity measurements at different temperatures.

6.2 Analysis of CoNi/Pt dots

In figure 6.1 four hysteresis loops of a $Pt(6\AA)/[CoNi(6\AA)/Pt(6\AA)] \times 26$ sample deposited on silicon oxide are presented. The graphs on the left corresponds to the continuous film, while the graphs on the right corresponds to the patterned film consisting of an hexagonal array of nanodots with a periodicity of 300 nm. We will comment first on the perpendicular hysteresis loops. It is possible to observe from the graphs that in the continuous film nucleation occurs at -16 kA/m and the point of coercivity is found at $+3$ kA/m. In the case of the patterned film there is not a sharp nucleation point, and coercivity has increased up to 70 kA/m. From the coercivity field at 70 kA/m the sample magnetization steadily increases up to a field of 210 kA/m. After 210 kA/m the slope changes

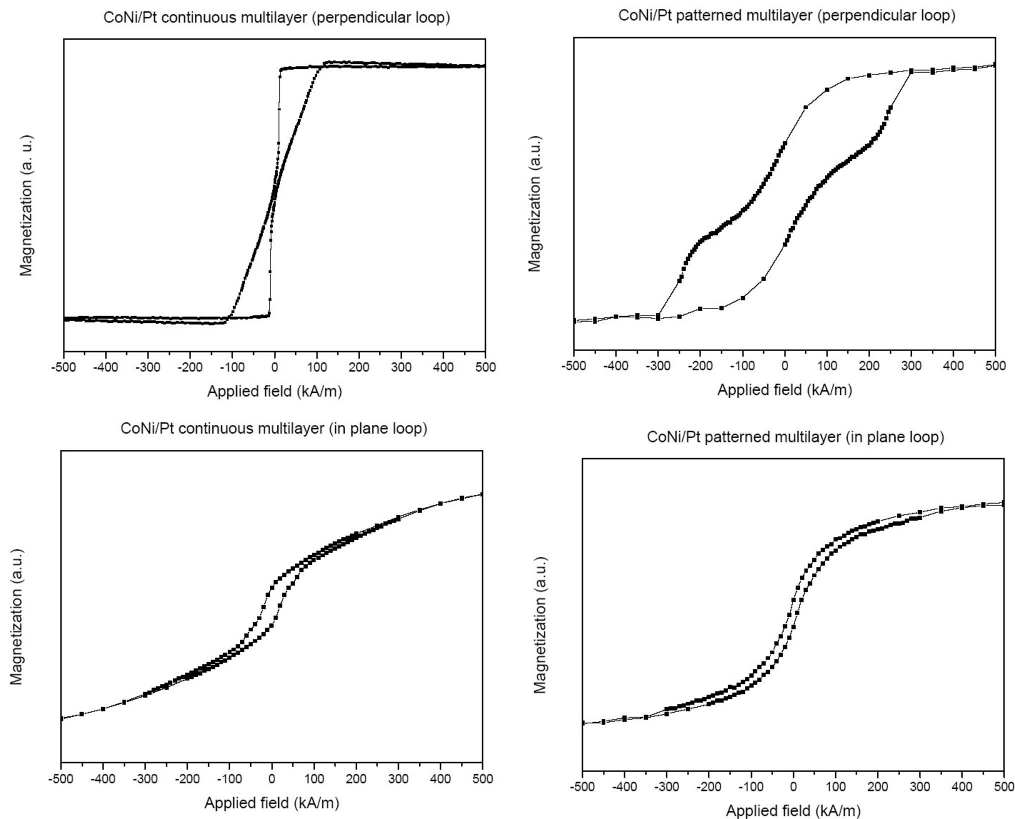

Figure 6.1: *VSM hysteresis loops of continuous (left) and patterned (right) CoNi/Pt multilayers. On the top row, the perpendicular hysteresis loops are displayed, and in the bottom row the in plane loops. The patterned film corresponds to an hexagonal array of dots with a periodicity of 300 nm and dot diameter of 90 nm.*

and the magnetization increases faster as a function of the applied field. Saturation is reached at 300 kA/m. The presence of two different slopes may indicate the presence of two different magnetic materials within the sample. Material redeposited on the dots walls during the ion beam etching process is an explanation of this behaviour. As to the in plane hysteresis loops, we can observe a small coercivity, which suggests the presence of a small anisotropy field which could be related in both cases to shape anisotropy.

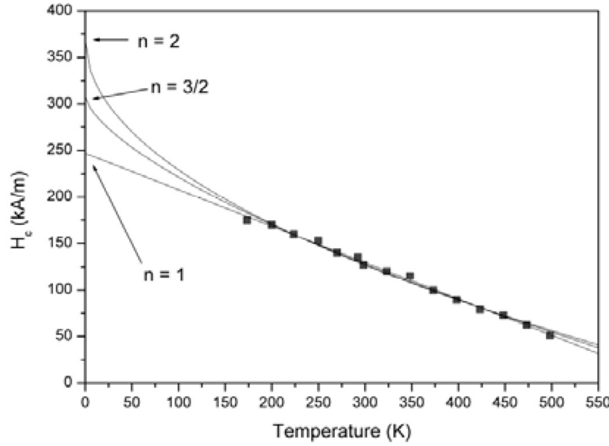

Figure 6.2: *Temperature dependence of the coercivity in the array of dots. Three different fittings for the experimental data are shown, by using different values of n.*

Value of n	H_0 (kA/m)	$U(J)$	$V_s(nm^3)$
1	246.9	1.87×10^{-19}	1.2×10^3
3/2	307.9	1.98×10^{-19}	1.3×10^3
2	368.8	2.06×10^{-19}	1.4×10^3

Table 6.1: *Estimated values for the switching field (H_0), energy barrier (U) and switching volume at zero temperature (Vs) for the different values n.*

6.2.1 Thermostability of CoNi/Pt dots

Using VSM, the hysteresis loops of the CoNi/Pt patterned film were measured at different temperatures, ranging from 175 to 500 K. The temperature dependence of the coercive field for the hexagonal array of CoNi/Pt nanodots is shown in Figure 6.2. Each coercivity value is an average of 20 measurements. The experimental data was fitted into three different expressions derived from equation (6.3) by using the three different values of n that were mentioned before and a value of $f_0 t = 10^9$. The fits are also displayed in Figure 6.2. However, based solely on this information it is not possible to determine which is the most suitable value for the n, since on the range of temperatures studied the three functions behave very similar. From the fits, the values for H_0 and U were estimated for $n = 1$, $3/2$, and 2. Those values are displayed in Table 6.1. The fitted values for the energy barrier at zero field, U, ranges from 1.87×10^{-19} till 2.06×10^{-19} J (1.16 - 1.28 eV), corresponding to a $\Delta E/KT$ ratio from 45.0 to 49.7 . Thus, regardless of the switching model used, the dots have a sufficiently high

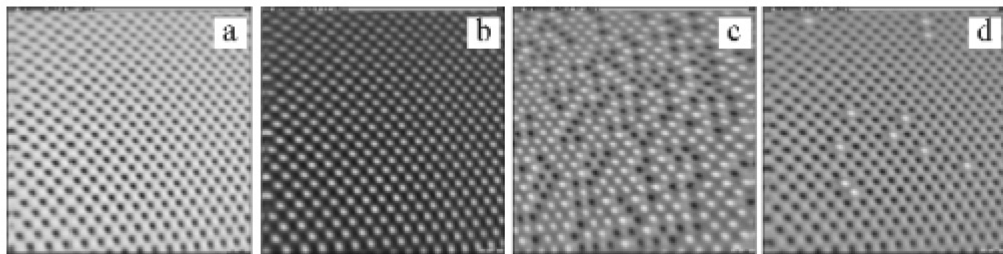

Figure 6.3: MFM images of a patterned CoNi/Pt multilayer film after application of $-1350, +4, +127, and + 183kA/m$.

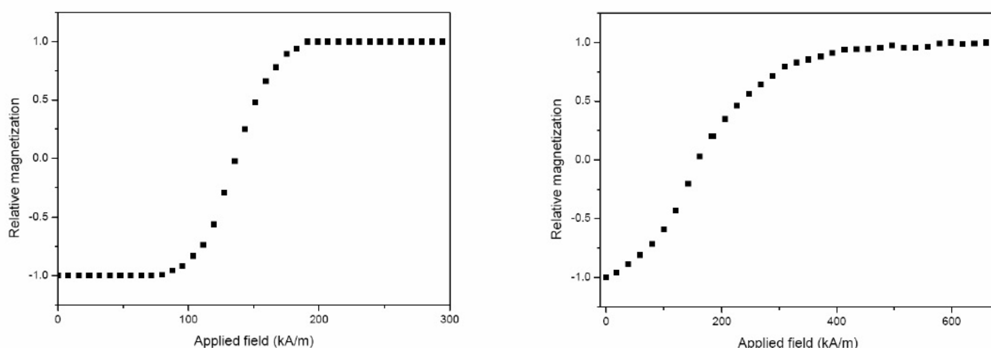

Figure 6.4: Left: Remanence curve obtained by MFM, the vertical axis corresponds to the fraction of the switched dots for each applied field. Right: Remanence curve obtained by VSM, the vertical axis corresponds to the relative magnetization of the sample.

energy barrier for long term stability. Furthermore, U can be written as $K_{eff}V_s$, where V_s, is the switching volume. By using the value of the effective anisotropy, determined by torque measurement as $150kJ/m^3$ [45, 103], it is possible to estimate the values of the switching volumes, which are also displayed in Table 1.

6.2.2 Remanence and switching field distribution of CoNi/Pt dots

Using a MFM, a series of field dependent measurements were made in order to measure the switching fields of individual dots localized in very specific areas of our samples. By doing this and comparing with the VSM measurements it is possible to draw some conclusions regarding the homogeneity and uniformity of the magnetic properties of the dots all over the sample.

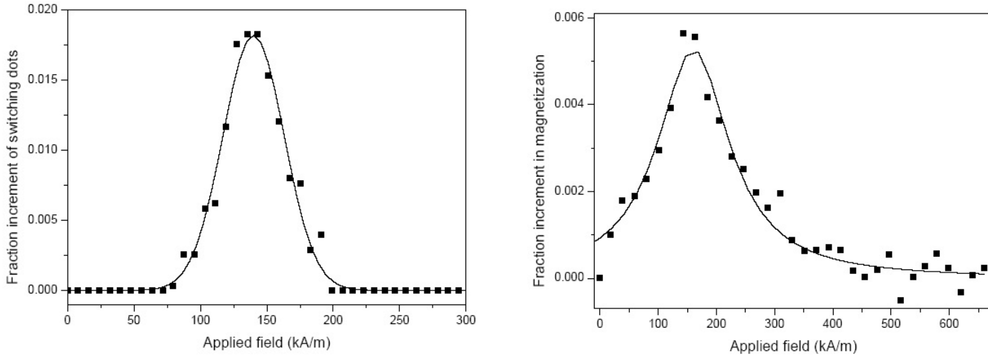

Figure 6.5: *Left: Histogram showing the fraction increment of the switched CoNi/Pt dots as measured by MFM after applying a new external field. Right: Histogram showing the fraction increment in magnetization as measured by VSM after applying a new external field*

Prior each MFM image an external magnetic field was applied. The field was increased to a certain value and then taken back to zero. All images were made over the same area of the sample covering a surface of about 5.5 $\times$ 5.5 μm^2, which contains a total of 365 dots. The first image in Figure 6.3 shows the magnetization after applying a field of -1353 kA/m perpendicular to the sample. The tip and the medium are saturated in the same direction so only attractive forces occur (black dots). When the field is increased to +4 kA/m, the tip reverses magnetization and all forces become repulsive, so the contrast reverses (white dots). At 127 kA/m almost 50% of the dots is reversed (Figure 6.3 c) and at 183 kA/m almost all dots are reversed (Figure 6.3 d). The first dots switch already at 80 kA/m, but the last at 192 kA/m. The graph on Figure 6.4 (left) was produced by counting the number of reversed dots on each MFM image after applying a certain field. On the vertical axis the fraction of the switched dots after applying a new field is shown.

Figure 6.4 (right) corresponds to an identical experiment performed by VSM (DCD curve) on the same sample. The MFM measurement shows a clear gradual reversal of the dots in between 80 and 192 kA/m. Outside this range all the imaged dots are magnetized either in the upwards or downwards direction. However, the VSM measurement shows a change in the sample magnetization in a much larger range (starting at negative switching fields and reaching equilibrium around 550 kA/m). It should be noted that the graph in Figure 6.4 (left) represents the reversal of 365 dots located on a very specific area of the sample surface, about $5.5 \times 5.5 \quad \mu m^2$. On the other hand, in the VSM experiment (Figure 6.4 (right)) the magnetization reversal of the whole sample (about

$5 \times 5 \quad mm$, containing around 2.8×10^8 dots) is measured, including magnetic material which could be redeposited during the IBE process.

Figures 6.5 (left and right) are histograms produced from the curves displayed in Figure 6.4. On the left, the fractional increment of switched dots after applying a new field is shown. On the right, the fractional increment in magnetization of the whole sample as measured by VSM is shown.

From figure 6.5 (left) it is possible to appreciate the dispersion in the switching field value of the dots, which matches with a Lorentzian distribution. The DCD curve of Figure 6.5 (right) shows a wider dispersion in the fitted Lorentzian curve than the MFM measurement. If the Switching Field Distribution (SFD) is defined as the dispersion of the fitted Lorentzian curve, then the SFD measured by VSM over the whole sample is 3 times larger than SFD measured by MFM over the dots. This could suggest that the mechanism that governs the dots switching is better represented by $n = 3/2$. However, even when the dots are single domain at remanence because of their perpendicular anisotropy, the switching process is not that of a coherent rotation. The size of the dots (90 nm diameter approx.) is not small enough to allow the them to behave as single domain particles.

Further thermal dependent measurements at lower temperatures are needed in order to better determine the coercive field H_0 and the reversal mechanisms. However, at the moment those temperatures are not achievable in our setup. Additionally, further research should include analytical models, which consider domain wall motion, pinning points, nucleation and the effects of rough edges and interfaces on the final anisotropy values.

6.3 Analysis of Co/Pt dots

In figure 6.6 six hysteresis loops are presented. They correspond to $Pt(40\AA)$ / $[Co(4\AA)$ / $Pt(10\AA)]$ $\times 5$ samples deposited on three different substrates: Silicon, silicon oxide 40 nm thick grown on silicon by thermal oxidation and silicon oxide 590 nm grown on silicon by the same method. The graphs on the left correspond to continuous films, while the graphs on the right correspond to the patterned films consisting of a squared arrays of nanodots with a periodicity of 300 nm. The hysteresis loops of the continuous films were already discussed in Chapter 4 and are here presented for comparison purposes with the patterned films. It is possible to observe from the graphs in figure 6.6 that the coercivity of the patterned samples has increased considerably if compared to the continuous films. It is remarkable that the coercivity of the continuous film deposited on silicon (around 10 kA/m) is the smallest of all but when it comes to the patterned films, the coercivity is the highest (260 kA/m). In the case of the film deposited on 40 nm thick silicon oxide the coercivity increases from 30 kA/m to 40 kA/m.

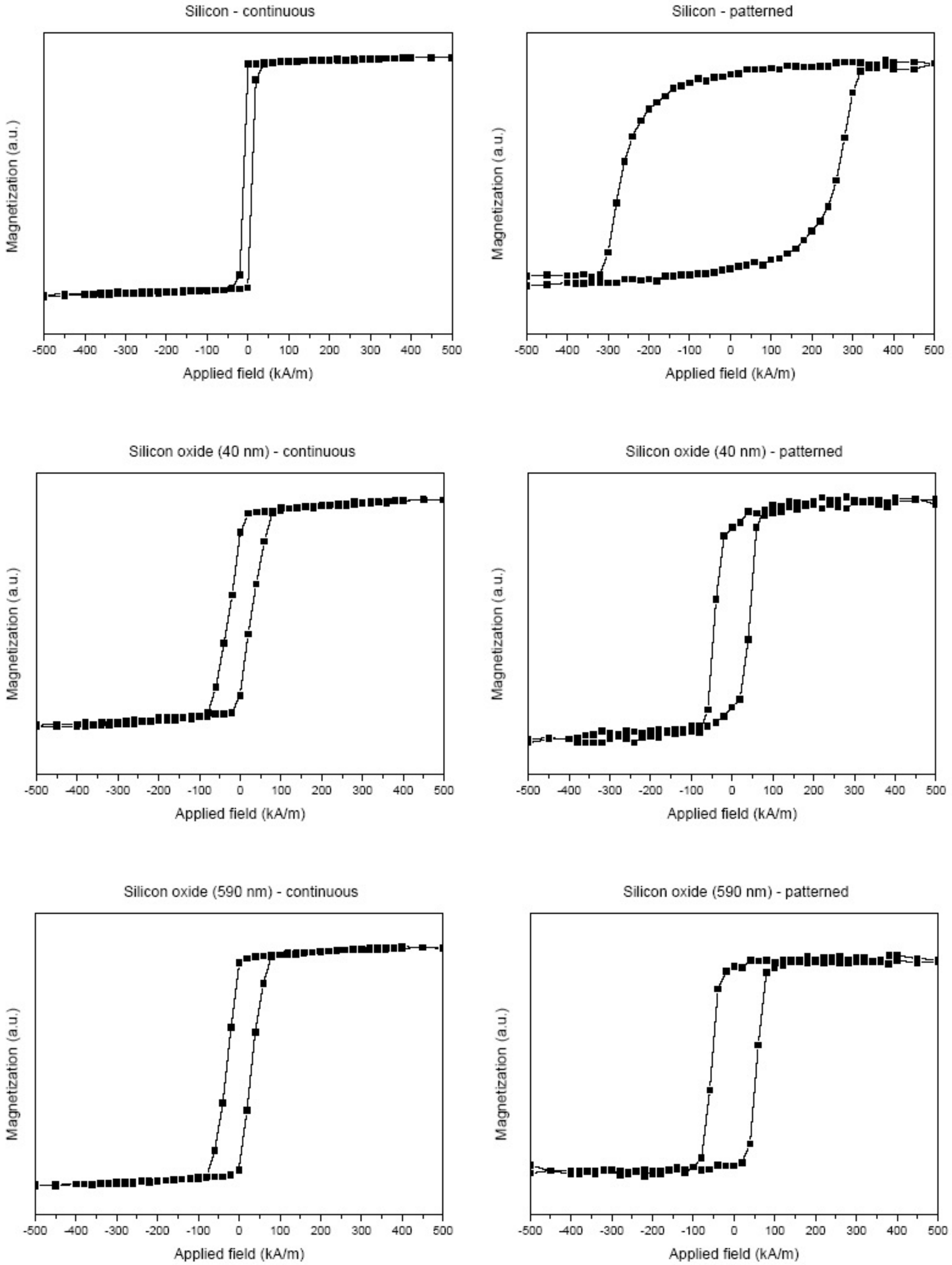

Figure 6.6: *Perpendicular VSM hysteresis loops of continuous (left) and patterned (right) Co/Pt multilayers deposited on different substrates. The patterned films corresponds to squared arrays of dots with periodicity of 300 nm and dot diameters of 90 nm.*

And in the case of the film deposited on 590 nm thick silicon oxide the coercivity increases from 30 kA/m to 60 kA/m.

In the case of the film deposited on Silicon, it is thought that the huge coercivity in the patterned film may be due to migration of Platinum and Cobalt into the Silicon structure. It is known that certain materials can be diffused into the crystal structure of Silicon when used as a substrate. Moreover, the migration process can be speeded up when heating the Silicon substrate. As a matter of fact, during the ion beam etching process, the wafer is heated. If migration occurs, this will induce defects in the lower bilayers of the film which will account as pinning points. Those pinning points could be responsible for the large coercivity that has been observed in the patterned film.

It should be noted that the magnetic multilayer thickness of Co/Pt dots is about 11 nm, while the multilayer thickness of the CoNi/Pt dots is about of 32 nm. For thinner structures the rate of redeposition during the ion beam etching process is lower due to a lower aspect-ratio. This may be the reason that the hysteresis loops of the three patterned films do not present a double-slope behaviour (as in the case of the patterned CoNi/Pt film).

6.3.1 Thermostability of Co/Pt dots

Using VSM, the hysteresis loops of the three Co/Pt patterned samples were measured at different temperatures, ranging from 150 to 475 K. Figure 6.7 displays the temperature dependence of the coercivity of the three patterned samples. As in the case of the analysis of the CoNi/Pt sample, the experimental data was fitted into three different expressions by using three different values of n. The resulting curves are also displayed in Figure 6.7. Table 6.2 shows the calculated values for H_0, U and V_s corresponding to the fitted curves. The energy barrier U, ranges from 2.45×10^{-19} to 3.13×10^{-19} J (1.53 - 1.95 eV) in the case of the sample deposited on Silicon. This corresponds to a $\Delta E/KT$ ratio from 59.0 to 75.6 . For the sample deposited on the 40 nm thick Silicon Oxide substrate it was found that U 1.54×10^{-19} - 1.63×10^{-19} J (1.53 - 1.95 eV) ($\Delta E/KT$ 37.2 - 39.3) and in the case of the sample deposited on the 590 nm thick Silicon Oxide it was found that U 1.53×10^{-19} - 1.62×10^{-19} J (0.96 - 1.01 eV) ($\Delta E/KT$ 37.0 - 39.1). The switching volume V_s was obtained from the calculated value for U and the estimated effective perpendicular anisotropy of the films ($U = K_{eff}V_s$). The effective perpendicular anisotropy was estimated by comparing the perpendicular and in-plane VSM hysteresis loops of the samples: $550 kJ/m^3$ in the case of the sample deposited on Silicon and $253 kJ/m^3$ in the case of the samples deposited on Silicon oxide.

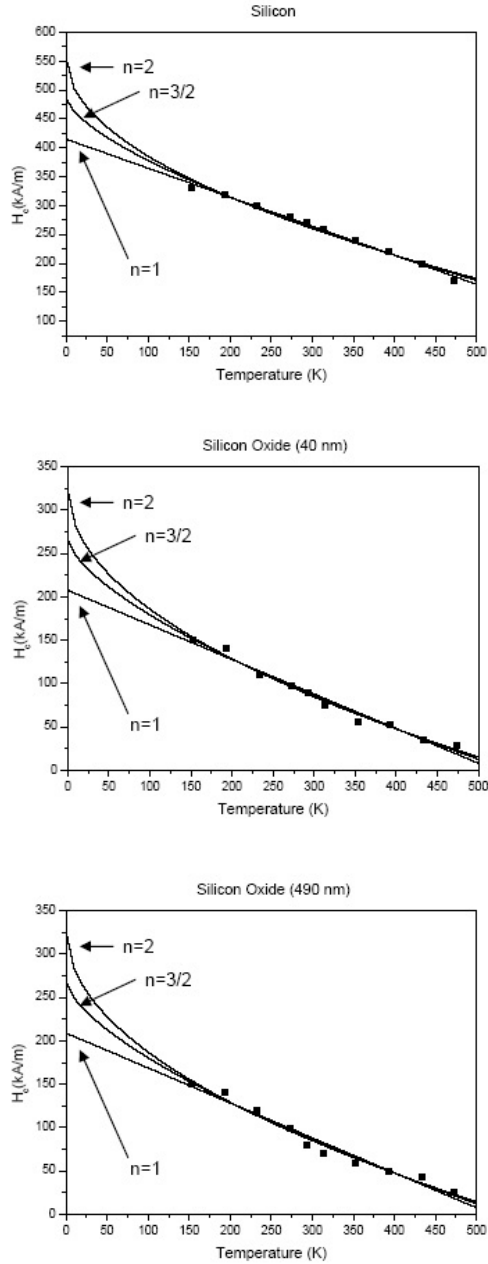

Figure 6.7: *Temperature dependence of the coercivity for the Pt/[Co / Pt]×5 patterned samples. Three different fittings for the experimental data are shown, by using different values of n.*

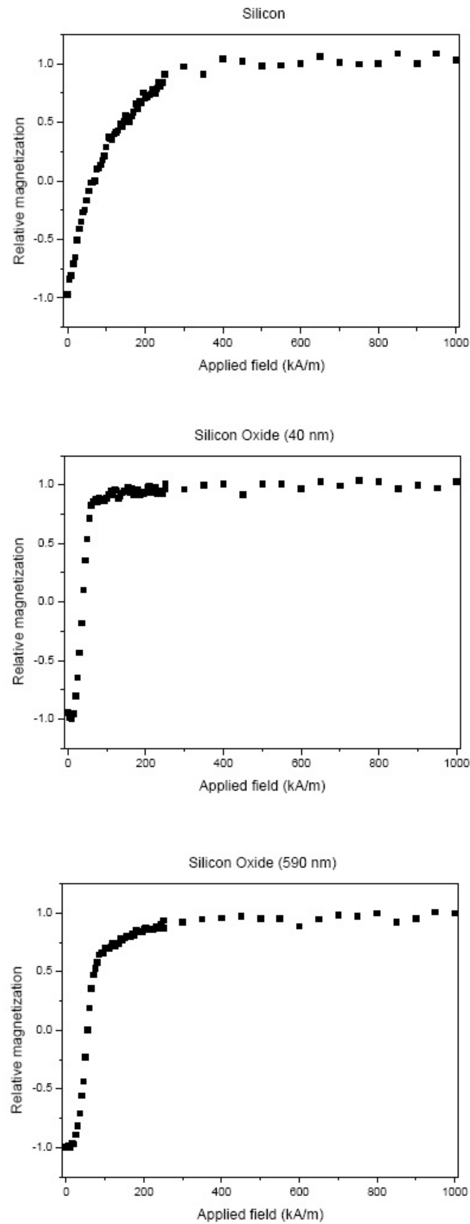

Figure 6.8: *Remanence curves of the three Co/Pt samples as measured by VSM*

Silicon			
Value of n	H_0 (kA/m)	$U(J)$	$V_s(nm^3)$
1	415.0	2.45×10^{-19}	4.5×10^2
3/2	485.9	2.83×10^{-19}	5.2×10^2
2	556.6	3.13×10^{-19}	5.7×10^3
Silicon oxide (40 nm)			
Value of n	H_0 (kA/m)	$U(J)$	$V_s(nm^3)$
1	207.5	1.54×10^{-19}	6.1×10^2
3/2	265.7	1.59×10^{-19}	6.3×10^2
2	323.6	1.63×10^{-19}	6.4×10^3
Silicon oxide (590 nm)			
Value of n	H_0 (kA/m)	$U(J)$	$V_s(nm^3)$
1	209.0	1.53×10^{-19}	6.1×10^2
3/2	268.0	1.58×10^{-19}	6.3×10^2
2	326.6	1.62×10^{-19}	6.4×10^3

Table 6.2: *Estimated values for the switching field (H_0), energy barrier (U) and switching volume at zero temperature (V_s) for the different values n (1, 3/2, 2) for the three Co/Pt samples.*

6.3.2 Remanence and switching field distribution of Co/Pt dots

DCD remanent curves of the three Co/Pt samples were produced by VSM measurements. The obtained data are plotted in Figure 6.8. Histograms have been produced from the data obtained by the remanent measurements (Figure 6.9). Lorentizan curves fitted into the plots are also displayed. The two graphs on the top of Figure 6.9 correspond to the same measurement of the sample deposited on Silicon. However, on the first graph (top left), a fit is shown to a simple Lorentzian distribution, while the second graph displays a curve corresponding to the combination of two Lorentzian distributions. As can bee seen, this second curve fits better with the experimental data. It seems as if there are two kinds of magnetic materials combined into the sample deposited on Silicon. This could be caused because of heating of the substrate during the IBE process which could facilitate diffusion of some of the magnetic material into the Silicon. However, one should also considered the possibility that the smaller Lorentzian curve is just an artifact resulting from noise during the data acquisition. In any case, it can be observed that the sample deposited on top of Silicon presents a large switching field distribution, about three times larger than the two other samples deposited on Silicon Oxide.

At the bottom of Figure 6.8 two graphs are shown, corresponding to the remanent VSM measurements of the sample deposited on 40 nm thick Silicon Oxide (bottom left) and the sample deposited on 590 nm thick Silicon Oxide

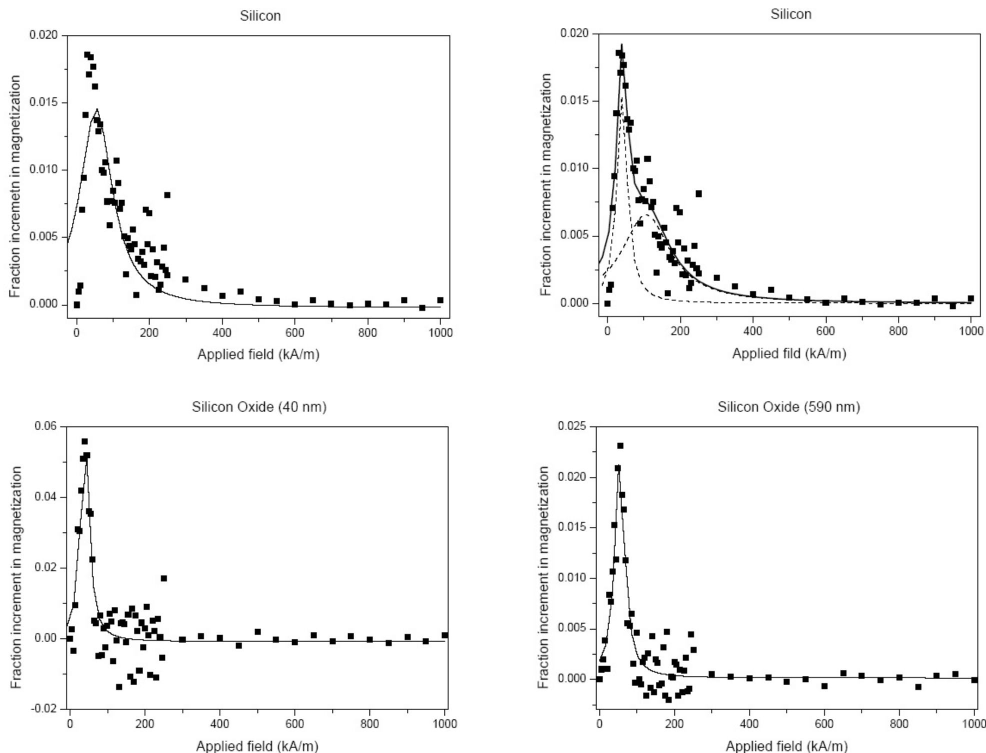

Figure 6.9: *Histograms showing the fraction increment in magnetization as measured by VSM after applying a new external field. Lorentzian curves have been fitted into the plotted data.*

(bottom right). Lorentzian curves are plotted along the experimental data. From the fitted curves it can be concluded that the switching field distribution of these two samples follows a Lorentizan distribution.

6.4 Conclusions

A model for coercivity for a magnetic patterned medium has been presented. This model is based on the equation describing the energy barrier for a group of weakly interacting particles and the Arrhenius relation. CoNi/Pt and Co/Pt multilayered samples were investigated and analysed by performing thermal dependent VSM measurements and by using the coercivity model.

In the case of the CoNi/Pt sample, the measurements done by VSM showed a larger switching field distribution than those done by field dependent MFM. This is due to the fact that the MFM measurement was done on a very localized

area of the sample, while the measurement done by VSM was an evaluation all over the sample covering all the dots present in the medium. It is possible that the dots are not uniform all over the sample's surface. So, the switching field distribution becomes larger when evaluating areas containing large number of dots. Another circumstance that should be taken into account is the fact that our MFM measurements are only sensitive to the perpendicular magnetization component of the dots. In other words, our MFM setup only senses dots magnetized either in the upward or downward direction. Because of this fact, redeposited material can be easily ignored by the MFM measurements, and of course dots outside the studied area ($5 \times 5\mu m$) are ignored. Specially dots located on the edges of the sample could be easily damaged due to the fact that the sample is cut in order to fit the sample holder's dimensions. Also, during the handling of the sample (mainly with tweezers) the dots on the edges may become damaged.

In the case of the three Co/Pt samples, a large difference in between the sample deposited on Silicon and the samples deposited on Silicon Oxide was observed. When analysing the continuous films, the sample deposited on Silicon showed a steep hysteresis loop with a sharp magnetization-direction transition. The other two samples showed a more gradual transition and their hysteresis loops were very similar to each other. However, after the samples were patterned, it was found that the hysteresis loop of the sample deposited on Silicon had a coercivity three times larger than the other two samples. Nevertheless, its hysteresis loop had a softer slope than the other two samples. When performing the remanence measurements the switching field distribution of the sample deposited on Silicon resulted to be the largest. Histograms were derived from the remanence measurements. Lorentzian dispersion curves were fitted to the data obtained from those histograms. However, in the case of the sample deposited on Silicon the fitting was poor. The fitting became more much better when including two Lorentzian curves in the fitting. Thus, the final fitting for the sample deposited on Silicon was a curve which was the addition of two Lorentizian dispersions. The fact that two Lorentzians curves are needed to produce a good fitting may indicate the presence of two kinds of magnetic materials within the sample. As indicated in Chapter 4, Silicon had the lowest roughness from the used substrates. However, the lack of a Silicon Oxide layer on top of the Silicon substrate allows for Platinum and Cobalt migration into the Silicon lattice. As a consequence, the Co/Pt interfaces may become less sharp due to the migration problem. Additionally, the migration of material into the Silicon can be favoured due to heating of the substrate during the Ion Beam Etching patterning process. In the case that the heating of the wafer is non uniform, the magnetic properties of the resulting dots will present a larger distribution than the one expected for the samples deposited on Silicon Oxide. One should take into account that the second peak observed in the fitted distribution curve may be an artifact created by noise in the measurements. In the case of the other two samples (those de-

posited on Silicon Oxide) the fittings were made by using only one Lorentzian curve. Both fitted curves showed similar results. This is in agreement with the fact that the roughness of the Silicon Oxide substrates used for these samples (40 and 590 nm thick) were not too different, as mentioned in Chapter 4,

As to the VSM thermal dependent measurements, it was found that the CoNi/Pt sample presented an internal energy (U) around $1.87 \times 10^{-19}$to $2.06 \times 10^{-19} J$ and its switching volume was about $1.3 \times 10^{3} nm^{3}$. In the case of Co/Pt the sample deposited on Silicon had an internal energy about 2.45×10^{-19} to $3.13 \times 10^{-19} J$. When compared with the other two Co/Pt samples deposited on Silicon Oxide, it is found that their thermostability is poorer.

In conclusion, the Co/Pt sample deposited on Silicon shows a larger switching field distribution and a coercivity three times higher than the other two Co/Pt samples and its thermostability is larger as well. Growing smoother Silicon Oxide substrates could help to fabricate magnetic dots with higher coercivity, thermostability, enhance perpendicular anisotropy. In the other hand material migration would be avoided and with this a large switching field distribution would be prevented.

Chapter 7

Conclusions

In this chapter the conclusions are summarized from two different views. One is about boundary conditions for designing a patterned media and the other is about the preparation and lithographic processes necessary to fabricate patterned media. At the end, some recommendations for future research are given.

7.1 Minimum requirements for magnetic patterned media

Different parameters have been estimated for designing a patterned medium. In the coming paragraphs those parameters will be discussed. The estimated values should be regarded as the minimum requirements that should be fulfilled in order to consider a magnetic patterned film used as a potential candidate for high-density magnetic recording applications.

7.1.1 Minimum energy-barrier for an idealized pattern media

Stored information is subject to thermal degradation. For information to be stable over long periods of time, a high energy barrier is needed between the recorded states ("up" and "down" in perpendicular magnetic recording). Charap [39] calculated that in the case of a continuous (granular) medium for hard disk recording, a minimum energy-barrier of 40.27 kT is required, which corresponds to a relaxation time of the magnetic information of 10 years.

To estimate the energy barrier for patterned media, we assumed an idealized patterned media consisting of identical Stoner-Wohlfarth particles. From this simple model it can be concluded that the energy-barrier should be at least **48.8** kT in order to achieve a raw bit error rate (BER) of 10^{-4} after 5 years, which corresponds to a relaxation time (τ) of 5×10^4 years. So, even in the idealized case, patterned media require a much higher $\Delta E/KT$ value than continuous

granular films. The reason for this is that reversal of a few grains in an assembly of grains composing bit in a continuous medium is acceptable. Accidental reversal of the magnetisation in an element of a patterned medium however will immediately result in a bit error.

7.1.2 Maximum areal bit density

According to our model, for a given dot-aspect-ratio the highest achievable bit-density is restricted by the magnetization saturation of the dots. In the case of an aspect ratio of 1/10 (which is close to the disk shape dots of the samples studied in this work) the maximum bit density for Co/Pt dots lies around 0.4 Tbit/sqi. This density is an upper limit, in a non-idealized sample the maximum areal-bit-density will be lower.

The model predicts that for the material with the highest energy density known today (FePt $L1_0$), the maximum bit density lies around **7 Tbit/sqi**. This value is achieved for dots with an aspect ratio of 1, for lower bit aspect ratios the maximum bit density will be lower.

7.1.3 Minimum switching field distribution in an idealized pattern medium

The idealized medium that we have considered will posses a switching field distribution (SFD)since for each dot the energy barrier depends on the magnetization state of its neighbours due to magnetostatic interactions. It has been estimated that in the case of Co/Pt multilayered dots with an aspect ratio of (b = 1/4) the theoretical switching fields range from 857 to 871 kA/m, so the minimum theoretical SFD is about 14 kA/m or 2%. Inhomogeneities or defects within the dots are not considered in our model and they will strongly increase the switching field values.

7.1.4 Boundaries for an auxiliary writing field

In order to change the magnetization state of a dot it was proposed to place a magnetic probe in contact with the addressed dot. However, it has been concluded that disregarding of the magnetic probe an auxiliary magnetic field will be necessary to assist the probe field. The field from the probe should exceed the swithing field distribution of the medium. After taking into consideration the inherent switching field distribution of our material (Co/Pt dots), it has been predicted that in the case of a probe made of pure Cobalt with a diameter equal to that of the dots an auxiliary field in between 333 and 857 kA/m will be required. In a realistic patterned medium, the permitted auxiliary field values

will be lower due to the larger switching field distributions that are expected. Therefore the field from the probe can be higher.

7.2 Fabrication techniques

A method for fabricating arrays of magnetic particles was improved. The method is based on sputtering a thin film, laser interference lithography and ion beam etching. That technique allows the fabrication of arrays of identical structures with elliptical, square and circular shapes, depending on the steps and parameters involved during the laser exposure and development. Square, hexagonal and other types of particle packaging are allowed. In the same way, it is possible to prepare two-dimensional arrays with two different periodicities in each one of their leading axes.

Because the characteristics of the laser interference lithography setup that has been used, it was possible to produce uniform patterns over quite large areas, compared to other techniques such as e-beam lithography. The area of quasi-uniform laser exposure ranges from 1 to 5 squared centimeters depending on the periodicity (pitch) of the produced structures. The time that is required for making a sample is also relatively short in comparison with other techniques (less than one minute).

The dimension of the patterns that were produced as part of this research project by the laser interference technique are very diverse: From 1 μm of periodicity down to 150 nm. The diameters of the produced magnetic dots range from 300 nm to 50 nm depending on the chosen periodicity and exposure time. However, the work here presented is focused in the fabrication and magnetic analysis of magnetic periodic structures with 300 nm of periodicity (and diameters about 90 nm), because this was the smallest arrays in which we could achieve good reproducibility.

Because of the large patterned areas on the samples, it is possible to conduct magnetic macroscopic measurements of the collective behaviour of the elements. This is done by VSM, Kerr magnetometry and AHE measurements, while MFM allowed for studying single dots. Those tools were used used to characterize the samples and determine relevant parameters such as coercivity, remanent magnetization, thermal stability and switching field distribution.

7.2.1 Substrate roughness effect in the continuous films

It has been found that Silicon wafers with its layer of native oxide removed present a low surface roughness of 0.2 nm, which favours the growth of smooth sputtered layers. In the case of the sputtered CoNi/Pt samples it was observed that their coercivity decreases as the substrates become smoother. This could be

explained by the fact that rougher substrates favour the formation of more defects in the films, which hampers domain propagation. However, it should also be considered that the growth of the Pt seed layer on bare Si might differ from the growth on SiO_x. In fact, formation of platinum silicide has been reported when depositing Pt directly on bare Si. Platinum silicide has influence in the growth of the subsequent deposited layers [104, 105, 106].

7.2.2 Number of bilayers effect in the continuous films

In the case of the (Co/Pt) $timesn$ multilayers, it was observed that the nucleation field and coercivity increases as the number of bilayers increases. This might be due to the larger amount of defects present in the thicker samples. As the number of bilayers was increased the squareness of the measured hysteresis loops was lost.

7.2.3 Photoresist stacks and vertical standing waves

As part of the fabrication experiments two kinds of photoresist were explored, one positive resist and one image reversal resist. Three different etch masking systems were studied, a simple etching mask compound only by the patterned photoresist coating, a trilevel stack using a bottom antireflection coating, and a hardmask approach in combination with the image reversal photoresist. From the three masking systems, the one comprising just the patterning photoresist was found to be the most convenient in day-to-day use. It consisted of a thin coating of diluted positive photoresist. The problem of vertical standing waves was addressed by using a high exposuse dose (supra-exposure scheme). It was found that by increasing the exposure dose and using a highly reflective mirror to achieve good contrast, it is possible to control the size of the photoresist dots and to diminish the presence of photoresist terraces or plateaus interconnecting the photoresist dots due to the effect of vertical standing waves.

7.3 Limitations of the fabrication techniques

In this section we discuss the limitations of the fabrication techniques that were used for the realization of our samples, and suggestions for improvement in further stages of the research on magnetic patterned media.

7.3.1 Laser interference technique

The lowest achievable pitch is limited by half the wavelength of the laser (λ=266 nm) which means that the minimum spacing between dot and dot could be in

ideal conditions 133 nm. [1], which can be translated into a maximum areal density of 36 $Gbit/in^2$. Lasers with lower wavelengths lack acceptable temporal stability and spacial coherence, which makes them difficult to use for LIL. Systems using diffraction gratings instead of a Lloyd's mirror or even the use of X-ray coherent sources (e.g. synchrotron sources) in combination with special design resists seems to be an alternative. Besides that, the use of high diffraction index media can help to decrease the periodicity of the LIL patterns.

7.3.2 Photoresist

Besides the limitations regarding the LIL technique, also the photoresist (diluted Olin 907) used to fabricate the magnetic samples is not suitable to attain the density at which patterned media will be introduced in industry. The Olin photoresist was not originally designed to work at a wavelength of 266 nm nor to produce submicron structures. Several experiments have demonstrated that the highest contrast resolution of the photoresist has a treshold around a feature size of 50 nm.

Impurities and polymeric chains aggregation (clustering) are present in the photoresist even after filtering. These results in non-uniform resist and subsequent irregularities in the photoresist dot shape. Those irregularities in shape are transferred to the final magnetic dots during the Ion Beam Etching process.

7.3.3 Ion beam etching technique

The Argon Beam Etching technique lacks selectivity, produces redeposition, heats the sample and damages the interlayer interfaces.

Heating and material redeposition are responsible for the difficulties in removal of the photoresist. It is known that heating produces cross-linking in novolak based resins[90].

Besides that, the ion bombardment penetrates through the interlayers and causes interfaces mixing. As a consequence, the effective perpendicular anisotropy is reduced which results in inferior quality recording media.

7.4 Coercivity, switching field distribution and writability

It was observed that the coercivity of the CoNi/Pt continuous films increased as the substrate roughness increased. A similar trend was found on the Co/Pt continuous films.

[1] In order to achieve the 1 Tb/in^2 goal it is necessary a pitch of 25 nm.

Substrate	H_c (kA/m)	SFD (kA/m)	R_{SFD}
Si	260	91	0.35
SiO_x (40 nm)	40	44	1.10
SiO_x (590 nm)	60	51	0.85

Table 7.1: *Values for the coercivity (H_c) as measured by VSM, switching field distribution (SFD) and relative switching field distribution (R_{SFD}) of the three kind of patterned Co/Pt samples analysed in this thesis.*

The differences in the coercivity and other magnetic parameters between the patterned sample deposited on the 40 nm thick Silicon Oxide and the patterned film deposited on the 590 nm thick Silicon Oxide are noticeable but small, which suggests that the influence of the IBE beam etching on the magnetic properties of the films is more much important than the influence of the substrate roughness. However, in the case of the patterned film deposited on Silicon the coercivity was about 5 times larger than in the other patterned samples, presumably because the formation of platinum silicide at the seed layer.

VSM measurements have shown, as stated in the previous chapter, that the SFD distribution of the two Co/Pt patterned samples deposited on Silicon Oxide is about two times smaller than the patterned sample deposited on Silicon. However when looking for suitable recording media the relative SFD distribution becomes the relevant parameter, which is defined as

$$R_{SFD} = \frac{H_c}{SFD}, \tag{7.1}$$

where H_c is the measured coercivity of the whole array of dots. This information is summarized in table 7.1.

The fact that the relative SFD in the case of the patterned sample on Silicon is lower than the other two samples means that this sample is more suitable for writing experiments than the other two.

7.5 Recommendations

It is thought that grain boundaries, interface irregularities within the dots and IBE damage are the main cause for the large switching field distribution which has been observed in the samples. Decreasing sputtering pressure and using smoother substrates might help to improve the regularity of the deposited films. However, grain boundaries always will be present when using magnetron sputtering. One alternative is the use of single crystalline, epitaxially grown magnetic materials.

The relative switching field distribution of the samples deposited on Si in this work seems to be in the right order of magnitude. If the coercivity can lowered while keeping the same relative switching field distribution, the range of switching fields will decrease and field-only writing might be simpler.

Alternative high contrast photoresists with higher resolutions should be explored. Since writing is seriously affected by remains of photoresist, alternate patterning processes avoiding ion beam etching and subsequent redeposition need to be investigated. Solutions could for instance be found in lift-off techniques, deposition on templates [107]or using hard masks.

A plausible alternative seems to be the use of self assembled structures as an etching mask. Submicron structures could be produced by LIL which would serve as a template to guide the self assembling process [108]. By using that, the 1 Tb/in^2 goal might be achievable.

Bibliography

[1] O. Smith. *The electrical world* (8 September 1888). 1.1.1

[2] V. Poulsen. “The telegraphone: A magnetic speech recorder”. *The Electrician* **46**, 208 (1900). 1.1.1

[3] V. Poulsen. “Das Telegraphone”. *Annalen der Physik* **3**, 754 (1900). 1.1.1

[4] M. Clark and H. Nielsen. “Crossed wires and missing connections: Valdemar Poulsen, the American Telephone Company and the failure to commercialise magnetic recording”. *Business History Review* **69**, 41 (1995). 1.1.1

[5] E. D. Daniel (Editor), C. D. Mee (Editor) and M. H. Clark (Editor). “Magnetic Recording: The First 100 Years”. IEEE (1999). 1.1.1

[6] Steven Schoenherr. “The History of Magnetic Recording” (2002). http://history.sandiego.edu/gen/recording/magnetic4.html (Online accessed 10-November-2005). 1.1.1, 1.1.2

[7] R. Rojas (editor). “Encyclopedia of computers and computer history”. Fitzroy Dearborn (2001). 1.1.2

[8] A. Hozoi. “Edge effects and submicron tracks in magnetic tape recording”. PhD. Thesis, University of Twente, The Netherlands (2005). 1.1.2

[9] T. Noyes and W. E. Dickinson. “The random-access memory accounting machine - II. The magnetic-disk, random-access memory (Reprinted from IBM Journal of Research and Development, vol 1, 1957)”. *IBM Journal of Research and Development* **44**, 16–19 (2000). 1.1.2

[10] “Seagate Technology Company Milestones” (2005). http://www.seagate.com/newsinfo/about/milestones/ (Online; accessed 11-November-2005). 1.1.3

[11] “IBM archive: 20th century disk storage chronology” (2005). http://www-03.ibm.com/ibm/history/exhibits/storage/storage_chrono20.html (Online accessed 11-November-2005). 1.1.3

[12] D. Jiles. “Introduction to magnetism and magnetic materials”. Chapman - Hall (1995). 1.2.1

[13] R. Waser (editor). "Nanoelectronics and Information Technology". Wiley-VCH (2005). 1.2.2, 1.2.3

[14] M. Mallary, A. Torabi and M. Benakli. "One terabit per square inch perpendicular recording conceptual design". *IEEE Trans. Magn.* **38**, 1719–1724 (2002). 1.2.2

[15] R. L. White, R.M.H. Newt and R.F.W. Pease. "Patterned media: a viable route to 50 Gbit/in^2 and up for magnetic recording?". *IEEE Trans. Magn.* **33**, 990 (1997). 1.2.3

[16] M. Todorovic, S. Schultz, J. Wong and A. Scherer. "Writing and reading of single magnetic domain per bit perpendicular patterned media". *Appl. Phys. Lett.* **74**, 2516 (1997). 1.2.3

[17] C. Chappert, H. Bernas, J. Ferré, V. Kottler, J.-P. Jamet, Y. Chen, E. Cambril, T. Devolder, F. Rousseaux, V. Mathet and H. Launois. "Planar Patterned Magnetic Media Obtained by Ion Irradiation". *Science* **280**, 1919 (1998). 1.2.3, 1.3.1

[18] L. Guan and J.-G. Zhu. "Investigation of patterned thin film media for ultra-high density". *IEEE Trans. Magn.* **36**, 2297–2299 (2000). 1.2.3

[19] M. Albrecht, C. T. Rettner, A. Moser, M. E. Best and B. D. Terris. "Recording performance of high-density patterned perpendicular magnetic media". *Appl. Phys. Lett.* **81**, 2875–2877 (2002). 1.2.3

[20] M. Albrecht, A. Moser, C. T. Rettner, S. Anders, T. Thomson and B. D. Terris. "Writing of high-density patterned perpendicular media with a conventional longitudinal recording head". *Appl. Phys. Lett.* **80**, 3409–3411 (2002). 1.2.3

[21] J.P. Wang and T.J. Zhou. "Patterned Magnetic Nanostructures". *Encyclopedia of Nanoscience and Nanotechnology, H. S. Nalwa editor* **Vol. 8**, 415–433, American Scientific Publishers (2004). 1.3

[22] J.I. Martín, J. Nogués, Kai Liu, J.L. Vicent and Ivan K. Schuller. "Ordered magnetic nanostructures: fabrication and properties". *J. Magn. Magn. Mater.* **256**, 449501 (2003). 1.3

[23] J. C. Lodder. "Methods for preparing patterned media for high-density recording". *J. Magn. Magn. Mater.* **272-276**, 1692–1697 (2004). 1.3, 2.1, 2.8.2, 3

[24] J. C. Lodder. "Patterned Nanomagnetic Films". *Advanced Magnetic Nanostructures, Eds. D. Sellmyer and R. Skomski* pages 261–288, Springer Science & Business Media, Inc. New York, USA (2006). 1.3

[25] P. F. Carcia, S. I. Shah and W. B. Zeper. "Effect of energetic bombardment on the magnetic coercivity of sputtered Pt/Co thin-film multilayers". *Appl. Phys. Lett.* **56**, 2345–2347 (1990). 1.3.1

[26] J. Ferr, C. Chappert, H. Bernas, J. P. Jamet, P. Meyer, O. Kaitasov, S. Lemerle, V. Mathet, F. Rousseaux and H. Launois. "Irradiation induced effects on magnetic properties of Pt/Co/Pt ultrathin films". *J. Magn. Magn. Mater.* **198–199**, 191–193 (1999). 1.3.1

[27] A. Dietzel, R. Berger, H. Grimm, W.H. Bruenger, C. Dzionk, F. Letzkus, R. Springer, H. Loeschner, E. Platzgummer, G. Stengl, Z.Z. Bandic and B.D. Terris. “Ion projection direct structuring for patterning of magnetic media”. *IEEE Trans. Magn.* **38**, 1952–1954 (2002). 1.3.1

[28] T. Aign, P. Meyer, S. Lemerle, J. P. Jamet, J. Ferré, V. Mathet, C. Chappert, J. Gierak, C. Vieu, F. Rousseaux, H. Launois and H. Bernas. “Magnetization Reversal in Arrays of Perpendicularly Magnetized Ultrathin Dots Coupled by Dipolar Interaction”. *Phys. Rev. Lett.* **81**, 5656–5659 (1998). 1.3.1

[29] C. T. Rettner, M. E. Best and B. D. Terris. “Patterning of Granular Magnetic Media with a Focused Ion Beam to Produce Single-Domain Islands at ¿140 Gbit/in^2”. *IEEE Trans. Magn.* **37**, 1649 (2001). 1.3.1

[30] G. M. McClelland, M. W. Hart, C. T. Rettner, M. E. Best, K. R. Carter and B. D. Terris. “Nanoscale patterning of magnetic islands by imprint lithography using a flexible mold”. *Appl. Phys. Lett.* **81**, 1483–1485 (2002). 1.3.2

[31] F. Carcenac, C. Vieu, A. Lebiband Y. Chen, L. Manin-Ferlazzo and H. Launois. “Fabrication of high density nanostructures gratings (¿500Gbit/in^2) used as molds for nanoimprint lithography”. *Micr. Eng.* **53**, 163–1664 (2000). 1.3.2

[32] J. Moritz, B. Dieny, J. P. Nozires, S. Landis, A. Lebib and Y. Chen. “Domain structure in magnetic dots prepared by nanoimprint and e-beam lithography”. *J. Appl. Phys.* **91**, 7314–7316 (2002). 1.2, 1.3.3

[33] K. Naito, H. Hieda, M. Sakurai, Y. Kamata and K. Asakawa. “2.5-Inch Disk Patterned Media Prepared by an Artificially Assisted Self-Assembling Method”. *IEEE Trans. Magn.* **38**, 1949 (2002). 1.3.4

[34] S. Sun, C. B. Murray, D. Weller, L. Folks and A. Moser. *Science* **287**, 1989 (2000). 1.3.4

[35] V. Skumryev, S. Stoyanov, Y. Zhang, G. Hadjipanayis, D. Givord and J. Nogués. “Beating the superparamagnetic limit with exchange bias”. *Nature* **423**, 850–853 (2003). 2.1

[36] W. F. Brown. “Thermal fluctuations of a single-domain particle”. *Phys. Rev.* **130**, 1677–1686 (1963). 2.2.2, 6.1

[37] M. P. Sharrock. “Time dependence of switching fields in magnetic recording media”. *J. Appl. Phys.* **76**, 6413–6418 (1994). 2.2.2, 2.4, 6.1

[38] Y. Hao, C. A. Ross and H. I. Smith. “Thermal stability of the magnetization of 150 nm$\times$230 nm $Ni_{19}Fe_{81}$ elements”. *J. Appl. Phys.* **93**, 7909–7911 (2003). 2.2.2, 6.1

[39] S. H. Charap, P. L. Lu and Y. He. “Thermal stability of recorded information at high densities”. *IEEE Trans. Magn.* **33**, 978–983 (1997). 2.2.3, 2.10, 7.1.1

[40] R. K. Wangsness. “Electromagnetic Fields”. Wiley (1986). 2.5

[41] M. A. M. Haast. "Patterned magnetic thin films for ultra high density recording". PhD. Thesis, University of Twente, Enschede, The Netherlands (1999). *a*, *d*, 4.1, 4.4

[42] M. Mansipur. "The physical principles of magneto-optical recording". Cambridge University Press (1995). *b*

[43] A. Lisfi and J. C. Lodder. "Magnetic domains in epitaxial $BaFe_{12}O_{19}$ thin films with perpendicular anisotropy". *J. Phys.: Condens. Matter* **14**, 12339–12352 (2002). *c*

[44] S. D. Willoughby, J. M. MacLaren, T. Ohkubo, S. Jeong, M. McHenry, D. E. Laughlin, S. J. Choi and S. J. Kwon. "Electronic, magnetic, and structural properties of $L1_0FePt_xPd_{1-x}$ alloys". *J. Appl. Phys.* **91**, 8822–8824 (2002). *e*, *g*

[45] Q. Meng, P. Han, W. P. Drent, J. C. Lodder and Th. J. A. Popma. "Effects of Pt seed layer and Ar pressure on magnetic and structural properties of sputtered CoNi/Pt multilayers". *IEEE Trans. Magn.* **32**, 4064–4066 (1996). *f*, 4.1, 4.4, 4.6.2, 6.2.1

[46] J. G. Zhu. "New heights for hard disk drives". *Materials Today* **6**, 22–31 (2003). 2.8.2

[47] T. A. Savas, M. L. Schattenburg, J. M. Carter and H. I. Smitha. "Large-area achromatic interferometric lithography for 100 nm period gratings and grids". *J. Vac. Sci. Technol. B* **14**, 4167–4170 (1996). 3, 5.3.1

[48] K. Nagai K. Utaka T. Ohira, T. Segawa and M. Nakao. "Large Area InP Submicron Two-Dimensional (2D) Periodic Structures Fabricated by Two-Time Laser Holography". *Jpn. J. Appl. Phys.* **41**, 1085–1089 (2002). 3

[49] M. Farhoud, J. Ferrera, A. J. Lochtefeld, T. E. Murphy, M. L. Schattenburg, J. Carter, C. A. Ross and H. I. Smith. "Fabrication of 200 nm period nanomagnet arrays using interference lithography and a negative resist". *J. Vac. Sci. Technol. B* **17**, 3182–3185 (1999). 3, 3.1

[50] J. Y. Decker, A. Fernandez and D. W. Sweeney. "Generation of subquarter-micron resist structures using optical interference lithography and image reversal". *J. Vac. Sci. Technol. B* 15. 3, 5.6, 5.15

[51] L. F. Johnson, G. W. Kammlott and K. A. Ingersoll. "Generation of periodic surface corrugations". *Appl. Opt.* **17**, 1165–1181 (1978). 3

[52] E. H. Anderson, C. M. Horwitz and H. I. Smith. "Holographic lithography with thick photoresist". *Appl. Phys. Lett.* **43**, 874–875 (1983). 3

[53] A. Fernandez, H. T. Nguyen, J. A. Britten, R. D. Boyd, M. D. Perry and D. R. Kania. "Use of interference lithography to pattern arrays of submicron resist structures for field emission flat panel displays". *J. Vac. Sci. Technol. B*. 3, 5.3.1

[54] R. C. Enger and S. K. Case. "Optical elements with ultrahigh spatial-frequency surface corrugations". *Appl. Opt.* **22**, 3220–3228 (1983). 3

[55] V. Berger, O. Gauthier-Lafaye and E. Costard. "Fabrication of a 2d photonic bandgap by a holographic method". *Electron. Lett.* **33**, 425–426 (1997). 3, 3.3.4

[56] C. J. M. van Rijn, W. Nijdam, S. Kuiper, G. J. Veldhuis, H.A.G.M. van. H.A.G.M. van Wolferen and M. C. Elwenspoek. "Microsieves made with laser interference lithography for micro filtration applications". pages 100–103 (1998). 3

[57] W. Wu, B. Cui, X. Sun, W. Zhang, L. Zhuang, L. Kong and S. Y. Chou. "Large area high density quantized magnetic disks fabricated using nanoimprint lithography". *J. Vac. Sci. Technol. B* **16**, 3825–3829 (1998). 3

[58] M. L. Schattenburg, C. R. Canizares, D. Dewey, K. A. Flanagan, M. Hamnett, A. M. Levine, K. S. K. Lum, R. Manikkalingam, T. H. Markert and H. I. Smith. "Transmission grating spectroscopy and the Advanced X-ray Astrophysics Facility (AXAF)". *Opt. Eng.* **30**, 1590–1600 (1991). 3

[59] A. Fernandez, P. J. Bedrossian, S. L. Baker, S. P. Vernon and D. R. Kania. "Magnetic force microscopy of single-domain cobalt dots patterned using interference lithography". *IEEE Trans. Magn.* **32**, 4472–4474 (1996). 3, 3.1

[60] E. F. Wassermann, M. Thielen, S. Kirsch, A. Pollmann, H. Weinforth and A. Carl. "Fabrication of large scale periodic magnetic nanostructures". *J. Appl. Phys.* 3

[61] M. Farhoud, M. Hwang, H. I. Smith, M. L. Schattenburg, J. M. Bae, K. Youcef-Toumi and C.A. C. A. Ross. "Fabrication of large area nanostructured magnets by interferometric lithography". *IEEE Trans. Magn.* **34**, 1087–1089 (1998). 3, 3.1

[62] M. A. M. Haast, J. R. Schuurhuis, L. Abelmann, J. C. Lodder and Th. J. Popma. "Reversal mechanism of submicron patterned CoNi/Pt multilayers". *IEEE Trans. Magn.* **34**, 1006–1008 (1998). 3, 3.1, 4.1, 4.5, 5.4

[63] J. P. Spallas, R. D. Boyd, J. A. Britten, A. Fernandez, A. M. Hawryluk, M. D. Perry, and D. R. Kania. "Fabrication of sub-0.5 m diameter cobalt dots on silicon substrates and photoresist pedestals on 50 cm 50 cm glass substrates using laser interference lithograph". *J. Vac. Sci. Technol. B* **14**, 2005–2007 (1996). 3

[64] L. Prodan, T.G. Euser, H.A.G.M. van Wolferen, C.G.Bostan, R.M. de Ridder, R.Beigang, K.-J. Boller and L.Kuipers. "Large-area two-dimensional silicon photonic crystals for infrared light fabricated with laser interference lithography". *Nanotechnology* **15**, 639–642 (2004). 3.1

[65] C.G. Bostan and R.M. de Ridder. "Design of photonic crystal slab structures with absolute gaps in guided modes". *J. Optoelectron. Adv. Mater* **4**, 921–928 (2002). 3.1

[66] L. Vogelaar, W. Nijdam, H.A.G.M. van Wolferen, R.M. de Ridder, F.B. Segerink, E. Flck, L. Kuipers and N.F. van Hulst. "Large area photonic crystal slabs for

visible light with waveguiding defect structures: fabrication with focused ion beam assisted laser interference lithography". *Advanced Materials* **13**, 1551–1554 (2001). 3.1

[67] E. Berenschot, N. Tas, J. Haneveld, H. Jansen and M. Elwenspoek. "Wet anisotropic etching for fluidic 1d nanochannels". *J. Micromech. Microeng.* **13**, S62–S66 (2003). 3.1

[68] H. Jansen, M. Elwenspoek, N. Tas, J. Haneveld and A. Van Den Berg. "Capillary filling speed of water in nanochannels". *Appl. Phys. Lett.* **85**, 3274–3276 (2004). 3.1

[69] H. H. Solak, C. David, J. Gobrecht, L. Wang and F. Cerrina. "Multiple-beam interference lithography with electron beam written gratings". *J. Vac. Sci. Technol. B* **20**, 2844–2848 (2002). 3.3.4

[70] V. Berger, O. Gauthier-Lafaye and E. Costard. "Photonic band gaps and holography". *J. Appl. Phys.* **82**, 60–64 (1997). 3.3.4

[71] T. A. Savas, S. N. Shah, M. L. Schattenburg, J. M. Carter and Henry I. Smith. "Achromatic interferometric lithography for 100-nm-period gratings and grids". *J. Vac. Sci. Technol. B* **13**, 2732–2735 (1995). 3.3.4

[72] A. Yen, E. H. Anderson, R. A. Ghanbari, M. L. Schattenburg and H. Smith. "Achromatic holographic configuration for 100-nm-period lithography". *Appl. Opt.* **31**, 4540–4545 (1992). 3.3.4

[73] G. A. Bertero, R. Sinclair, C. H. Park and Z. X. Shen. "Interface structure and perpendicular magnetic anisotropy in Pt/Co multilayers". *J. Appl. Phys.* **77**, 3953–3959 (1995). 4.1

[74] S. Foner. "The vibrating sample magnetometer: Experiences of a volunteer (invited)". *J. Appl. Phys.* **79**, 8 (1996). 4.2.1

[75] A. G. van den Bos, A. J. le Fbre, H. Saito, K. Ramstöck, M. H. Siekman, L. Abelmann and J. C. Lodder. "High Resolution magnetic tips and integrated multiwire probes for scanning probe microscopy". *AIP Conf. Proc.* **696**, 320 (2003). 4.2.2

[76] N. Kikuchi, R. Murillo and J. C. Lodder. "AHE measurements of very thin films and nanosized dots". *J. Magn. Magn. Mater.* **287**, 320–324 (2005). 4.2.4, 4.6.1

[77] S. Haan, C. Lodder and T.J.A. Popma. "The (anomalous) Hall magnetometer as an nalysis tool for high density recording media". *J. Magn. Soc. Jpn.* **15**, 349 (1991). 4.2.4

[78] N. Kikuchi, S. Okamoto, O. Kitakami, Y. Shimada and K. Fukamichi. "Sensitive detection of irreversible switching in a single FePt nanosized dot". *Appl. Phys. Lett.* **82**, 4313 (2003). 4.2.4

[79] A. Zú niga Segundo, F. Ruiz, C. Vázquez-LóPez, J. González-Hernández, G. Torres-Delgado and D. V. Tisu. "Characterization of SiO_2 layers on Si wafers using atomic force microscopy". *J. Vac. Sci. Technol.* **A 12**, 2572–2576 (1994). 4.3

[80] M. Yasutake, S. Wakiyama and Y. Kato. "Measurement of Si wafer and SiO_2 layer microroughness by large sample atomic force microscope". *J. Vac. Sci. Technol.* **B 12**, 1572–1576 (1994). 4.3

[81] A. S. Penfold. "Magnetron Sputtering". *in: 'Handbook of thin film technology' edited by D.A. Glocker and S.I. Shah, Institute of Physics Publishing* **A3.2**, 10 (1995). 4.4

[82] W. P. van Drent. "CoNi/Pt multilayers for magneto-optical recording". PhD. Thesis, University of Twente, Enschede, The Netherlands (1995). 4.4

[83] J. R. Barnes, S. J. O'Shea, M. E. Welland, J. Y. Kim, J. E. Evetts and R. E. Somekh. "Magnetic force microscopy of Co-Pd multilayers with perpendicular anisotropy". *J. Appl. Phys.* **76**, 2974–2980 (1994). 4.5

[84] R. Dammel. "Diazonaphthoquinone-based Resists; Tutorial Texts in Optical Engineering, v. TT 11". SPIE Optical Engineering Press: Bellingham, WA (1993). 5.2

[85] H. Vi Tran. "Materials for advanced microlithography: polymers for 157 nm lithography and acid diffusion measurements". PhD. Thesis, University of Texas at Austin, Austin, Texas (2002). 5.2

[86] A. Reiser. "Photoreactive Polymers: The Science and Technology of Resists". John Wiley and Sons, New York (1989), isbn = 0471855502,). 5.2

[87] K. Uenishi, Y. Kawabe, T. Kokubo, S. Slater and A. Blakeney. "Structural effects of DNQ-PAC backbone on resist lithographic properties". *Proc. SPIE Int. Soc. Opt. Eng.* **1466**, 102–116 (1991). 5.2

[88] C. L. McAdams, P. Tsiartas and C. G. Willson. "Structure-Function Correlation Studies of Dissolution Inhibitors for Novolac-based Photoresists". *Polym. Mater. Sci. Eng.* **77**, 437–438 (1997). 5.2

[89] M. L. Schattenburg, R. J. Aucoin and F. C. Fleming. "Optically matched trilevel resist process for nanostructure fabrication". *J. Vac. Sci. Technol. B* **13**, 3007–3011 (1995). 5.3.1

[90] X. Sun, L. Zhuang, W. Zhang and S. Y. Chou. "Multilayer resist methods for nanoimprint lithography on nonflat surfaces". *J. Vac. Sci. Technol. B* **16**, 3922–3925 (1998). 5.3.1, 5.8, 7.3.3

[91] B. M. Rathsack, C. E. Tabery, T. B. Stachowiak, J. Albelo and C. G. Willson. "Simulation based formulation of non-chemically amplified resist for 257 nm laser mask fabrication". *SPIE Advances in Resist Technology and Processing* **17**, 3999–61 (2000). 5.3.1

[92] S. Fujimori. "Computer simulation of exposure and development of a positive photoresist". *J. Appl. Phys.* **50**, 615623 (1979). 5.3.1

[93] H. Kelderman. "Interferometric Lithography Simulation". Internal communication, Systems and Materials for Information storage group, University of Twente, The Netherlands (2005). 5.3.1

[94] R. Atkinson, S. Pahirathan, I.W. Salter, P.J. Gmndy, C.J. Tatnall, J.C. Lodder and Q. Meng. "Fundamental optical and magneto-optical constants of Co/Pt and CoNi/Pt multilayered films". *Journal of Magnetism and Magnetic Materials* pages 131–138 (1996). 5.3.1

[95] P. R. Puckett, S. L. Michel and W. E. Hughes. "Thin Film Processes; Section V-2". Academic Press, New York (1991), isbn = 0-12-728251-3,). 5.4

[96] "Clariant AZ and MicroChemicals... TI photoresists and what they perform". *MicroChemicals GmbH, Ulm* [www.microchemicals.com]. 5.6

[97] B.C. Min. "Laser Interference Lithography with image reversal technique". Internal communication, Systems and Materials for Information storage group, University of Twente, The Netherlands (2004). 5.6

[98] I. Vera. "Fabrication of nanomagnets using a hard mask scheme". M.Sc. Report, Systems and Materials for Information storage group, University of Twente, The Nehterlands (2005). 5.6, 5.16

[99] P. Gaunt. "Magnetic viscosity and thermal activation energy". *J. Appl. Phys.* **59**, 4129–4132 (1986). 6.1

[100] S. T. Chui. "Nucleation of planar magnetization in ultr-thin magnetic films". *J. Magn. Magn. Mater.* **168**, 9–14 (1997). 6.1

[101] R. H. Victora. "Predicted time dependence of the switching field for magnetic materials". *Phys. Rev. Lett.* **63**, 457–460 (1989). 6.1

[102] E. C. Stoner and E. P. Wohlfarth. "A mechanism of magnetic hysteresis in heterogeneous alloys". *Phil. Trans. Soc. London* **A 240**, 599–642 (1948). 6.1

[103] Q. Meng. "Magneto-optical recording media CoNi/Pt and Co/Pt multilayers". PhD. Thesis, University of Twente, Enschede, The Netherlands (1996), isbn = 90-9009945-x,). 6.2.1

[104] J. Shi, D. Kojima and M. Hashimoto. "The interaction between platinum films and silicon substrates: Effects of substrate bias during sputtering deposition". *J. Appl. Phys.* **88**, 1679–1683 (2000). 7.2.1

[105] C. Canali, C. Catellani, M. Prudenziati, W. H. Wadlin and Jr. C. A. Evans. "Pt_2Si and PtSi formation with high-purity Pt thin films". *Appl. Phys. Lett.* **31**, 43–45 (1977). 7.2.1

[106] C. A. Crider and J. M. Poate. "Growth rates for Pt_2Si and PtSi formation under UHV and controlled impurity atmospheres". *Appl. Phys. Lett.* **36**, 417–419 (1980). 7.2.1

[107] B. D. Terris and T. Thomson. "Nanofabricated and self-assembled magnetic structures as data storage media". *J. Phys. D: Appl. Phys.* **38**, R199R222 (2005). 7.5

[108] J. Y. Cheng, C. A. Ross, E. L. Thomas, H. I. Smith and G. J. Vancso. "Fabrication of nanostructures with long-range order using block copolymer lithography". *Appl. Phys. Lett.* **81**, 3657–3659 (2002). 7.5

Appendix A

Anisotropy and energy barrier of Stoner-Wohlfarth particles

A.1 Field of anisotropy for a Stoner-Wohlfarth particle

Consider that the density of magnetostatic energy of a particle can be expressed as

$$\varepsilon_T = \varepsilon_a + \varepsilon_H \tag{A.1}$$

where ε_a represents the energy density of anisotropy and ε_H the energy density due to an external applied field H. In the case of a Stoner-Wolfarth particle, the energy of anisotropy is described by

$$\varepsilon_a = K_u \sin^2 \phi \tag{A.2}$$

whith K_u the constant of anisotropy and ϕ the angle of the magnetization with respect to the anisotropy axis. If the external field H is applied along the anisotropy axis of the particle, but antiparallel to the local anisotropy equilibrium direction (refer to Figure A.1, then the energy density is given by

$$\varepsilon_H = -\mu_0 MH \cos(180 - \phi) = \mu_0 MH \cos \phi \tag{A.3}$$

Using the former expressions for the energy density of anisotropy and the density of magnetostatic energy it is possible to rewrite (A.1) as

$$\varepsilon_T = K_u \sin^2 \phi + \mu_0 MH \cos \phi \tag{A.4}$$

The necessary field in order to equal the torque due to the anisotropy at a certain angle ϕ is found through the following expression

$$0 = \frac{d\varepsilon_T}{d\phi} = 2K_u \sin \phi \cos \phi - \mu_0 MH \sin \phi = (2K_u \cos \phi - \mu_0 MH) \sin \phi \tag{A.5}$$

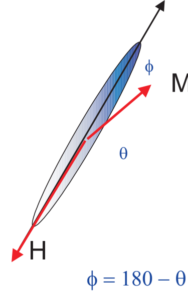

Figure A.1: *External field H applied along the anisotropy axis of a Stoner-Wohlfarth particle, but antiparallel to the local anisotropy equilibrium direction*

Assuming that $\sin\phi \neq 0$, we have that

$$2K_u \cos\phi = \mu_0 M H \qquad \Rightarrow \qquad H = \frac{2K_u}{\mu_0 M}\cos\phi \tag{A.6}$$

It should be noted that as ϕ approaches to zero, H becomes greater. The maximum value of H is denoted as H_0 and is found when $\phi \to 0$, i.e.

$$H_0 = \lim_{\phi\to 0} \frac{2K_u}{\mu_0 M}\cos\phi = \frac{2K_u}{\mu_0 M} \tag{A.7}$$

H_0 is called the *anisotropy field* and represents the magnetic field along the anisotropy axis which is necesary to compensate the anisotropy torque at very small angles.

A.2 Energy Barrier for a Stoner-Wohlfarth particle

As mention before, if an external field is applied along the anisotropy axis of a Stoner-Wohlfarth particle, but opposite to the direction of magnetization (Figure A.1)the energy density will be given by (A.4). The energy barrier which should be overcome in order to switch the magnetization direction is expressed by

$$\Delta E = E_{max} - E_{min} \tag{A.8}$$

where E_{max} and E_{min} are the maximum and minimum values of the energy in the system. Now we look for the expressions for ε_{max} and ε_{min}. From (A.5) it is noticeable that two of the critical points are found when $\sin\phi = 0$, (i.e. $\phi = 0, 180$). And the two other critical points are found when $\cos\phi = \frac{\mu_0 M H}{2K_u}$ (there are two values of ϕ which fulfill the former equation, but those values are

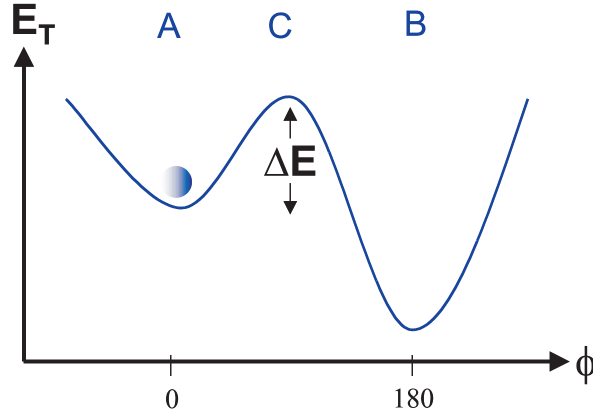

Figure A.2: *Sketch of the total energy E_T as a function of the angle of the magnetization (given in degrees)*

symmetric as respect to the anisotropy axis). Evaluating the critical values in the second derivative of (A.4)

$$\frac{d^2\varepsilon_T}{d\phi^2} = (2K_u \cos\phi - \mu_0 MH)\cos\phi - 2K_u \sin^2\phi \tag{A.9}$$

we get that

$$\left.\frac{d^2\varepsilon_T}{d\phi^2}\right|_{\phi=0,180} = 2K_u \pm \mu_0 MH > 0 \qquad \text{(provided that } H \neq H_0\text{)} \tag{A.10}$$

Thus, $\phi = 0$, 180, corresponds to minima. And we get that

$$\left.\frac{d^2\varepsilon_T}{d\phi^2}\right|_{\cos\phi=\frac{MH}{2K_u};\phi\neq 0,180} = -2K_u \sin^2\phi < 0 \tag{A.11}$$

Thus, the condition $\cos\phi = \frac{\mu_0 MH}{2K_u}$ corresponds to a maximum.

Figure A.2 shows the sketch of the total energy (E_T), as a function of angle ϕ, as described in (A.4). $\phi = 0$ corresponds to the local minimum of the initial state, while $\phi = 180$ corresponds to the final state after the magnetization switch has taken place. Thus, the magnitude of the energy barrier corresponds to the substraction of the energy values on the points labelled as C and A from Figure A.2.

Thus,

$$\Delta\varepsilon = \varepsilon_{max} - \varepsilon_{min}$$

$$= K_u \sin^2 \phi_{max} + \mu_0 MH \cos \phi_{max} - K_u \sin^2 \phi_{min} - \mu_0 MH \cos \phi_{min}$$

but $\phi_{min} = 0$, then

$$\Delta\varepsilon = K_u \sin^2 \phi_{max} + \mu_0 MH \cos \phi_{max} - \mu_0 MH$$

$$= K_u (1 - \cos^2 \phi_{max}) + \mu_0 MH \cos \phi_{min} - \mu_0 MH$$

but $\cos \phi_{max} = \frac{\mu_0 MH}{2K_u}$, then

$$\Delta\varepsilon = K_u \Big[1 - \Big(\frac{\mu_0 MH}{2K_u} \Big)^2 + \frac{(\mu_0 MH)^2}{2{K_u}^2} - \frac{\mu_0 MH}{K_u} \Big]$$

$$= K_u \Big[1 - \frac{1}{4} \Big(\frac{\mu_0 MH}{K_u} \Big)^2 + \frac{1}{2} \Big(\frac{\mu_0 MH}{K_u} \Big)^2 - \frac{\mu_0 MH}{K_u} \Big]$$

$$= K_u \Big[1 - \frac{\mu_0 MH}{K_u} + \Big(\frac{\mu_0 MH}{2K_u} \Big)^2 \Big]$$

$$= K_u \Big[1 - \frac{\mu_0 MH}{2K_u} \Big]^2$$

but we mention before that $K_u = \frac{\mu_0 M H_0}{2}$, then

$$\Delta\varepsilon = K_u \Big[1 - \frac{H}{H_0} \Big]^2 \tag{A.12}$$

or

$$\Delta E = K_u V \Big[1 - \frac{H}{H_0} \Big]^2 = U \Big[1 - \frac{H}{H_0} \Big]^2, \tag{A.13}$$

where V is the volume of the particle and U is know as the internal energy. This is the expression for the energy barrier.

Summary

In the last century there has been an accelerated development in information technologies, with an enhanced trend in magnetic storage systems. In order to be sustained, this accelerated development requires the creation of new technologies and devices which could allow higher storage densities, portability, lower power consumption and faster access and processing of the retrieved information.

This work is the result of four years of research in the field of magnetic patterned media with potential applications for ultra high density information storage systems. A novel tool, Laser Interference Lithography (LIL) has been used in order to fabricate an experimental prototype of such media.

In Chapter One, a brief overview of the historical development of magnetic recording is presented. Two possible pathways are here considered to keep pace with the trend in the increase of areal bit density of magnetic recording: Perpendicular anisotropy media and patterned media.

An ideal magnetic patterned medium with potential application in high density probe recording is presented in Chapter Two. The medium is considered to be compound of identical elements arranged in a squared periodic lattice. First we present a discussion giving a general description of the medium. Then follows a discussion on the thermostability, where aspects as switching probability of individual elements in the array are considered. From it, calculated values for the relaxation time are given. Raw bit error rate is also discussed and an acceptable energy barrier to thermal energy ratio is estimated. Numerical estimations are presented on the subject of required switching fields for individual magnetic elements depending on the magnetization state of neighbouring elements. A discussion on the required anisotropy and magnetization saturation is also presented. The dimensions of a reading/writing probe are considered. It is concluded that an auxiliary field is necessary for writing. Upper and lower limits to this auxiliary field are given.

Chapter Three serves as an introduction to the Laser Interference Lithography technique. This is an alternative mask-less lithographic technique, in which a photosensitive resist is exposed to an interference pattern produced by two coherent laser beams. This lithographic technique has the capability of generating

patterned structures over large areas and in short time (typically less than one minute).

Different kinds of experimental arrays are described and some of their advantages and limitations are mentioned. At present, the theoretische minimum period of the interference pattern at the MESA+ LIL setup is 133 nm, which corresponds to half the wavelength of the laser source used. Periodes of 150 nm have been experimentally obtained.

In Chapter Four the deposition process of continuous magnetic multilayered CoNi / Pt and Co / Pt films is presented. The substrate preparation is explained and the influences of the substrate material to the magnetic properties of the deposited films. The effect of the number of deposited bilayers on the magnetic properties is also discussed. The films were characterized by Magnetic Force Microscopy, Vibrating Sample Magnetometry, Anomalous Hall Effect and Magneto-Optical Kerr effect. With these techniques it was found that smoother substrates favour sharper transitions in the magnetization switching.

Chapter Five deals with the process of patterning of the continuous samples mentioned in Chapter Four. The first step in the LIL processing consists in coating the sample (in this case the continuous magnetic films) with a photoresist system. Then the photoresist is exposed to the interference pattern produced by the LIL setup. Afterwards the resist is developed. Then an etching process follows in order to transfer the resist pattern into the sample. Finally, the photoresist system should be removed from top of the patterned sample. In Chapter Five we compare three different photoresists systems that were tested as part of this research. The first one is a single positive photoresist layer. The second consists of a three-layer system consisting of an antireflection coating (ARC) at the bottom, an interlayer acting as a hardmask during the subsequent etching process, and a positive resist on the top. The third one is an image reversal resist acting as a shadow mask for the evaporation of a hard etching mask.

Some of the magnetic properties of the CoNi/Pt and Co/Pt patterned films are studied in Chapter Six. Thermostability and switching field distribution are two important parameters for any recording medium. A thermally stable magnetization state will warranty that the stored information will remain unchanged for a long time. On the other hand, a lower switching field distribution means that in such a medium each bit of information can be written by exerting the same (or at least a similar) magnetic field, which helps to avoid side writing. In the analysis of the dots the coercivity plays an important role. Because of this, in the first section of Chapter Six we consider an ensemble of nanomagnets and we derive an expression which relates the coercivity of the ensemble with its internal energy. By using that expression (in combination with experimental data) a study on the thermal stability and distribution of the switching field of arrays of CoNi/Pt and Co/Pt dots is presented. Those structures have diameters around 90 nm and a periodicity of 300 nm. The thermal dependence of the

averaged switching field has been investigated by means of VSM. Additionally, the switching field distribution at room temperature is obtained by performing VSM remanent measurements and MFM measurements.

General conclusions are presented in Chapter Seven. In this chapter the conclusions are summarized from two different views. One is about boundary conditions for designing a patterned media and the other is about the preparation and lithographic processes necessary to fabricate patterned media. At the end of this chapter some recommendations for future research are given.

Samenvatting

In de vorige eeuw hebben we een versnelde ontwikkeling meegemaakt in de informatie technologie, met daarin een belangrijke trend in magnetische data opslag systemen. Om deze trend voort te zetten zijn nieuwe technologieën en systemen nodig, met hogere data-dichtheden, draagbaarheid, lager vermogensverbruik en snellere toegang tot en verwerking van data.

Dit proefschrift geeft het resultaat weer van vier jaar onderzoek op het gebied van magnetische patterned media, met mogelijke toepassing in ultra-hoge dichtheid data opslag systemen. Een nieuwe methode, de Laser Interferentie Lithografie (LIL) is toegepast om een experimenteel prototype van een dergelijk medium te fabriceren.

In hoofdstuk 1 wordt een kort overzicht gegeven van de geschiedenis van magnetische recording. Er zijn twee mogelijke routes om de trend van steeds toenemende data-dichtheden voort te zetten: media met loodrechte anisotropie en patterned media.

Het ideale medium voor toepassing in hoge dichtheid probe recording wordt besproken in hoofstuk 2. Dit medium bestaat uit identieke elementen, die in een vierkant array zijn geplaatst. Het hoofdstuk begint met een algemene beschrijving van een dergelijk medium. Daarna volgt een discussie over thermische stabiliteit, waarbij aspecten worden beschouwd zoals de kans op switching van individuele elementen in het array. Hieruit volgen waarden voor de relaxatietijd van elementen. De raw bit error rate wordt behandeld, en een schatting voor een minimaal acceptabele verhouding tussen energie barrière en thermische energie. Numerieke berekingen worden gepresenteerd voor de relatie tussen switching velden van individuele elementen en de magnetische toestand van de omringende buren. Daarna volgt een discussie over de vereiste anisotropie en verzadigingsmagnetisatie. Het hoofstuk besluit met de conclusie dat een uitwendig hulpveld benodigd is om te kunnen schrijven, en de onder- en bovengrenzen van dit veld worden berekend.

In hoofdstuk 3 wordt Laser Interferentie Lithografie geïntroduceerd. Dit is een maskerloze lithografie techniek, waarbij een fotogevoelige laag (resist) wordt belicht met een interferentie patroon dat wordt gegenereerd door twee coherente laserbundels. Deze lithografie techniek stelt ons in staat in zeer korte

tijd (onder 1 minuut) belichtingen uit te voeren over grote oppervlakken. In dit hoofdstuk worden de voor- en nadelen van verschillende experimentele configuraties worden beschreven. De theoretisch minimaal haalbare periode van het interferentie patroon in de MESA$^+$LIL setup is 133 nm (halve golflengte van het gebruikte laserlicht). Op dit moment zijn periodes van 150 nm experimenteel gerealiseerd.

In hoofdstuk 4 wordt het depositieproces van CoNi/Pt en Co/Pt films gepresenteerd. De substraat preparatie wordt besproken, en de invloed van het substraat materiaal op de magnetische films. Vervolgens wordt het effect van het aantal lagen in de multilaag op de magnetische eigenschappen bediscussieerd. De films zijn gekarakteriseerd met behulp van Magnetic Force Microscopy, Vibrating Sample Magnetometry, Anomalous Hall Effect en Magneto-Optisch Kerr effect. Deze technieken laten zien dat gladdere lagen een scherpere transitie in de magnetisatie reversal hebben.

In hoofdstuk 5 wordt het process besproken waarmee patterned media worden gemaakt uit de continue films van hoofdstuk 4. De eerste stap in het dit proces bestaat uit het coaten van het sample (in dit geval de magnetische multilaag) met een fotoresist systeem. Daarna wordt de fotoresist belicht met het interferentie patroon dat door de LIL opstelling wordt gegenereerd. Vervolgens wordt de belichte resist ontwikkeld en wordt het resist patroon middels een etsstap in het sample overgebracht. Ten slotte moet de fotoresist van het sample worden verwijderd. In hoofdstuk 5 worden tests met drie verschillende fotoresist systemen behandeld. Het eerste systeem is een enkele fotoresist laag. Het tweede bestaat uit een drielaags pakket met een anti-reflectie coating (ARC) aan de onderkant, een tussenlaag die als hard-mask dienst doet, en een positieve resist als toplaag. Het derde is een image reversal resist die als shaduw masker dient voor het opdampen van een hard etching mask.

Een aantal magnetische eigenschappen van patterned CoNi/Pt en Co/Pt films worden besproken in hoofdstuk 5. Thermische stabiliteit en switching field distribution zijn belangrijke parameters voor recording media. Een thermisch stabiele magnetisatietoestand garandeert dat de informatie voor lange tijd behouden blijft. Een lage switching field distributie zorgt ervoor dat iedere dot in het medium bij min of meer hetzelfde veld beschreven kan worden, zodat side-writing voorkomen wordt. In de analyse van de dots speelt de coerciviteit een grote rol. Daarom wordt in het eerste deel van hoofdstuk 6 een uitdrukking afgeleid voor de relatie tussen de coerciviteit van een ensemble van nanomagneten en de interne energie. Op basis van deze uitdrukking (in combinatie met experimentele resultaten) wordt de thermische stabiliteit en switching field distributie van arrays van CoNi/Pt en Co/Pt dots gepresenteerd. In deze arrays hebben de dots een diameter van ongeveer 90 nm en een periodiciteit van 300 nm. Met behulp van VSM is de thermische afhankelijkheid van het gemiddelde switching field onderzocht. Daarnaast is de switching field distributie gemeten

door remanente VSM en/of MFM.

De algemene conclusies worden gepresenteerd in hoofdstuk 7. In dit hoofdstuk zijn de conclusies samengevat volgens twee verschillende uitgangspunten. In het ene geval wordt er uitgegaan van de randvoorwaarden voor het ontwerp van een patterned medium. De preparatie en lithografie processen die noodzakelijk zijn voor de realisatie van patterned media zijn het andere uitgangspunt. Het hoofdstuk eindigt met enkele aanbevelingen voor verder onderzoek.

Resumen

A lo largo del pasado siglo se ha ido produciendo un desarrollo acelerado en las tecnologías de la informacíın, con especial enfásis en los sistemas de almacenamiento magnéticos. Para conservar esta progresión es necesario el desarrollo de nuevas tecnologías y dispositivos que permitan una mayor densidad de almacenamiento de datos, portabilidad y un consumo energético inferior, así como un acceso y procesamiento más rápido de la información almacenada.

Esta tesis es el producto de cuatro años de investigación en el campo de medios magnéticos nanoestructurados con aplicaciones potenciales a sistemas de almacenamiento de datos de ultra alta densidad. Un sistema experimental novedoso, la Litografía por Interferometría Láser (LIL), es la herramienta con la que se han fabricado los prototipos de medio magnético de almacenamiento de datos.

En el Capítulo Uno se hace un pequeño resumen de la evolución histórica de los medios de grabación magnética. De aquí se deduce que dos posibles formas de mantener la progresión de almacenamiento de información por unidad de superficie son los medios con imanación perpendicular y los medios estructurados.

En el Capítulo Dos se presenta un medio magnético estructurado ideal con posibles aplicaciones en medios de grabación de alta densidad mediante sonda magnetica. Se considera que el medio esta compuesto de elementos idénticos ordenados de forma periodica en una red cuadrada. En primer lugar se hace una descripción general del medio. En segundo lugar, se estudia la termoestabilidad para lo que se tiene en cuenta la probabilidad de inversión de los elementos de la red. Esto nos proporciona una serie de valores para el tiempo de relajación de la muestra. Además, se estudia la proporción de bits defectuosos y de ello se obtiene una estimación de los valores aceptables para el cociente entre la barrera de energía de los elementos y la energía térmica. Asimismo se muestran unas estimaciones numéricas acerca de los campos necesarios para invertir la imanación de elementos magnéticos individuales en función del estado de la imanación de sus vecinos, complementado con un estudio de la anisotropía y de la imanación de saturacion necesarias y teniendo en cuenta el tamaño de la sonda de lectura/escritura. Del estudio previamente descrito se deduce la

necesidad de utilizar un campo magnético auxiliar para escribir un bit, proporcionando estimaciones para los límites superior e inferior de dicho campo.

El Capítulo Tres sirve como introducción a la técnica de Litografía por Interferomentría Láser, un método alternativo de litografía sin máscara. En esta técnica, una resina fotosensible se expone a un patrón de interferencia producido por dos haces láser coherentes. Este procedimiento litográfico posee la capacidad de generar estructuras ordenadas sobre grandes áreas en poco tiempo (normalmente menos de un minuto). Se describen algunos de los distintos tipos de redes, así como las ventajas y limitaciones del metodo. Actualmente, el mínimo periodo del patrón de interferencia que se puede conseguir en el dispositivo LIL del MESA+ es de 133 nm, que corresponde a la mitad de la longitud de onda de la fuente de láser utilizada.

En el Capítulo Cuatro se presentan los metodos de crecimiento de películas delgadas de multicapas magnéticas de CoNi/Pt y Co/Pt. Además se explica la forma de preparar el sustrato previo al crecimiento y como ésto influye en las propiedades magnéticas de las películas. Asimismo, se estudia el efecto en las propiedades magnéticas del número de bicapas crecidas. Las películas magnéticas se caracterizan mediante Microscopía de Fuerza Magnética (MFM), Magnetometría de Muestra Vibrante (VSM), Efecto Hall Anómalo (AHE) y Efecto Kerr Magneto-Óptico (MOKE). Mediante la aplicación de estas técnicas en nuestras muestras se deduce que los sustratos más lisos son los que favorecen las transiciones más rápidas en la inversión de la imanación.

El Capítulo Cinco trata del proceso de litografía de las muestras continuas mencionadas en el Capítulo anterior. El primer paso del proceso de Litografía por Interferometría Láser consiste en revestir la muestra (en este caso la película magnética continua) con una fotorresina, para luego hacer una exposición controlada en el tiempo al patrón de interferencia producido por el dispositivo LIL. A continuación se revela la resina, continuando con un ataque por iones de argón de forma que la red dibujada sobre la resina se transfiere a la película delgada. Por último, la resina debe eliminarse de la muestra dando como resultado un medio estructurado. En este capítulo se comparan tres tipos de fotorresinas que fueron probadas como parte de esta investigación. La primera de ellas consiste en una única capa de fotorresina positiva. La segunda es un sistema de tres capas compuesto por un Recubrimiento Antirreflectante (ARC) sobre el que se coloca una intercapa actuando como "hard maskij superpuesta a ella se sitúa una capa de resina positiva. La tercera es una resina de imagen invertida actuando como máscara de sombra para la evaporación de una "hard etching mask"

Algunas de las propiedades magnéticas de las películas de CoNi/Pt y Co/Pt litografiadas se estudian en el Capítulo Seis. La termostabilidad y la distribución del campo de inversión (SFD) son dos parámetros importantes para los medios magnéticos de grabación. Un material térmicamente estable garantiza que la información almacenada permanecerá inalterada por largo tiempo. Por otra

parte, una baja distribución del campo de inversión significa que en ese medio de grabación, cada bit de información puede ser escrito ejerciendo el mismo (o al menos similar) campo magnético, lo que ayuda a evitar la escritura colateral. En este análisis, la coercitividad juega un papel importante, por esa razón en la primera parte del Capítulo Seis se considera un conjunto de nanoimanes y se deduce una expresión que relaciona la coercitividad del conjunto con su energía interna. Utilizando dicha expresión (en combinación con los datos experimentales) se presenta un estudio de la termoestabilidad y de la distribución del campo de inversión en redes de puntos de CoNi/Pt y Co/Pt de 90 nm de diámetro y 300 nm de periodicidad. La dependencia térmica del campo de inversión promedio se estudia por medio del VSM. Asimismo, la distribución del campo de inversión a temperatura ambiente se determina mediante medidas de VSM en remanencia y medidas de MFM.

En el Capítulo Siete se presentan las conclusiones generales de este trabajo, resumidas desde dos puntos de vista. Uno de ellos está relacionado con las condiciones de frontera para diseñar medios estructurados y el otro está relacionado con la preparación de las muestras y los procesos de litografía necesarios para fabricar estos medios. Al final de este capítulo se hacen algunas recomendaciones de cara a futuras investigaciones.

Acknowledgements

First of all, I would like to express my gratitude to all my fellow colleagues and ex-colleagues at the Systems and Materials Group for Information Storage (SMI). PhD and postdoc researchers, technicians and supervisors have contributed day by day to produce in the SMI group a very nice and enjoyable working atmosphere. Even when I feel grateful to all of them, it is unavoidable to mention some specific names within these lines:

Onoue-san and Kikuchi-san, from whom I have learnt a lot not only about magnetism but discipline and modesty.

Martin Siekman. My PhD project was greatly influenced by his technical support and initiative to measure and write some of my samples. No one has made as many experiments on my samples as him.

Arnout van den Boss from whom I received guidance and advice during the first months of my PhD project.

It is priceless to count with two such kind an efficient secretaries within our group. There are too many little and not so little details that Karen and Thelma have arranged for me within these last years.

The guidance, supervision and flexibility of Cock and Leon, promotor and co-promotor of my PhD project, have been of paramount importance in these four years. My view of science and research has evolved because of them.

I had the privilege of supervising three students at the University of Twente. They have contributed to parts of this thesis as part of their assignments. Barry carried out a number of VSM and MOKE measuremnts which have been included in this work. David and Sebastiaan worked on optical simulations concerning the behaviour of the antireflection coatings and vertical standing waves.

This research could not be possible without a laser interference lithography setup. Henk van Wolferen was the person who has constructed this amazing instrument and kept it running. Building such a machine was not only a technical job but an art.

During the last months of my project I had the privilege of meeting Henry Kelderman. He became familiar with the LIL setup so soon and he produced for me a number of samples that were analysed in this work. During his stay at SMI I was benefited from his knowledge and experience.

Iván and Byoung-Chul at SMI explored the possibilities of a reversal image photoresist. What they have learnt has been of influence for my own work.

The experimental work contained in this thesis was possible because of the effort of our technicians at the Clean Room facilities and the Institute for Materials Research and Thin Films Technology at the University of Twente. I must mention that Mark Smithers is the responsible for most of the SEM images displayed in this book.

I appreciate the interest of all the members of the user's committee. Specially, the advice of ASML on photolithography and resists opened new possibilities for further improvement of the sample's fabrication process.

A PhD project is more than amazing equipment, excellent technicians, creativity, guidance and supervision. Moral support is an important thing in life. My deep gratitude to Stephany and Blas, they are no less than my own family in The Netherlands.

Norma, Irma, Diana, Alicia, Alma and Eduardo, disregarding the distance and the seven hours time difference between Mexico and The Netherlands you have been always present during these four years.

My appreciation to the members of the Laboratorio de Física Atómica y Molecular at the National Univeristy of Mexico, the place where I started my journey into science.

List of publications

Scientific journals

First author

- R. Murillo, H.A. van Wolferen, L. Abelmann and J.C. Lodder, ”Fabrication of patterned magnetic nanodots by laser interference lithography”, *Microelectronic Engineering* 78-79 (2005) 260-265.
- R. Murillo, M.H. Siekman, T. Bolhuis, L. Abelmann and J.C. Lodder, ”Thermal stability and switching field distribution of CoNi/Pt patterned media for magnetic recording”, accepted in *Microsystem Technologies*.

Coauthor

- N. Kikuchi, R. Murillo, J.C. Lodder, K. Mitsuzuka and T. Shimatsu, ”Magnetization process of high anisotropy CoPt nanodots”, *IEEE Trans. Magn.* 41 (2005) 3613-3615.
- N. Kikuchi, R. Murillo and J.C. Lodder, ”Anomalous Hall-effect measurement study of Co/Pt nanosized dots”, *J. Appl. Phys.* 97 (2005) 10J713
- N. Kikuchi, R. Murillo and J.C. Lodder, ”AHE measurements of very thin films and nanosized dots”, *Journal of Magnetism and Magnetic Materials* 287 (2005) 320-324.
- N. Dao, N. Kikuchi, R. Murillo, L. Abelmann and J.C. Lodder, ”Micromagnetic simulation of non-uniform nanodots with perpendicular anisotropy”, submitted to *IEEE Trans. Magn.*

International Conferences (first author only)

- R. Murillo, M.H. Siekman, T. Bolhuis, L. Abelmann, J.C. Lodder, ”Thermal stability and switching field distribution of nanosized magnetic periodic structures”, *49th Annual Conference on Magnetism & Magnetic Materials*, Jacksonville, Florida, USA, November 7-11, 2004.

- R. Murillo, N. Kikuchi, M.H. Siekman, L. Abelmann, J.C. Lodder, ”Realization and analysis of Spam patterned media”, *Innovative Mass Storage Technologies Workshop 2004*, Aachen, Germany , September 28-29, 2004

- R. Murillo, M.H. Siekman, N. Kikuchi, L. Abelmann, J.C. Lodder, ”Improved fabrication method of nanomagnetic dots by laser interference lithography”, *Micro- and Nano-Engineering International Conference 2004*, Rotterdam, The Netherlands, September 19-22, 2004

- R. Murillo, M.H. Siekman, T. Bolhuis, L. Abelmann, J.C. Lodder, ”Analysis of Patterned Media for Magnetic Probe Recording”, *3rd International Probe Storage Workshop*, Zurich, Switzerland, February 28 March 1, 2005.

- R. Murillo, D. Edmundson, M.H. Siekman, L. Abelmann, B. Rodmacq, D. Wright, and J.C. Lodder, ”Probe recording in MRAM Elements using magnetic tips”*Innovative Mass Storage Technologies Workshop 2003*, Grenoble, France, September 23-24, 2003

- R. Murillo, R. Gómez. ”Characterization and identification of pigments by means of diffuse-reflectance infrared spectroscopy”, *International Materials Research Congress*, Cancún, Mexico, August 27-31, 2000.